UNIVERSITÀ DEGLI STUDI DI PADOVA

Dipartimento di Fisica a Astronomia "Galileo Galilei"

CORSO DI LAUREA MAGISTRALE IN FISICA

Neutron detectors based on siloxane scintillators and light readout through Silicon Photomultipliers

RELATORE: Dott. GIANMARIA COLLAZUOL
CORRELATORE: Dott. TOMMASO MARCHI

CANDIDATA: CATERINA CHECCHIA
MATRICOLA: 1036296 - SF

ANNO ACCADEMICO 2013/2014

Overview

This thesis deals with experimental nuclear physics, in particular with neutron detection. Neutron is a very elusive particle, being charge-less its detection is quite challenging and the research in the field of neutron detection is still very active. The presence of neutrons is often associated with γ-rays background that affects their detection, therefore a good neutron detector should be sensitive to γ-rays as well as to neutrons, being able to discriminate between them. Oganic scintillators perform suchg a tasks,having a fast timing response and the capability to distinguish between the two particles from the signal shape. Common liquid organic scintillator such as BC501 or NE213 have very good neutron/γ discrimination properties but are also toxic, flammable, volatile and polluting. For this reason, since the last few years the INFN ORIONE project has been studying effective and cheap alternative solutions less dangerous than the commercial ones for the environment.

In this context, recently some new siloxane scintillator developed at Legnaro National Laboratories in collaboration with Padova University has been developed but a deep study of their discrimination properties was not yet carried out . One of the topics of this work is indeed to identify which of these samples best approach the pulse shape discrimination properties of the commercial EJ309, also measured for comparison. To achieve this purpose several algorithms has been investigated in the first part o this work. The second part is dedicated the the coupling of these detectors with the the state of the art in solid state photodetectors, namely silicon photomultipliers. These devises could represent a valid alternative to the more common photomultiplier tubes, due to their superior amplitude and time resolution for single photons. Furthermore due to their insensitivity to magnetic fields they are suggested to be used in application where magnetic fields are needed preventing the use of photomultiplier tubes.

Chapter 1 of this thesis is dedicated to described the most common sources of neutrons, the way they interact with matter and the most widespread detection techniques.Chapter 2 will describe the scintillation processes occurring in organic scintillators and the main operation of photodetectors. The introductory part of this thesis is completed in the third chapter where the silicon photomultipliers theory and operation are described . In chapter 4 the experimental setups used to carry out the measurements are described, whereas in the subsequent chapter a summary of the most common pulse shape discrimination algorithms reported in literature is given. In the last chapter the data analysis is presented and the experimental results are discussed.

Contents

Chapter 1

Neutron Detection

Neutrons are subatomic particles with no charge and mass of $939.565\,\mathrm{MeV}/c^2$ [1] that form, along with protons, the fundamental constituents of atomic nuclei. Being charge-less, they do not not interact through the Coulomb force. Therefore even low energy neutrons (E < 1eV) can penetrate in an atomic nucleus and induce nucleon reactions. On the other hand, the total indifference to the coulomb potential makes neutrons very difficult to be detected and confined because interactions with the electrons of the most commonly used materials as detectors or absorbers, are negligible. The reason of this behaviour is that neutrons interact through the strong force which has a short range [2]. The interaction probability of neutrons inside a material is very low and therefore neutrons are very penetrating particles. This characteristic is strictly linked to the probability of neutron absorption since rarely a neutron can lose all its energy in a single interaction. High energy neutrons can have elastic or inelastic scattering with nuclei of the material: in the former case the recoil nucleus can be detected, in the latter γ-radiation of disexcitation is emitted and then detected. Less energetic neutrons may be captured from nuclei of material with consequent emission of charged particles or γ-rays. For these reasons neutrons detection constitutes an experimental challenge because it is necessary to create a detector made of a material that can interact with neutrons and able to detect all products of interactions. Furthermore, energy selection and focusing of an incident neutron beam are difficult and require development of techniques completely different from those implemented for charged beams because it is not possible to rely on accelerating effects of electric fields and properties derived from magnetic fields.

In this chapter we will described how neutron sources can be obtained, the interaction of neutrons with matter and the main features of neutron detectors.

1.1 Neutron Sources

Depending on their energy, neutrons can be classified as follows:

- Thermal $E \sim 0.025\,\text{eV}$
- Epithermal $E \sim 1\,\text{eV}$
- Slow $E \sim 1\,\text{keV}$
- Fast $E = 100\,\text{keV} - 10\,\text{MeV}$

Neutrons with an energy below 0.5 eV are slow neutrons whereas if they have an energy above this value they are called fast neutrons [3]. This value is linked to the abrupt decrease of the capture cross section of ^{113}Cd at 0.5 eV.

Even if natural neutrons emitters do not exist, several techniques can be used to artificially produce neutron fluxes [2]. There is indeed a variety of nuclear reactions that can be exploited to this purpose, the most important of which are illustrated in the following.

α - Beryllium sources The reaction used in this case (α,n) is the same responsible of the discovery of neutrons in 1932. The ^{9}Be isotope is stable and has a relatively loosely bound neutron (1.7 MeV binding energy). If an α particle from α-radioactive decay strikes this nucleus the following reaction takes place:

$$^{4}\text{He} + ^{9}\text{Be} \rightarrow ^{12}\text{C} + \text{n}$$

The Q value for this reaction is 5.7 MeV. Therefore mixing a long lived α-emitting material (e.g. ^{226}Ra, ^{241}Am, ^{210}Po) with ^{9}Be, there will be of a constant rate of neutron production . For example, if we consider ^{241}Am and its daughters, there are α's emitted with an energy of about 5 MeV and thus neutrons produced can have an energy up to about 11 MeV. The outcoming neutrons energy spectrum will not be monoenergetic for the following reasons:

1. the many α groups involved
2. the slowing down of α's by collisions in matter
3. reaction kinematics
4. the possibility that ^{12}C is left in an excited state.

For the Am-Be neutron source, the most probable neutron energy is 3 MeV and the neutron production rate is of the order of 10^6 neutrons/per second for each Ci of α activity.

Beam-induced Nuclear Reactions There are of course many nuclear reactions that produce neutrons. These require an accelerator to provide a beam of charged particles to initiate the reaction: by carefully selecting the incident energy and the angle at which we observe the emitted neutron, we can obtain a reasonably monoenergetic spectrum. Some reactions that might be used are:

- $^{7}\mathrm{Li}(\mathrm{p},\mathrm{n})^{7}\mathrm{Be}$ $\quad Q = -1.6\,\mathrm{MeV}$
- $^{3}\mathrm{H}(\mathrm{d},\mathrm{n})^{4}\mathrm{He}$ $\quad Q = +17.6\,\mathrm{MeV}$
- $^{9}\mathrm{Be}(\alpha,\mathrm{n})^{12}\mathrm{C}$ $\quad Q = +5.7\,\mathrm{MeV}$

As an example, Figure1.1 shows the dependence of the neutron energy on the incident energy and on the direction of the outgoing neutron, for the reaction $^{3}\mathrm{H}(\mathrm{d},\mathrm{n})^{4}\mathrm{He}$.

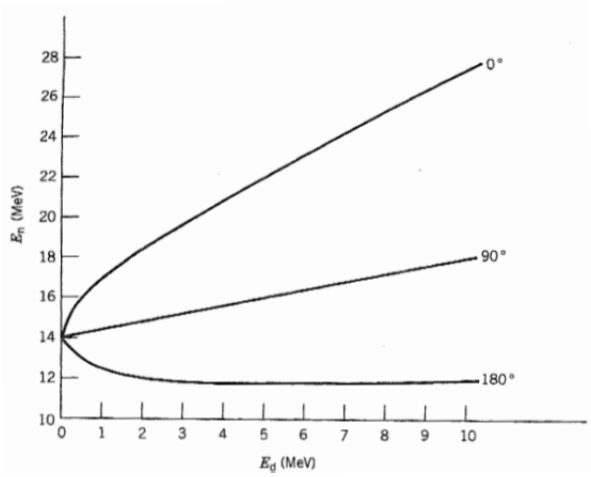

Figure 1.1: Neutrons kinematics in the $^{3}\mathrm{H}(\mathrm{d},\mathrm{n})^{4}\mathrm{He}$.

Photoneutron Sources The $(\gamma,\,\mathrm{n})$ reaction mechanism can be used to produce a neutron flux too. This process is called photoneutron production and has the advantage of provide nearly monoenergetic neutrons, particularly if the photon source is monoenergetic. For example, if we consider a ^{24}Na source, the energy of γ-rays emitted is 2.76 MeV, sufficient to overcome the neutron binding energy of ^{9}Be:

$$\gamma + {}^{9}\,\mathrm{Be} \rightarrow {}^{8}\mathrm{Be} + \mathrm{n}$$

The yield is approximately 2×10^{6} neutrons/s per Ci of ^{24}Na, but the ^{24}Na half life is relatively short (15 h). The neutron mean energy is 0.8 MeV. It is also possible to use the long lived isotope ^{124}Sb (60 d) but in this case the neutron mean energy is few tens of keV.

Spontaneous Fission An additional source of neutrons is the spontaneous fission of transuranic isotopes, e.g. ^{252}Cf with a half life of 2.65 years. Neutrons are produced directly in the fission process, at a rate of 4 per fission. The fission occurs in only about 3% of the decays which means a production rate of 2.3×10^{12} neutrons/s per gram of ^{252}Cf or 4.3×10^{9} n/s per Ci of ^{252}Cf. The energies of the emitted neutrons is shown in Figure 1.2.

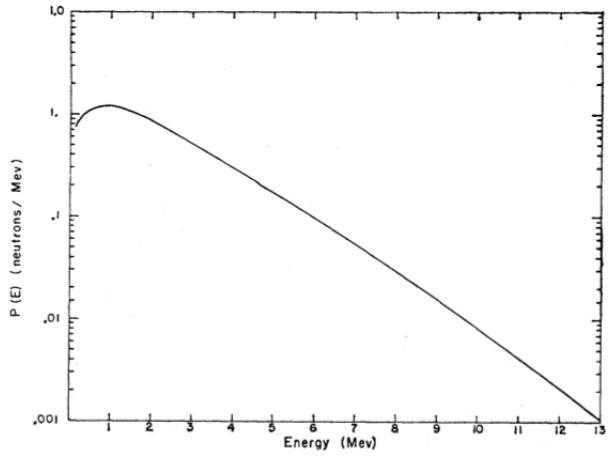

Figure 1.2: Energy spectrum of neutrons emitted by ^{252}Cf spontaneous fission (adapted from [4]).

1.2 Interaction of Neutrons with Matter

Since neutrons are charge-less, they cannot interact with matter by means of the Coulomb force, which dominates the energy loss mechanisms for charged particles and electrons. Neutrons can therefore travel through many centimetres of matter without interacting with it and thus can be totally invisible to small size detectors.The ways in which neutrons can interact with nuclei, depending on the energy, are the following:

- Elastic scattering
- Inelastic scattering
- Transmutation
- Radiative capture
- Spallation reaction
- Neutron-induced fission

As a result of the interaction, the neutron may either be absorbed (being replaced by one or more secondary particles), or change its energy and direction significantly. In this way the average energy of a neutron beam can be completely or partly reduced ("moderation" of neutrons). In contrast to γ-rays, the secondary particles produced by the interaction of a neutron with matter are almost always heavy charged ions. These particles may be produced either directly by the neutron-induced nuclear reaction, or they may be the recoil nuclei of the material itself. Thus neutrons are detected by means of the heavy charged particles produced after the interaction. For high energy neutrons the dominant process of interaction is elastic scattering with nucleons of the absorbing material. For slow or thermal neutrons the primary cause of their total absorption is capture, in the form of the (n,γ) reaction. The cross sections for this capture reactions are often dominated by one or more resonances, where the probability of absorption becomes larger. Off

resonance, the cross section decreases proportionally to v^{-1}, thus as neutrons become moderated, the probability of absorption increases. Some of the mechanisms of neutron interaction with matter are illustrated in the following.

1.2.1 Elastic scattering

Elastic scattering at non relativistic energies ($E \ll m_n c^2 = 939$ MeV), may be represented in the following way:

$$n + {}^{A}_{Z}X \rightarrow n + {}^{A}_{Z}X$$

A neutron of initial energy E and velocity v collides with a target atom of mass A initially at rest. Applying the laws of conservation of energy and linear momentum, one can obtain the ratio between the final energy E' and the initial energy:

$$\frac{E'}{E} = \frac{A^2 + 1 + 2A\,cos\theta}{(A+1)^2} \tag{1.1}$$

where θ is the scattering angle in the centre of mass system while E and E' are measured in the laboratory system. For forward scattering ($\theta = 0°$), the final energy is the same as the initial energy, whereas the maximum energy loss occurs for a head-on collision ($\theta = 180°$):

$$\left(\frac{E'}{E}\right)_{min} = \left(\frac{A-1}{A+1}\right)^2 \tag{1.2}$$

It is worth to notice that the energy transfer is maximum if the target is Hydrogen ($A = 1$). The ratio E'/E is uniformly distributed between 1 and its minimum value given by (1.2) as shown in Figure 1.3(a). Because neutrons will scatter many times, this distribution is valid only for the first scattering: in the second scattering neutrons do no longer have a monoenergetic spectrum. If we approximate this effect dividing the first step distribution in approximately monoenergetic intervals of width ΔE, we can measure the effects of each one and obtain the result presented in Figure 1.3(b). Going further with this procedure one can obtain the succeeding "generations" of energy distributions shown in Figure 1.3(c). For a more quantitative discussion of these calculations see [2].

Until now we have considered target atoms at rest: this constitutes a good approximation for incident energies in the range of MeV but when neutrons approach thermal energies this is not true any more, since the thermal motion of the moderator is now comparable with the speed of neutrons. The elastic scattering can be better described using statistical mechanics, and assuming that after a sufficient time the neutrons will reach the thermal equilibrium with the moderator at a temperature T. In this case, the neutrons are described by the Maxwellian speed distribution:

$$f(v)dv = 4\pi n \left(\frac{m}{2\pi kT}\right)^{3/2} v^2 e^{-\frac{mv^2}{2kT}} dv \tag{1.3}$$

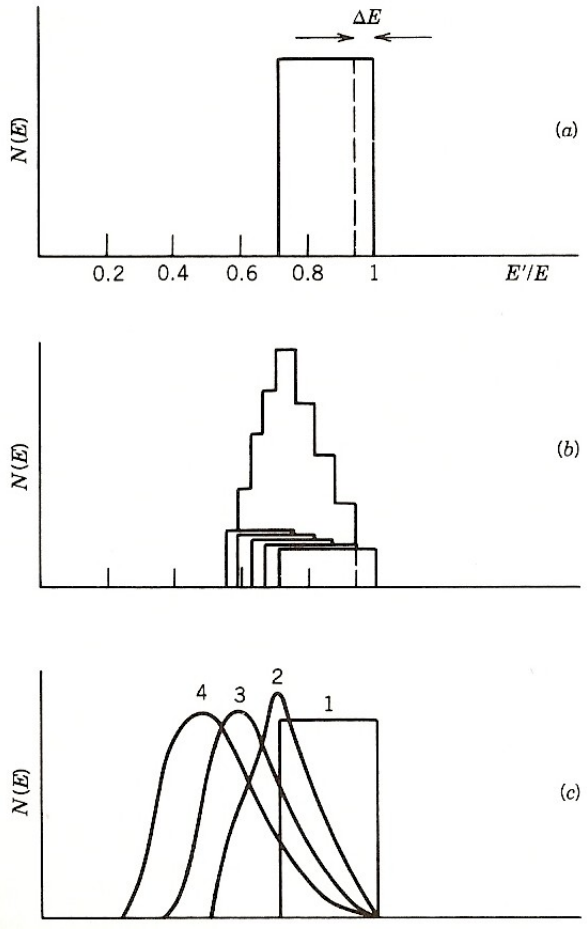

Figure 1.3: (a) A monoenergetic neutron of energy E gives, after a single scattering from an absorbed, a flat distribution of laboratory energies E' from 0.72 E to E. (b) Dividing the scattered distributions into five narrow, nearly monoenergetic distributios of width ΔE, we get after a second scattering the five flat distributions shown, whose sum in the peaked distribution. (c) An exact calculation of the energy distribution after 1, 2, 3 and 4 scatterings.

where $f(v)dv$ is the fraction of neutrons with a speed between v and $v + dv$, m is the neutron mass and n is the total number of neutrons per unit volume. In terms of energy (1.3) becomes:

$$f(E)dE = \frac{2\pi n}{(\pi kT)^{3/2}} E^{1/2} e^{-\frac{E}{kT}} dE \tag{1.4}$$

1.2.2 Inelastic scattering

In inelastic scattering the target nucleus is excited after the collision with the neutron. Schematically the reaction is:

$$\mathrm{n} + {}^{A}_{Z}X \rightarrow \mathrm{n} + \left[{}^{A}_{Z}X\right]^{*}$$

The incident neutron is absorbed by the target nucleus forming an unstable compound which quickly emits a neutron of lower kinetic energy. Since it still has some excess energy it goes through one or more γ-decays to return to the ground state.

1.2.3 Transmutation Reactions

In this type of reactions an element changes into another one. Neutrons of all energies are capable of producing transmutations. The most popular example of transmutation reaction is

$$\mathrm{n} + {}^{10}_{5}\mathrm{B} \rightarrow \begin{cases} {}^{7}_{3}\mathrm{Li} + \alpha & \mathrm{Q} = 2.792\ \mathrm{MeV}\ (\mathrm{ground\ state}) \\ {}^{7}_{3}\mathrm{Li}^{*} + \alpha & \mathrm{Q} = 2.310\ \mathrm{MeV}\ (\mathrm{excited\ state}) \end{cases} \tag{1.5}$$

When thermal neutrons induce the reaction, about 94% of them leads to the ^{7}Li excited state and only 6% to the ground state. In both cases, the Q value is so large

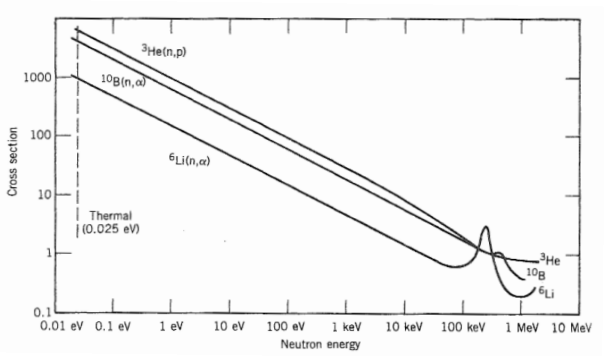

Figure 1.4: Cross section versus neutron energy for some interesting reactions. Notice the trend proportional to v^{-1} above 1 keV and the appearance of resonances around 100 keV.

compared to the incoming energy of the neutron, that the energy of the reaction products is just the Q value itself. Therefore it is impossible to extract any information about the original value of the incoming neutron.

Individual energies of the α particle and Lithium nuclei can be calculated using energy and momentum conservation laws. If one considers the case of populating the excited state of ^{7}Li, the result is 0.84 MeV for lithium and 1.47 MeV for α particles.

In Figure 1.4 the cross sections as a function of the neutron energy are shown for the reactions 1.5 as well for the following two:

$$^{6}\mathrm{Li} + \mathrm{n} \rightarrow {}^{3}_{1}\mathrm{H} + \alpha \qquad \mathrm{Q} = 4.78\,\mathrm{MeV} \tag{1.6}$$

$$^{3}\mathrm{He} + \mathrm{n} \rightarrow {}^{3}_{1}\mathrm{H} + \mathrm{p} \qquad \mathrm{Q} = 0.764\,\mathrm{MeV} \tag{1.7}$$

1.2.4 Radiative Capture

Radiative capture is a very common reaction involving neutrons. In such a reaction, a nucleus absorbs the neutron and goes into an excited state. To return to a

stable state, the nucleus emits γ-rays. In this case no transmutation occurs, however the mass of the absorbing nucleus changes due to an increase in the number of neutrons. The reaction can be represented like this:

$$n + {}^{A}_{Z}X \rightarrow {}^{A+1}_{Z}X + \gamma$$

Radiative capture is generally used to produce radioisotopes, such as ^{60}Co:

$$n + {}^{59}\,Co \rightarrow {}^{60}Co + \gamma$$

1.2.5 Spallation

Spallation refers to the fragmentation of a nucleus into several parts when a high energy neutron collides with it. This process is important only with neutrons having energy greater than about 100 MeV.

1.2.6 Neutron-induced Fission

In fission a slow neutron is captured by a heavy nucleus, such as ^{235}U, with the consequence of exciting it. Afterwards fission occurs, a part from the heavy fragments produced, also γ-rays and other neutrons can be emitted. As an example, the most probable decay channel for ^{235}U is

$$n + {}^{235}_{92}U \rightarrow {}^{139}_{39}I + {}^{95}_{53}Y + 2n + \gamma$$

and its cross section is shown as a function of the neutron energy in Figure 1.5. The plot illustrates also the cross section for other neutron-induced fission reactions. It is noteworthy the trend of cross section for a fission process in some material ( ).

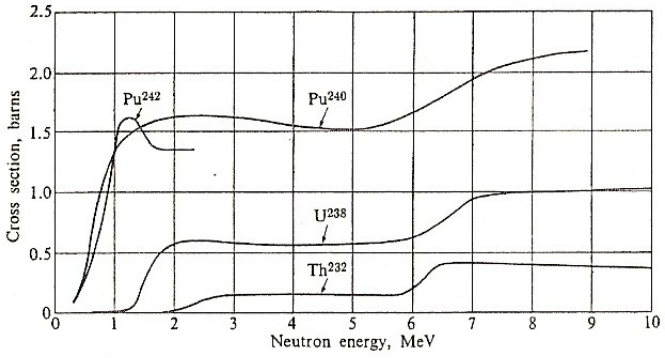

Figure 1.5: Fission cross section for ^{242,240}Pu, ^{238}U and ^{232}Th as a function of the incident neutron energy. .

1.2.7 Total Cross Section

The total neutron interaction cross section is the sum of the cross sections of each precess discussed above.

$$\sigma_t = \sigma_{\text{elastic}} + \sigma_{\text{inelastic}} + \sigma_{\text{trans}} + \sigma_{\text{capture}} + \sigma_{\text{spall}} + \sigma_{\text{fission}}$$

In Figure 1.6 it is reported the total cross section for neutrons with energy up to 200 MeV. It is obvious that at very low energy the cross section varies more if compared with higher energies.

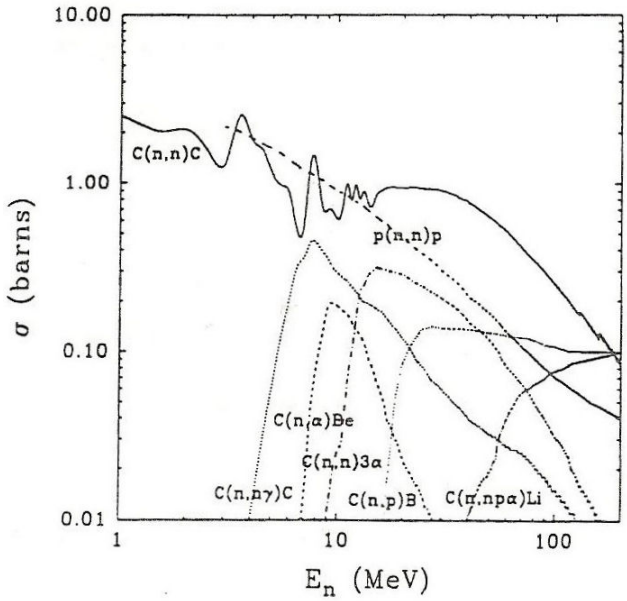

Figure 1.6: Neutron interaction cross section with C e H. Experimental values.

1.3 Neutron Detectors

We are now going to describe the properties of the two main categories of neutron detectors: fast and slow neutron detectors [3].

1.3.1 Slow Neutron Detectors

Slow neutron detectors are mainly based on transmutation reactions [3] involving Boron or Lithium as capturing nuclei. The interaction is observed detecting the charged particles emitted from the transmutation reaction. Geometry and dimensions of the detector play a fundamental role. The protons and α particles produced do not have to exit the active volume of the detector neither to interact with its walls since: in the former case only a fraction of energy is deposited, in the latter case signals with a small amplitude are produced.

A widely used detector is the **BF_3 proportional tube** where Boron Trifluoride serves both as the target for slow neutron conversion into secondary particles as well as a proportional gas counter. Although a number of other Boron-containing gases have been evaluated, BF_3 is the near-universal choice because of its superior properties as a proportional gas (it is often enriched in ^{10}B in order to increase the efficiency), as well as its high concentration of Boron. The typical pressure of operation of these detectors is between 0.5 and 1 atm since BF_3 does not work well as a proportional chamber if pressure is higher.

In a **Boron-lined proportional counters**, the Boron in the form of a solid coating is introduced in the interior walls, filled with a proportional gas like noble gases to obtain a fast timing response. The reaction occurs in the solid coating and the products are detected by the proportional gas. For this reason, since the α particles range is of the order of $1\,mg/cm^2$, the thickness of the coating must remain below this value, otherwise the efficiency will decrease.

^{3}He proportional counters were used as slow neutron detectors due to the high cross section of the reaction (1.7). The main disadvantage of these devices is that ^{3}He price has grown impressively in the last years.

Organic scintillator doped with ^{10}B are also widely used. They show several advantages with respect to proportional counters, in terms of timing response and efficiency. They are solid or liquid materials that often display good discrimination properties between neutron and γ-rays induced signals.

1.3.2 Fast Neutron Detectors

A quite widespread technique used to detect fast neutrons and that allows the applicability of the techniques presented in the previous section, is based on the moderation of neutron slowing them down before they reach the detector. The detector is surrounded by a few centimeters of light material, such as Hydrogen, that constitutes the moderating material. Within the moderator a neutron behaves in one of the following ways, depending on its energy and on the dimensions of the moderator (Figure 1.7):

- It can be thermalized and detected.
- It can preserve enough energy to escape the detector. In this case, in order to detect it, there can be a neighbouring detector but in the case of energy measurements the information is lost.
- It can loose too much energy to reach the detector and be absorbed by the material. In this case there is no way to detect it and this cause loss of information and decrease of efficiency.

Detectors based on this technique are for example **spherical dosimeters** and **long counters** [3]. Notice that for all these devices the common denominator is the utilization of BF_3 tubes or ^{3}He proportional counters, surrounded by a volume of light materials.

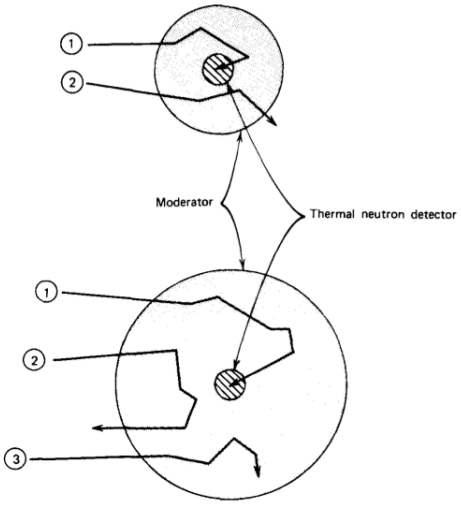

Figure 1.7: Moderation processes in two different size material volumes : 1) neutron has been thermalized and correctly detected 2) neutron has been moderated but escapes the detector 3) neutron has been absorbed by the moderator.

This solution entails the strong limitation of not giving any information about energy of the incoming neutron and it does not allow to reach high efficiency also because the time taken by neutrons to undergo moderation is long. To overcome this problem, one may rely on elastic scattering between the neutron and a nucleus of the material. We refer to 1.2.1 for the detailed discussion about elastic scattering. We only remind that, as the target mass is similar to that of the neutron as much energy is transfered to the recoiling particle.

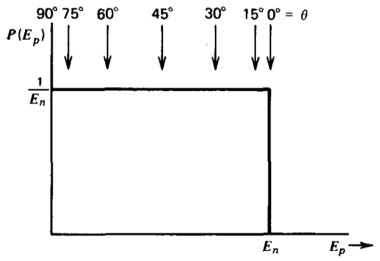

Figure 1.8: Energy distribution of the recoil proton heated by neutrons. The distribution ranges from zero to the full neutron energy. Recoil energies are indicated for various values of the recoil emission angle.

For this reason lightweight elements, such as Hydrogen, Deuterium or Helium, are targets preferred to make **"proton recoil detectors"**. The easiest way to build this type of detectors consists in the use of organic scintillators because they are rich in lightweight elements. Since the range of the recoil products is usually small compared with the dimensions of the scintillator, their full energy is released in the scintillator and the typical fast neutron spectrum is obtained, a rectangular distribution ranging from zero to the full neutron energy (Figure 1.8).

Successful applications have been reported using organic crystals such as anthracene or stilbene [5,6], as well as liquid or plastic scintillators. Many organic crystals have a large light output and allow for γ-rays rejection but are difficult and expensive to obtain in large sizes (greater than few centimeters in dimension) and are subject to damage from thermal and mechanical shock. Generally the use of liquid or plastic scintillator is preferred due to their lower cost and high flexibility in terms of sizes and shapes. Moreover liquid scintillators are usually preferred because of their properties of neutron-γ discrimination.

A valid alternative to the organic scintillators are **gas recoil proportional counters**. In these applications, the fill gas is usually Hydrogen or Hydrogen-containing gas such as methane, or some other low-Z gas such as Helium. These devices have a lower counting efficiency than typical organic scintillators because the detection medium is a gas with low density.

In all these cases, apart from the neutron-proton interaction, one cannot neglect the interaction between neutrons and carbon through the following reactions:

$$^{12}\mathrm{C} + \mathrm{n} \rightarrow \alpha + {}^{9}\mathrm{Be} \tag{1.8}$$

$$^{12}\mathrm{C} + \mathrm{n} \rightarrow \mathrm{n} + 3\alpha \tag{1.9}$$

The threshold energy of these reactions is 6.17 MeV and 7.98 MeV respectively but they start being significant above 9 MeV .

In conventional organic scintillators or recoil proportional counters, the measurement of the full energy spectrum of charged products of the reactions is not sufficient to give a reliable estimate of the incident neutron energy. In fact, the recoil nuclei carry only a fraction of incident energy as a function of the scattering angle and without this information there is no possibility of drawing quantitative conclusions. To solve the problem it has been developed the so **called proton recoil telescope**. In these devices the proton recoils that occur at a fixed angle with respect to the neutron direction, are singled out so that the recoil proton energy is fixed for monoenergetic neutrons. Thus, the energy of recoil protons observed at an angle θ with respect to the incoming neutron direction is given simply by

$$\mathrm{E_p} = \mathrm{E_n} \cos^2\theta \tag{1.10}$$

A schematic diagram of a common form of recoil telescope is shown in Figure 1.9.

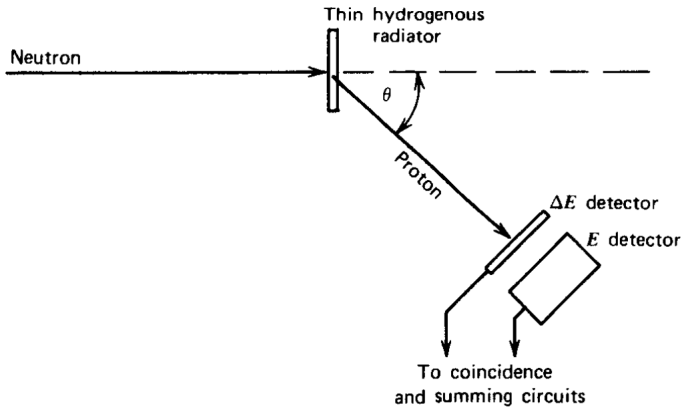

Figure 1.9: A proton recoil telescope

The angle θ at which recoil protons are observed is defined by positioning a detector some distance from the radiator, with the intervening space evacuated to prevent proton energy loss. Because of the $\cos^2\theta$ fall-off of recoil proton energy, the

detector is usually positioned at a small angle with respect to the neutron direction. Many designs put the proton detector at $\theta = 0°$, but others choose a finite observation angle to avoid neutron-induced background events in the detector from the primary beam.

The pulse height spectrum produced by monoenergetic neutrons in a typical organic or plastic scintillator shows a broad continuum that stretches from zero amplitude up to the equivalent of the full neutron energy. This continuum reflects the energy of single or multiple recoil protons produced by the fast neutron in its interactions within the detector, sometimes neutrons enter the scintillator and then escape. The ideal pulse height spectrum is a single peak for monoenergetic neutrons. An alternative approach that comes closer to this ideal is supplied by **capture-gated neutron spectrometer**, in which we have a reasonably large plastic scintillator that has been loaded with a small percentage of ^{10}B.

Because the fast neutron is travelling at a significant fraction of the speed of light, all the recoil protons are produced within a short period of time compared with typical pulse shaping times, giving rise to single output pulse which is the sum of the energy release of every single scattering event. Once the neutron has lost its energy through these multiple collisions, it continues to diffuse as a thermal neutron within the scintillator. If a sufficient Boron concentration is present, the high cross section for capture in ^{10}B will predominate, and virtually all thermalized neutrons will be captured by Boron nuclei. In most of these capture events, some energy is released as kinetic energy of heavy charged particles giving rise to a second pulse of light. The average time separation between the light produced by the recoil protons and the light produced by the Boron capture products is about 10 μs.

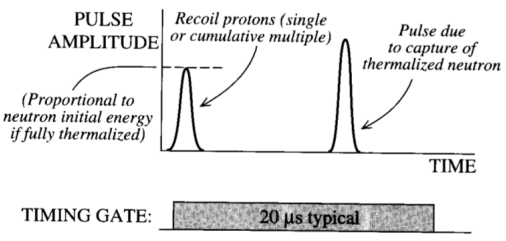

Figure 1.10: Sequence of two pulses expected from a captured-gated neutron spectrometer when the incident fast neutron is thermalized and captured.

Thus we have a unique signature that can be used to single out just those neutrons that lose all their energy in the detector. That signature is a pulse (produced by the multiple recoil protons) that is followed within 10-20 μs by a second pulse that corresponds to the capture in ^{10}B (Figure 1.10). The neutrons entering the detector, creating one or more recoil protons and escaping are rejected because a second pulse does not occur as in the case of full energy deposition. These techniques however, are very difficult to implement because the detection of the proton recoils presents several experimental complications.

The most common way to determine the energy is the the measure of **time of flight** (TOF). In this case we need to measure the time taken by a neutron, after it has been produced, to reach the detector placed at a fixed and known distance. To measure the TOF it is necessary to have a signal that identifies the emission of the neutron (start) and a signal that designates the arrive of the neutron to the detector (stop). The stop is usually given by a neutron detector with suitable properties

of neutron-γ discrimination. Concerning the start there are two possibility: in the study of nuclear reactions the use of a pulsed beam is very common, otherwise a fast γ-rays detector is situated very close to the reaction point so that the detection of an events corresponds to the emission of a neutron since γ-rays are produced simultaneously with the neutron. The greater the distance between the reaction point and the detector, the better is the precision of TOF measurement. On the other hand, the solid angle under which the detector sees the radiator is reduced and, unless the number of detector is increased, the acceptance makes worse. Moreover, depending on the frequency (i.e. if the beam is pulsed at high frequency) there is the risk that the slow neutrons signals are superimposed to the fast ones of the following event. For this reason it is defined the maximum frequency of detectable events as follows

$$\nu_{\mathrm{max}} = \frac{1-\alpha}{\mathrm{D}\left(\sqrt{\frac{\mathrm{m}}{2\,\mathrm{E_{min}}}} - \sqrt{\frac{\mathrm{m}}{2\,\mathrm{E_{max}}}}\right)} \tag{1.11}$$

where α is the duty cycle, that is the fraction of time occupied by the beam, D is the distance of flight, m is the mass of neutron and E_{min} and E_{max} are the minimum and the maximum energy of neutrons respectively. For example, at a distance D = 2 m, a duty cycle of 5% and an energy range between 5 MeV and 100 MeV, the maximum frequency is 18.9 MHz.

Chapter 2

Scintillation Detectors and Photodetectors

This thesis is focused on neutron detectors and in particular on scintillation materials that can detect neutron as well as γ radiation allowing their discrimination. In this chapter we will summarize the general scintillation mechanisms for organic materials and how these are connected with their performances in terms of efficiency and reliability [3,7,8]. Scintillation detectors are widely used in many fields of experimental physics. The scintillation process is one of the most useful methods available for the detection and spectroscopy of neutral and charged particles. The physical process over which these detectors are based is called *luminiscence*: when the incident radiation loses energy interacting with the scintillating material, its constituent atoms or molecules are excited to short lived configurations. The subsequent de-excitation process results in an emission of photons usually in the UV-visible regions. This light has then to be collected and converted in an electrical signal for further acquisition and processing. The basics steps involved in scintillation detection are:

- Interaction of the radiation with the scintillation material
- Energy transfer to the bound states of the material
- Relaxation of the excited states to the ground state resulting in the photon emission
- Collection of photons by a photodetector
- Detection of the photodetector signal by the associated electronics.

A scintillation detector is composed of two elements: the scintillating material and the photodetector. Sometimes a light guide is required for geometrically fit the scintillator with the phtodetector entrance window. Moreover optical grease can be used for optimizing the coupling between the two parts.

The scintillating materials are divided in two main categories: **organic** and **inorganic**, which differ in chemical composition, absorption and emission mechanisms.

With the exception of noble liquids, inorganic scintillators are usually crystalline solids, whereas organic scintillators can be liquid or gaseous compounds or made by some particular polymers such as rubber or elastomers. An ideal scintillation material should have the following properties:

- it should have **high scintillation efficiency**: it should convert most of the deposited energy of charged particles into detectable light;
- the conversion should be proportional to deposited energy (**linearity**) in order to easily calibrate the device and to obtain uniform resolution in the working energy range;
- the medium should be **transparent** to the wavelength of its own emission (i.e. little overlap between the emission and the absorption light spectra)
- the decay time of the induced luminiscence should be as short as possible in order to generate fast signal pulses;
- the material should be of good optical quality in order to permit a good optical coupling with the photodetector. The refraction index of the different pieces should be as similar as possible to avoid diffractive effects and maximize transmission [1];
- a good matching between the emission spectra and the sensibility interval of the photodetector.

It is evident that the choice of the scintillation material is fundamental in order to develop a good quality instrument. In this work we will study the pulse shape discrimination properties of siloxane scintillators in liquid (oligosiloxane) and solid (polysiloxane) form, therefore we are now going to introduce the typical scintillation mechanisms and the light output properties of organic scintillators. At the end of this chapter we will also discuss the main operation of photodetectors used in this thesis, such as photomultipliers tube and silicon photomultipliers.

2.1 Scintillation Mechanism in Organic Scintillators

The fluorescence process arises from transitions in the energy level structure of a single molecule and then can be observed from a given molecular species independent on its physical state [9]. For example, anthracene is observed to fluoresce either as a solid polycrystalline material or as a vapor, or as a part of a multicomponent solution. For this reason organic scintillators can be either solid or liquid or gaseous.

The characteristics of light absorption and emission are determined by the energetic structure of molecular orbitals. Those are obtained from the combination

[1] According to geometrical optics the optimal matching between two materials with refraction index n_1 and n_2 can be obtained inserting a third material with refraction index $\sqrt{n_1 n_2}$ between them.

of atomic orbitals, which predict the location of an electron in an atom. If the orbital lies along the conjunction between nuclei it is called a σ-orbital, whereas if the orbital extends perpendicularly to the conjunction it is called π-orbital. The π elec-

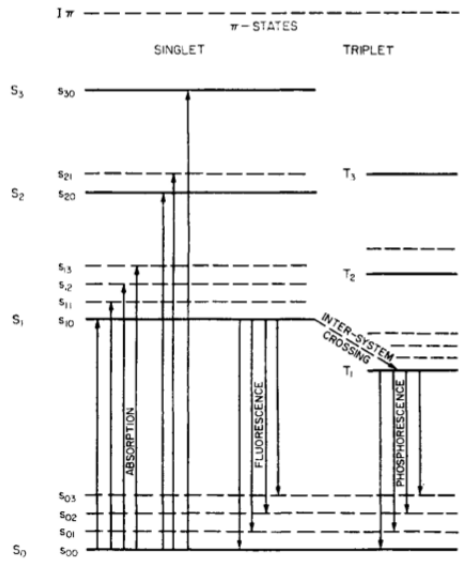

Figure 2.1: π-Electronic energy levels of an organic molecule. S_0, ground state. S_1, S_2, S_3 excited singlet states. T_1, T_2, T_3 excited triplet states. S_{00}, S_{01}... S_{10}, S_{11}... etc. vibrational sub-levels. I_π, π-ionization energy.

tronic energy levels for a molecule are illustrated in Figure 2.1. A sequence of singlet states (spin 0) labelled as S_0, S_1, S_2, ... with energy 0, E_1, E_2 ... can be observed up to the π-electron ionization energy I_π. The typical spacing between singlet states is of the order of $1.5 - 4$ eV. Each of these electronic levels is further subdivided into a series of vibrational levels spaced tens of meV apart. These levels are usually denoted with a second subscript, i.e. S_{00}, S_{01} and so on. A similar set of triplet (spin 1) electronic energy levels, T_1, T_2, T_3 ... each lower in energy than the corresponding singlet state, can be observed in the Figure 2.1. Although the absorption transition from S_0 to T_1 is spin-forbidden, the triplet states may be populated as we will see in the following.

In Figure 2.1 the absorption of energy by the molecule is represented by the arrows pointing upward. The higher singlet electronic states that are excited are quickly (on the order of picoseconds) de-excited to the S_1 electron state through radiationless internal conversion. Furthermore, any state with excess vibrational energy (such as S_{11} or S_{12}) is not in thermal equilibrium with its neighbours and again quickly loses vibrational energy. Therefore, the net effect of excitation process in a simple organic crystal is to produce after a negligibly short time period, a population of excited molecules in the S_{10} state. Afterwards, prompt fluorescence light is emitted in transitions between this state and one of the vibrational levels of the ground state. These transitions are indicated with arrows pointing downward in Figure 2.1. If τ represents the fluorescence decay time for S_{10} level, then the

prompt fluorescence intensity at a time t following the excitation should simply be

$$I = I_0 \, e^{-t/\tau} \tag{2.1}$$

Usually τ for organic scintillators is of the order of few nanoseconds.

Regarding the triplet states, the lifetime for T_1 states is much longer than the one of the first singlet state. The triplet state T_1 can be reached through a process called intersystem crossing, and since the lifetime of T_1 is about 10^{-3}s, the radiation emitted to reach the ground state is a delayed light emission known as phosphorescence. Sometimes it could occur that some molecules may be thermally excited back to S_1 level giving rise to delayed fluorescence

Thanks to Figure 2.1 we can also explain why organic scintillators can be transparent to their own fluorescence emission. The length of the upward arrows corresponds to the energies of photons that are strongly absorbed in the material. The downward arrows instead are shorter (except for the transition $S_{10} - S_{00}$) because the energy is lower than the minimum required for excitation. Thus the emission and absorption spectra show a small overlap (see Figure 2.2) and consequently there is a little self absorption of the fluorescence. This effect is called Stokes shift.

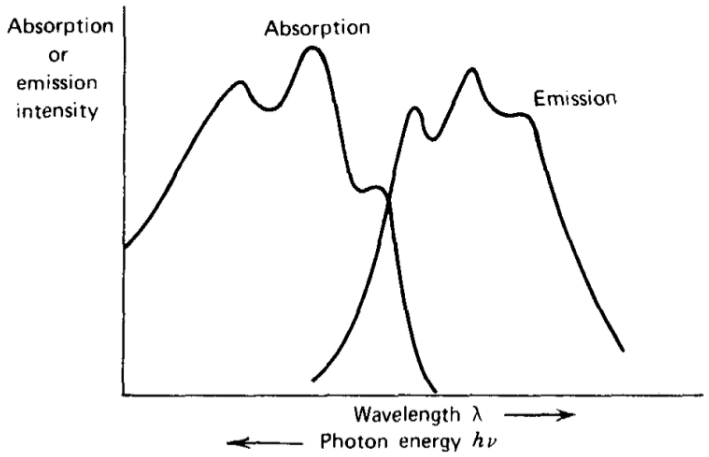

Figure 2.2: The optical absorption and emission spectral for a typical organic scintillator with the level structure shown in Figure 2.1.

In Table 2.1 the characteristic time of the processes occurring inside an organic scintillation material are summarized [9].

Table 2.1: Characteristic times of the main processes occurring inside an organic scintillation material.

Phenomenon	Characteristic Time
absorption	10^{-15} s
vibrational relaxation	$10^{-10} \div 10^{-10}$ s
lifetime of the excited state S_1	$10^{-10} \div 10^{-7}$ s
intersystem crossing	$10^{-10} \div 10^{-8}$ s
lifetime of the excited state T_1	$10^{-6} \div 1$ s

2.2 Response of Organic Scintillators

We describe the response of the organic materials in terms of energy conversion in photons and light yield.

2.2.1 Scintillation Efficiency

The **scintillation efficiency** is the ratio between the total energy of scintillation photons and the energy lost by the incident particle:

$$\eta = \frac{\text{Total Energy of Scintillation Photons}}{\text{Energy Deposited by Incident Particle}} = \frac{E_s}{E_i} \tag{2.2}$$

where the subscripts i and s stands for incident and scintillation respectively.

Scintillation efficiency is limited by de-excitation modes available to the excited molecules that do not involve the emission of light and in which the excitation is degraded mainly to heat (phonons). All such radiationless de-excitation processes are grouped together under the name of quenching and will be described in 2.2.3. In the fabrication and use of organic scintillators it is always important to eliminate impurities (such as dissolved oxygen in liquid scintillators), which degrade the light output by providing alternate quenching mechanisms for the excitation energy.

In almost all organic materials, the excitation energy undergoes substantial transfer from molecule to molecule before de-excitation occurs. This energy transfer process is especially important for the large category of organic scintillators that involve more than one species of molecules. If a small concentration of an efficient scintillator is added to a bulk solvent, the energy that is absorbed, primarily by the solvent, might eventually reach one of the efficient scintillation molecules and cause light emission at that point. These "binary" organic scintillators are widely used both as liquid and plastic solutions incorporating a variety of solvents and dissolved organic scintillants.

A third component is sometimes added to these mixtures to serve as a "wavelength shifter." Its function is to absorb the light produced by the primary fluorophore and reradiate it at a longer wavelength. This shift in the emission spectrum

can be useful for closer matching to the spectral sensitivity of a photomultiplier tube or to minimize bulk self-absorption in large liquid or plastic scintillators.

2.2.2 Light Yield

If the scintillation efficiency is independent of energy, a linear dependence of light yield on initial energy results. Most organic scintillators, such as anthracene or stilbene, have a linear response to electrons for particle energies above 125 keV. The response to heavier particles such as protons or alpha particles, is always less for equivalent energies and is nonlinear to much higher initial energies.

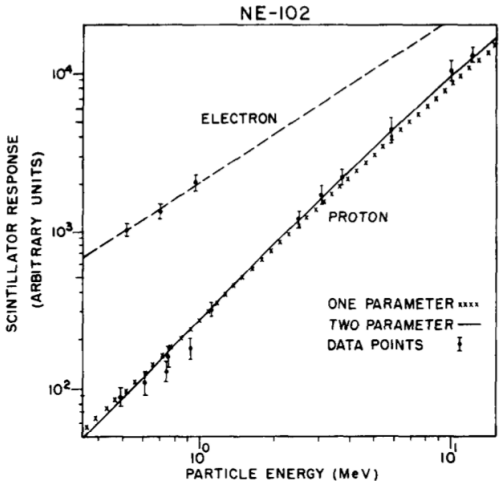

Figure 2.3: The scintillation light yield for a plastic scintillator (NE102) when excited by protons and electrons.

In Figure 2.3, the scintillation light yield of a typical plastic scintillator (NE102) for protons and electrons is shown. At energies of few hundreds of keV the proton light yield is an order of magnitude smaller than the light yield of equivalent energy electrons. At higher energies the discrepancy is less but proton response is always below the electron response. This effect, is observed in all the organic scintillators and requires to introduce the concept of eV electron equivalent (eV_{ee}). The particle energy required to generate 1 eV_{ee} of light yield by definition is 1 eV for electrons but several eV for heavy charged particles because of their reduced light yield per unit energy. This relation is material dependent, as an example see [10] where the NE213 liquid scintillator is studied.

The response of organic scintillators to charged particles can be best described relating dL/dx (the fluorescent energy emitted per unit path length) with dE/dx (the specific energy loss per unit path length for a charged particle). If the incident particle is an electron with energy of about 1 MeV, the energy loss dE/dx is low and the ionizations and molecular excitations originated by it, occur in spaced positions along the particle track, so they do not affect the scintillator response. Under these conditions, the scintillator response L is proportional to the energy lost by the particle in the material:

$$L = SE \leftrightarrow \frac{dL}{dx} = S\frac{dE}{dx} \tag{2.3}$$

where S is the normal scintillation efficiency. In case of heavy particles the scintillation response is nonlinear at low energy. Therefore we must keep in mind that in case of high ionization density the quenching factors are no more negligible because processes of molecular damage and energy absorption intervene. If we assume that the density of damaged molecules is directly proportional to the ion-

ization density by $B(dE/dx)$, where B is a proportionality constant, we can re-write (2.3) as follows

$$\frac{dL}{dx} = \frac{S\frac{dE}{dx}}{1 + kB\frac{dE}{dx}} \tag{2.4}$$

which is known as Birks' formula [8]. Equation (2.4) should be considered as an empirical approach to the light yield problem. As a practical matter the product kB is treated as an adjustable parameter to fit experimental data for a specific scintillator. In many cases, this single adjustable parameter can give very good fits to the shape of experimental data. However, sometimes this approach has to be improved introducing a quadratic terms in the energy loss and a constant C

$$\frac{dL}{dx} = \frac{S\frac{dE}{dx}}{1 + kB\frac{dE}{dx} + C\left(\frac{dE}{dx}\right)^2} \tag{2.5}$$

2.2.3 Quenching

The decrease in light output of a scintillator due to the change of some parameters (temperature, energy of the incident radiation, impurity, or concentration of its constituents, etc) is called **quenching**. We now describe the main quenching processes.

Thermal quenching. Large temperature changes that can lead to thermal recombination effects of excited states and to the enlargement of vibrational levels decrease the light output in some scintillation materials . The light output decrease induced by temperature increase is generally referred to as thermal quenching. However this problem is relevant only for few scintillators showing a strong enough dependence on temperature.

Energy quenching. The energy delivered by the incident radiation determines the light output of a scintillator. However this process is not linear and eventually saturates. Delivering more energy to the scintillator, beyond a certain stopping power that depends on the material, does not affect the light output. When such a state is reached, the material is said to have suffered energy quenching. This effect is most pronounced in organic scintillators.

Impurity quenching. In some types of scintillation materials the impurities cannot only decrease the light output but can also affect the optical properties of the material itself. This type of quenching may require the use of high purity components for the synthesis of some scintillating materials .

Self-quenching. Usually the scintillating materials are actually mixtures of two or more elements. The light yield of the scintillators depends on the concentration of their constituents. In most of them, the light output increases with the concentration of the primary fluorophore but then after reaching a certain value it gets saturated.

Mechanical properties. Solid scintillators are subjected to cuts and abrasions during surface cleaning, and this may cause internal damage (crack) if the structure is not resistant enough. Many scintillators are particularly sensitive and flimsy due to the vulnerability to atmospheric agents. For example there can be variations in optical properties of liquid solutions as a function of temperature.

2.2.4 Time Response

If it can be assumed that the luminescent states in an organic molecule are formed instantaneously following the absorption of radiation and only prompt fluorescence is observed, then the time profile of the light pulse should be a very fast increase followed by a simple exponential decay (see equation 2.1). Although this simple representation is often adequate a more detailed model of the time dependence of the scintillation yield must take into account three other effects: the finite time required to populate the luminescent states, the slower components of the scintillation corresponding to delayed fluorescence and phosphorescence and the scintillator geometry. The time evolution of the light pulse can be described by the following expression:

$$I = I_0 \left(e^{-t/\tau} - e^{-t/\tau_1} \right) \tag{2.6}$$

where τ_1 is the rise time constant and τ is the fall time constant describing their decay. the decay time constants of a scintillator can be measured using the Bollinger-Thomas single photon method [11]. In section 6.1 we will apply this technique to characterize the time response of the materials tested in this work.

2.2.5 Pulse Shape Discrimination

Most of the observed scintillation light, for a majority of organic materials, is due to prompt fluorescence. In many cases, however, the delayed fluorescence discussed in section 2.1 can produce longer-lived components that can also be observed. A sum of two or more exponential decays, called the fast and slow components of the scintillation, often represents adequately the composite yield curve. Typically, the slow component has a characteristic decay time of several hundred nanoseconds to be compared with the prompt decay time of a few nanoseconds. Since the majority of the light yield occurs in the prompt component, the long-lived tail would not be of great consequence except for one very useful property: **the fraction of light that appears in the slow component often depends on the nature of the exciting particle**. Indeed, it is usually employed to differentiate between different particles impinging in the detector. This process is often called pulse shape discrimination and is widely applied to eliminate γ-ray-induced events when organic scintillators are used as neutron detectors.

Certain organic materials, including stilbene crystals and a number of commercial liquid scintillator, are particularly favored for pulse shape discrimination because of the large differences in the relative slow component induced by different particles. Figure 2.4 shows the differences observed in stilbene for α particles, fast neutrons (recoil protons), and γ-rays (fast electrons resulting from the interaction

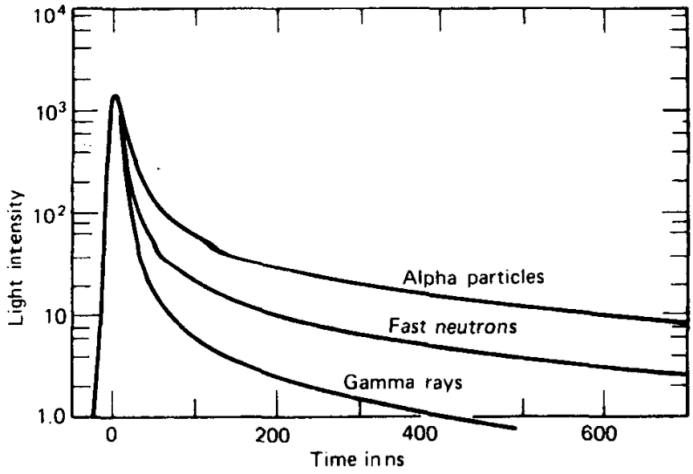

Figure 2.4: The time dependence of scintillation pulse in stilbene, when radiated by alpha particles, fast neutrons or γ-rays.

of γ-rays with matter through photoelectric effect, Compton scattering or pair production). In such scintillators, it is not only possible to differentiate particles with different energy deposition densities (such as neutrons and γ-rays) but also to separate events arising from various species of heavy charged particles as well. As we will see in the next chapters, one of the purposes of this work is to apply the main methods of pulse shape discrimination, on liquid and solid siloxane scintillators designed at Legnaro National Laboratories (LNL) .

2.3 Commercial Organic Scintillators

One the most common liquid organic scintillator is the BC501 [12]. It emits at a wavelength of about 425 nm and has a fast decay time constant of 3.3 ns. Commercial alternatives are given by the NE213 or EJ301 [13]. Although it is one of the best organic scintillator able to discriminate γ-ray from neutron pulses [14–17] it has the disadvantage of being very toxic, flammable, volatile and polluting. For this reason the research of plastic or liquid alternative solutions is very active. As an example, the manufacturing of plastic scintillators with efficient neutron-γ pulse shape discrimination has been recently obtained [18] and put on the market as EJ299-33 [19]. Its pulse shape discrimination properties were recently studied in [20, 21].

EJ309 [22] is another commercial liquid scintillator recently manufactured which provides slightly poorer pulse shape discrimination characteristics than BC501 but does possess a number of chemical properties recommending it for use in environmentally difficult conditions [23] (less volatile). Its main characteristics are reported in Table 2.2 and in Figure 2.5.

Table 2.2: The main characteristics of the EJ309 commercial liquid scintillator (adapted from [22])

Properties	
Light Output (% Anthracene)	75%
Photons produced by a 1 MeV electron	11.5
Wavelength of Maximum Emission	424 nm
Decay Time, Short Component	$\sim$ 3.5 ns
Refractive Index n_D	1.57
Atomic Composition	
No. of H Atoms per cm^3	5.43×10^{22}
No. of C Atoms per cm^3	4.35×10^{22}
No. of Electrons per cm^3	3.16×10^{23}

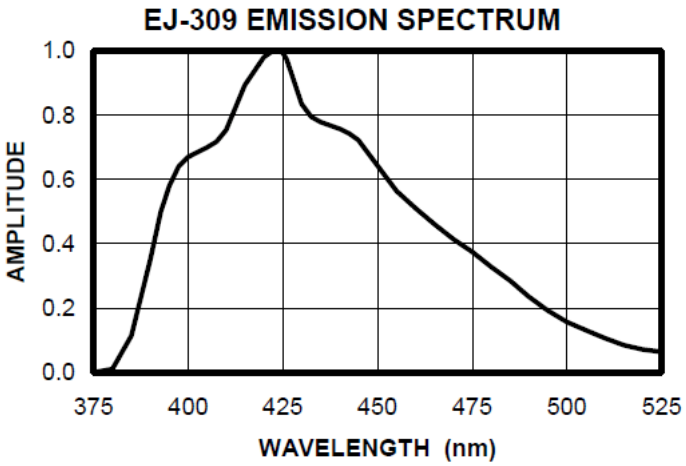

Figure 2.5: The emission spectrum for EJ309 (adapted from [22]).

2.4 Photodetectors

The light produced by scintillation must be converted into a corresponding electrical signal to be acquired and processed. In many applications it is necessary to put a light guide between the scintillator and the photodetector due to geometric or space reasons. Therefore the optical coupling between the elements involved is very delicate:

- the emission spectrum of the scintillation material must match as much as possible the acceptance range of the photodetector
- the components in contact between each other must have a refractive index as similar as possible

- the coupling is maximized by optical grease spread on the surfaces that maximizes the transmission

There are mainly two categories of photodetectors: photomultiplier vacuum tubes and solid state photodetector. The photomultiplier (PM) tube converts light signals into a usable current pulse without adding a large amount of random noise to the signal. Although the PM tube remains the most widely used device for this purpose, recently there has been some progress in the development of semiconductor photodetectors. In general, solid state photodetectors (SSPD) offer the advantages of higher quantum efficiency (and therefore the potential for better energy resolution), lower power consumption, more compact size and improved ruggedness compared with PM tubes. Their performances are not affected by magnetic fields and therefore they can sometimes be used in applications where magnetic fields prevent the use of PM tubes. Given the relatively small dimensions over which the charges must move in these devices, their time response is better than the one of conventional PM tubes.

2.4.1 Photomultiplier Tubes

A great variety of commercial PM tubes is available with different sensitivity to ultraviolet, visible or near-infrared photons. They have many applications in optical spectroscopy, laser measurement and astronomy.

The simplified structure of a typical photomultiplier tube is shown in Figure 2.6. An outer (usually glass) envelop serves as a pressure boundary to sustain vacuum conditions inside the tube that are required so that low-energy electrons can be accelerated efficiently by internal electric fields. The components inside the tube are primarily a cathode made of a photosensitive material (photocathode), an electron multiplier structure, that will be described shortly and an anode from which the signal is extracted. Between anode and cathode there is a constant potential difference usually equal to few thousands of volts .

The photons incident on the photocathode, release their energy emitting electrons due to the photoelectric effect. The energy of the latter is proportional to the energy of incident photons through the Einstein's law:

$$E = h\nu - \phi \tag{2.7}$$

where ϕ represents the extraction work that constitutes a detection threshold. This parameter depends on the photocathode material and usually it affects largely the sensitivity of the device. Beyond the threshold however, the probability of electron extraction is not the best because we have to take into account the quantum efficiency of the PM tube that connects the probability of photoelectron emission to the wavelength of the incident photons:

$$\eta(\lambda) = \frac{\text{Number of Photoelectrons Emitted}}{\text{Number of Incident Photons } (\lambda)} \tag{2.8}$$

These electrons have an energy of the order of few eV, and are not able to generate a relevant electric signal. For this reason they have to be accelerated and focused

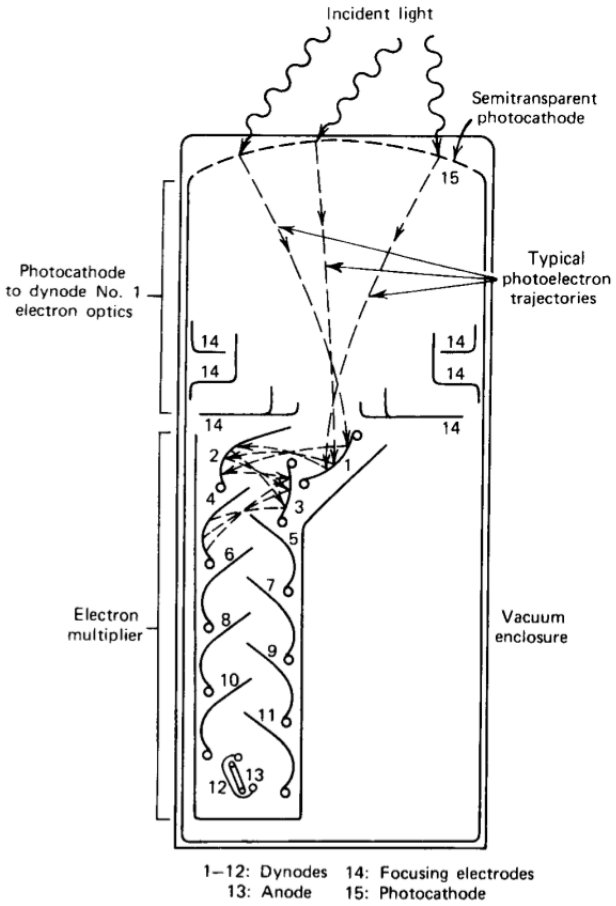

Figure 2.6: The simplified structure of a typical PM tube.

towards an amplifying process able to return an electric pulse high enough to be detected. The multiplier portion of a PM tube is based on the secondary electron emission. Electrons are accelerated and focused on an electrode called *dynode*. If the dynode material is chosen properly, the energy deposited by the incident electron can result in the re-emission of more than one electron from the same surface. The extraction of an electron from the dynode material requires an energy at least equal to the bandgap, which typically may be of the order of 2-3 eV. Therefore, if the potential difference between two dynodes is about 100 V, a gain factor of the order of 30 can be reached. Normally about 12 dynodes are employed. Only a fraction of the electrons exiting the i*th* dynode will contribute to the secondary emission in the following one due to geometrical inefficiencies and/or energy reasons. Therefore the secondary emission process is dominated by an overall multiplication factor:

$$\delta = \frac{\text{Number of secondary electrons emitted}}{\text{Primary incident electron}} \tag{2.9}$$

This factor should be as large as possible for maximum amplification per stage in the photomultiplier tube. The total gain of the PM tube is given by the product of

the gain per dynode δ and the fraction of photoelectrons really captured by the first dynode:

$$\text{Gain} \propto \delta^N \tag{2.10}$$

where N is the number of dynodes. Eventually typical gains achievable fall in the range $10^5 - 10^7$.

Hamamatsu Photomultiplier Tubes

The photomultiplier tubes that will be employed in this thesis coupled with liquid scintillator samples are the R1450 supplied by the Hamamatsu company [24] (19 mm diameter). Their spectra response ranges from 300 to 650 nm with the maximum at 420 nm. They are designed to operate at a maximum voltage between anode and cathode of 1800 V. They have a fast time response namely anode pulse rise time is 1.8 ns and the electrons transit time is 19 ns. In Figure 2.7(a) the quantum efficiency as a function of the wavelength is shown. Figure 2.7(b) illustrates the gain curve.

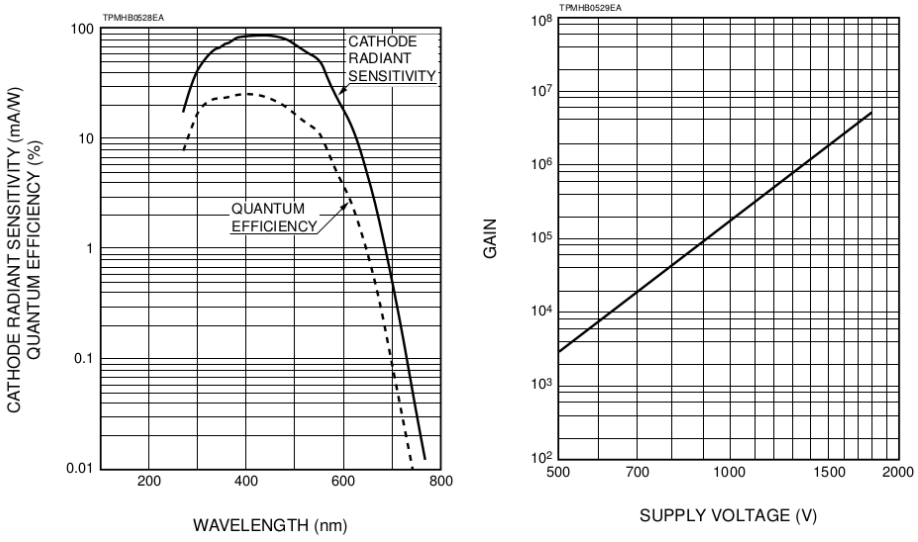

(a) Typical spectral response .

(b) Typical gain characteristics.

Figure 2.7: Characteristics curves for a R1450 PM tube [24].

The solid samples have been coupled with the R11833-100 photomultiplier from the Hamamatsu company [24] (127 mm diameter). Besides the geometrical size the R11833-100 PM tube differs from the R1450 for the maximum supply voltage (1500 V) and the time response (4.3 ns anode pulse rise time, 45 ns electron transit time). The quantum efficiency dependence from the wavelength is reported in Figure 2.8. For the measurements described in this work, both types of PM tubes have been operated at 1500 V.

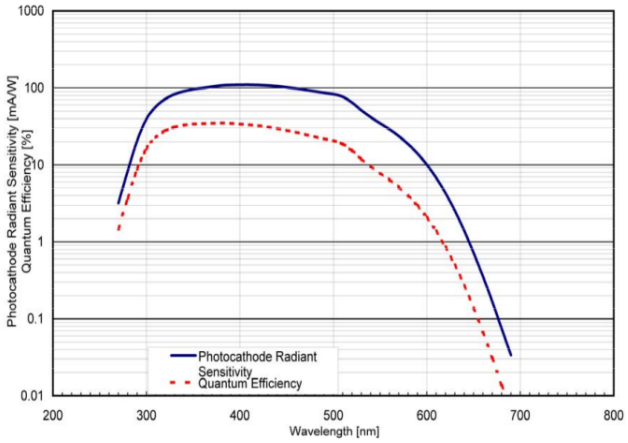

Figure 2.8: The quantum efficiency of the R11833-100 PM tube as a function of the wavelength [24].

2.4.2 SiPM

The silicon photo-multiplier (SiPM) [25] is a semiconductor device consisting in a matrix of tiny avalanche photo-diode pixels ($\sim 10^3/\text{mm}^2$) grown on a common silicon substrate and connected in parallel via integrated resistors. The diodes are operated in Geiger mode, i.e. biased at few volts above breakdown, so that any single carrier, generated either by photons or thermally in the depletion region, might trigger a self-sustaining avalanche which is quenched by the integrated resistors. Because all SiPM pixels work together on a common load, the output signal is the sum of the signals from all fired pixels: while each pixel is an independent binary photon counter (with a dead-time of $\sim$ 30 ns), the SiPM as a whole works as an analog detector (with negligible dead-time). High gain ($\sim 10^6$) and high efficiency (up to 80%) in detecting low optical photon fluxes with unprecedented charge resolution, extreme single photon timing resolution, low voltage operation and insensitivity to magnetic fields, radiofrequency pickup, make SiPM suitable for many applications, as an alternative to vacuum photo-multiplier tubes. The next chapter is dedicated to a detailed description of the SiPM devices.

Chapter 3

Silicon Photomultipliers

Silicon Photomultipliers (SiPM) [26] are light sensors able to count the number of photons impinging on their surface. They are sensitive to wavelengths from UV to NIR (near-infrared) region, with a specific peak sensitivity depending on the design. When coupled with scintillators they can be used to detect γ-rays for several applications, ranging from biomedical imaging (e. g. detectors for Positron Emission Tomography, PET) to fluorescence spectroscopy and astrophysics. A SiPM is an array of single photon avalanche photodiodes (SPAD) cells, each with dimensions of tens of micrometers, produced using either custom or CMOS processes on silicon. The size of the individual cell is small enough so that the probability to be hit by a photon is low, so that the number of cells producing an avalanche is proportional to the number of incident photons. Usually there are 10^3 or more cells in the array to match the number of scintillation photons produced usually in scintillators. The output of each cell when operated in Geiger mode has a very similar amplitude: the tiny fluctuations are due to little variations, cell geometry and quenching resistance (R_q) values. Then simply adding their output by connecting them in parallel produces an analogue pulse whose amplitude is proportional to the number of detected photons. We are now going to explain the theory of a silicon photomultiplier, starting from the definition of a p-n junction up to the analysis of the most performance parameters.

3.1 Theory of SiPM design

Before describing the SiPM working principles, it is convenient to recall some concepts of a p-n junction. In a p-n junction electrons of the n-zone (which are locally supernumerary) diffuse towards the p-zone and vice-versa holes diffuse towards the n-zone. This process reaches the equilibrium because the carriers leave behind positive and negative ions depending on the charge, which are fixed in the lattice and generate an electric field that prevent the movement of carriers. A carriers-lacking depletion layer it is then created (see Figure 3.1).

If the p-side of the junction is made negative with respect to the n-side, the junction is reverse biased. The natural potential difference from one side of the junction

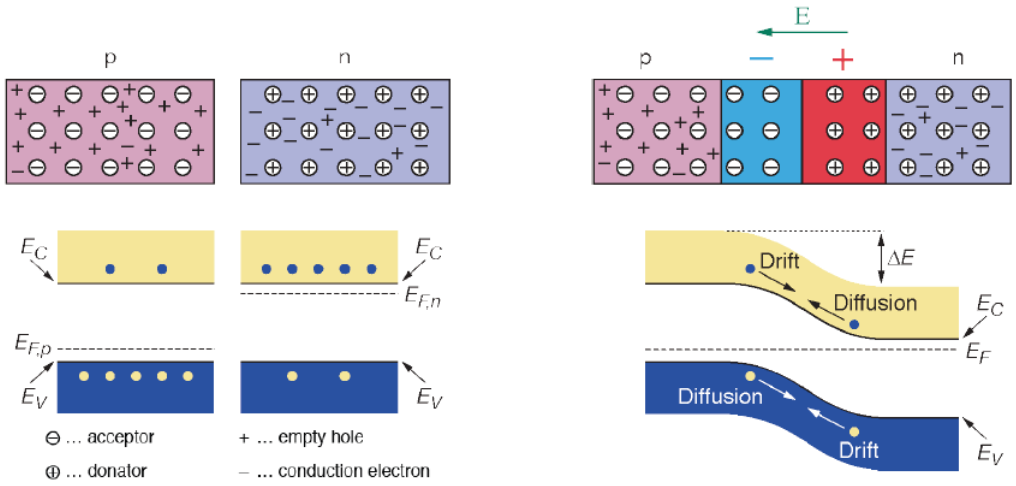

Figure 3.1: Formation af a p-n junction between a p-doped and an n-doped semiconductor.

to the other is enhanced. Under these conditions, the minority carriers (holes in the n-side and electrons in the p-side) are attracted across the junction and, since their concentration is relatively low, the reverse current across the diode is quite small. Because the effect of the reverse bias is to accentuate the potential across the junction, Poisson's equation demands that the space charge must also increase and extend to a greater distance on both sides of the junction. Usually practical detectors are operated with a bias voltage V that exceeds the contact potential so that the applied voltage dominates the magnitude of the potential difference across the junction. If we suppose that the junction is only partially depleted, we can derive the thickness of the depletion layer. Given the Poisson's equation:

$$\nabla^2 \Psi(x) = -\frac{\rho(x)}{\epsilon} \tag{3.1}$$

where $\Psi(x)$ is the potential, $\rho(x)$ is the net charge density and ϵ is the dielectric constant, one can derive the expression for the electric field across the depletion region:

$$E = -\frac{d\Psi}{dx} = \begin{cases} -\dfrac{eN_A}{\epsilon}(x + x_p) & -x_p \leq x \leq 0 \\ \dfrac{eN_D}{\epsilon}(x - x_n) & 0 \leq x \leq x_n \end{cases} \tag{3.2}$$

where N_A and N_D are the acceptor and donor atom concentration respectively and x_p and x_n are the width of the depletion layer in the p and n zones respectively. The electric field presents a triangular negative shape, having its minimum at the contact between the two different zones, and it cancels out beyond the depletion layer. Imposing the boundary condition for the potential, that is:

$$\Psi(x_n) - \Psi(-x_p) = V \tag{3.3}$$

and remembering the neutrality of space charges:

$$N_A x_p = N_D x_n \tag{3.4}$$

one can derive the thickness of the depletion layer W :

$$W = x_p + x_n = \sqrt{\frac{2\epsilon_s}{q}\left(\frac{(N_A + N_D)}{N_A N_D}\right)V} \tag{3.5}$$

Across the junction, the carriers move due to the effect of drift field. The drift velocity v is indeed proportional to the electric field E and to the mobility μ:

$$v = \mu E \tag{3.6}$$

Being the mobility

$$\mu = \frac{e\tau}{m} \tag{3.7}$$

where e is the electric charge, τ is the mean free time between collisions and m is the effective mass. The mobility of the electrons is greater than the one of the holes. Outside the depletion layer, the charge movement is given by diffusion. The space that a carrier is able to travel before recombination is called diffusion length.

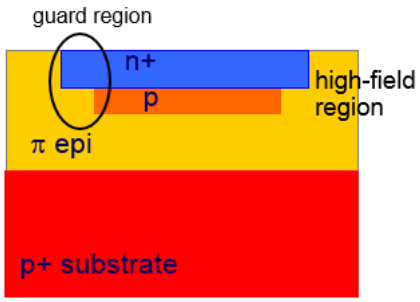

Figure 3.2: Cross section of a typical SiPM cell.

In this framework the SPAD concept can be introduced. This is based on a p-n junction polarized in the inverse region, i.e. operating in Geiger mode. The p-n junction is designed in order to maximize the performance parameters for the desired application like efficiency and response time. In Figure 3.2 an example of a SiPM cell layout is shown. On a silicon substrate usually 300 μm thick covered by an epitaxial layer, an $n^+ - p$ junction is formed by ion implantation. Obviously this is an example since also $p^+ - n$ SPAD devices exists. Together with the high field region, it is highlighted a "virtual" guard region that consists of a ring around the sensitive area, having an intermediate dopant dose. The purpose is to avoid a steep dopant gradient, which is correlated to a higher electric field and would cause an anticipated breakdown at the edges of the junction, involving only the borders and thus wasting most of the sensitive area of the SPAD. Besides, the guard ring works as an electric isolation between adjacent cells.

When a photon hits the device it can be absorbed promoting an electron from the valence band to the conduction band, generating an electron-hole pair. This phenomenon (photoelectric effect), can occur only if the photon energy exceeds the band gap energy of the material, namely:

$$E_{ph} = \hbar \cdot \nu = \hbar \cdot \frac{c}{\lambda} > E_g \tag{3.8}$$

where λ is the wavelength of the incident photon and $\hbar$ is the reduced Planck's constant. In case of silicon, the energy gap is $E_g = 1.12$ eV, therefore the photoelectric effect can occur if $\lambda < 1100$ nm. After the creation of the e-h pair, the electron

moves due to the effect of the electric field and if it travels through the high field region (usually more than 10^5 V/m), it speeds up and acquires enough energy to ionize. This process, called impact ionization, generates soon an avalanche ionizing process. Indeed, the electron generated by ionization speeds up and can in turn ionize again, giving rise to the avalanche. The minimum energy that the primary carriers should have to cause this effect, depends on the energy gap. The average number of carriers generated per unit distance path by electrons or holes is called ionization rate and it is higher for electrons rather than for holes. The inverse of the ionization rate is called ionization length and corresponds to the mean free distance that a carrier may travel before ionizing an atom.

Above and below the junction there are two neutral regions. If a photon is absorbed in a neutral region, within a diffusion length from the border of the junction, the carrier can reach the depletion layer by diffusion and then generate impact ionization. Shorter wavelength photons are likely to be absorbed closely to the depletion layer, whereas longer wavelength photons are usually further absorbed. If a photon is absorbed further than a diffusion length from the depletion layer, it is not absorbed at all because it do not reach the depletion layer (see illustration in Figure 3.3).

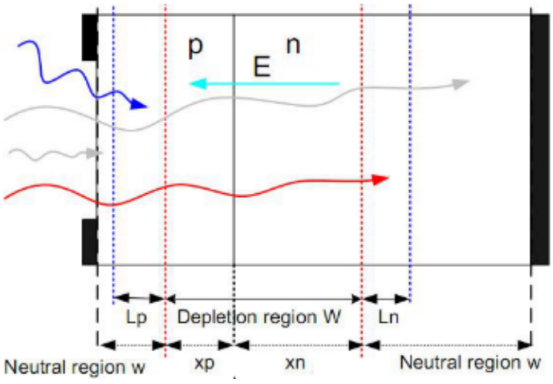

Figure 3.3: Example of photon absorption in a p-n junction. Only blue and red photons are absorbed whereas gray photons are lost

At a certain voltage over the breakdown, the number of carriers generated will grow indefinitely and the impact ionization will initiate an avalanche breakdown, which is a self sustaining current. In a shallow junction, where the breakdown voltage is lower, such a high electric field can be achieved at a lower over-voltage (which is the difference between the supply voltage and the breakdown voltage) since the depletion layer is thinner. From these informations we can give some criteria that should be taken in consideration for an optimum SPAD design:

- Photons should be absorbed in the depletion layer or within the distance of a diffusion length. Since the diffusion is slow, there can be a time jitter in the photon detection response function, so the first option is preferable. This means that it is better to have the neutral zone thinner than the depletion layer (W $\gg$ w in Figure 3.3). Obviously, W has to be longer than or equal to a diffusion length. Moreover, the junction geometry has to be designed carefully, according to the wavelength of incident photons.

- The depletion layer cannot be too thin because a higher equivalent capacitance, and consequently a slower time response, would follow.

- The depletion layer cannot be not even too large in order to avoid transit-

time effects and in order to have a lower breakdown voltage and thus a lower over-voltage required to get a high electric field

- As we have seen above, the ionization rate is greater for electrons than for holes. Besides, the highest is the electric field, the highest is the velocity of the carriers and faster is the time response of the avalanche. In a p-n junction, electrons move from the p-zone to the n- zone, so if one wants them to initiate the avalanche while getting closer to the junction border, it is necessary that photons are absorbed in the p-zone. As for the first point, the geometry has to be designed properly and this means from formulas (3.2) and (3.5), that the concentration of the dopant has to be chosen properly.

- For short wavelengths the junction should be closer to the surface, but not too much in order to avoid problems related to defects on the surface of the lattice.

- The intensity of the electric field has to be high enough in order to obtain an avalanche breakdown. This is given both by the dopant doses and by the over-voltage value.

Finally, it is important to consider the sensitive area of the SPAD: since part of the SiPM surface is occupied by optically passive elements and since some space is needed between cells, a fraction of the total SiPM area is "dead". In order to maximize the photodetection efficiency, it is then important to optimize the SPAD sensitive area. A larger area corresponds to a high photo-detection efficiency.

3.1.1 SIPM equivalent circuit

The SPAD cells in a SiPM are connected in parallel, each SPAD is in series with a quenching resistor. The electrical circuit model [26] is illustrated in Figure 3.4. C_s and C_q are the parasitic capacitance in parallel to the SPAD and R_q is the quenching resistor. The SPAD is equivalent to a switch in series with a voltage source equal to the breakdown voltage and a resistor R_s. Typically, $R_q \approx 500k\Omega$, $C_s \approx C_q \approx fF$ and $R_s \ll R_q$. The SiPM and each of its cells are polarized to a voltage above the breakdown value, $V_b + V_e$ (V_e is the over-voltage).

Basically, the circuit works as follows. When a photon converts, a current is created across the device due to the photoelectric effect and the subsequent avalanche effect. The switch closes and C_s starts discharging through R_s. This first phase has a time constant equal to $R_s\,(C_s + C_q)$. Afterwards, the voltage across the SPAD decreases until when it achieves a value close to the breakdown voltage. During this phase also the current decreases and asintotically reaches the latch-off, a low level of carriers flow so that due to statistical fluctuations the current stops (the switch opens). Then C_q recharges through R_q with a time constant equal to $R_q\,(C_q + C_s)$, slower than the first one. Actually, the recharge of C_q occurs even during the first phase, but the time constant is negligible with respect to the discharge constant. Thus the discharge process is dominant and the current can reach the latch-off level.

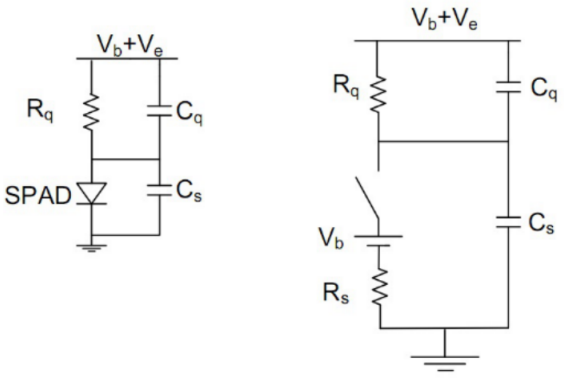

Figure 3.4: Schematic equivalent circuit of a SiPM cell

In this way, the avalanche can stop when the voltage drops to V_b and does not sustain itself indefinitely.

Ideally the current pulse produced by an avalanche has a rise time equal to zero, but practically the parasitic elements of the read out chain act as a low pass filter, giving a rise time of the order of few nanoseconds.The decay time of the current pulse, is given by the total capacitance, and can vary from some tens to several hundreds of nanoseconds. During the recharge the single cell is almost blind to photons while other cells are active.

3.2 SiPM performance parameters

The main parameters to measure the performance of a SiPM are the gain and the photon detection efficiency (PDE). The former is defined as the number of charges produced during a single avalanche, namely

$$G = \frac{Q}{q} = \frac{\int I\,dt}{q} = \frac{V_e \cdot (C_s + C_q)}{q} \tag{3.9}$$

where R is the total output resistance of the readout chain and Q is the total charge stored in C_s and C_q capacitors. It is noteworthy that G depends on the over-voltage V_e.

The photon detection efficiency (PDE) is the ratio between the number of detected photons and the incident photons. It depends on three factors: the geometry fill factor A_f, the quantum efficiency Q_e and the avalanche initiation probability P_t according to the following equation:

$$PDE = Q_e \cdot A_f \cdot P_t \tag{3.10}$$

The fill factor is the ratio between the sensitive area of the SiPM and the total area. The quantum efficiency is defined as the probability that a photon both impinge on the SiPM and generate an e-h pair. It is a strong function of the photon wavelength and is related to the optical absorption coefficient of the semiconductor substrate.

The avalanche initiation probability (P_t) is related to the probability of generating an avalanche. Some avalanches may indeed begin to form but fail to reach a critical number of electron-hole pairs required to form a full discharge. P_t increases with the bias (electric field).

The SiPM has an inherently nonlinear response to pulses of light that are sufficiently intense such that the probability that a single photon hits a cell is no longer small. Suppose a flash of light whose time duration is short with respect of to the recovery time of a cell, uniformly illuminates the SiPM surface. If the probability of firing a cell is 20%, there is 4% probability that two photons will arrive in the same cell within its resolving time. Then the probability for the cell to be triggered will be higher, but the output signal will have the same amplitude. The SiPM output pulse will fall short of the amplitude that would be produced if each photons had triggered two different cells. the fractional loss will increase with the intensity of the light flash, so a measurement of SiPM pulse amplitude vs. light intensity will show increasing departure from proportionality as the light intensity becomes larger. Such nonlinearity in the SiPM response is given by the expression

$$N_t = N_c(1 - e^{-\frac{N_i PDE}{N_c}}) \tag{3.11}$$

where N_t is the number of triggered cells so the detected photons, N_c is the total number of cells (that is the maximum number of detectable photons) and N_i is the total number of impinging photons. The expression (3.11) derives from the Poisson statistics of the photons reaching the surface of the device at the same time.

3.3 SiPM noise

One of the main challenges in the design of SiPM light detectors is the reduction of noise contributions. Geiger-mode ADP cells can indeed trigger avalanches due to both single photoelectrons as well as thermally generated e-h pairs. These electrons lead to spurious "dark" events that add random noise to the signal. The dark rate observed by a SiPM can be as large as 10^6 Hz per mm^2 at room temperature. Usually each of these events corresponds to the firing of a single cell. Thus if one is interested in single electron pulse, the spontaneous dark rate is quite annoying. Nevertheless, the dark rate decreases quickly by many orders of magnitude if a discrimination threshold is set to the simultaneous firing of multiple cell. In the case of scintillation readout where large number of photons are registered per pulse it is possible to fix a discrimination level.

Another source of dark counts is given by the tunneling effect, a phenomenon that occurs when there is a very high electric field that allows the promotion of an electron from the valence to the conduction band, creating an electron-hole pair. This source of noise is relevant at low temperature.

In addition to thermal events, the dark noise of SiPM includes afterpulsing and optical cross-talk. **Afterpulsing** is the presence of secondary charge pulses, correlated to regular pulses. This effect occurs when impurities in the silicon lattice act as traps that de-excite exponentially in time. The electrons from de-excitation

may cause subsequent avalanches within the same cell, typically when C_q is not fully recharged yet. As a consequence they appear as smaller pulses which arise on the charged tail of main pulses. A low value of the depletion layer capacitance, when possible, could decrease the trapping probability, decreasing the gain. Besides, counter measures can be applied to reduce the contamination and damage of the device during fabrication processes.

Optical cross-talk is the generation of extra pulses contemporary to the main pulse. It originates from the recombination light generated in a cell which propagates in the neighbouring cells. As the fill factor is increased, these avalanche photons are more likely to initiate avalanches. One possible solution to this noise mechanism consists in the fabrication of opaque trenches between pixels. When reflective surface is coupled with the SiPM, avalanche photons may reflect inside the scintillator and overcome any inter-cell barrier.

In summary, the noise of a SiPM is a complex interplay of scintillation, thermal, afterpulse, and optical cross-talk events, altering the time response and affecting the energy resolution. Dark counts prevent the choice of a too low threshold. In the same way, after-pulses appears as a long tail over the signal decay.

3.4 Dependance on Temperature

A noteworthy characteristic of many properties of SiPM is the dependence on temperature. For example the breakdown voltage (and consequently the over-voltage) increase of 0.8 V for 10° C of temperature positive variation, while the quenching resistance value decreases. Dark count increases with temperature, therefore cooling the device reduces it significantly but, at very low temperature, increases the probability of afterpulsing. For each application it is necessary to identify the proper **temperature suitable** to reach the best signal to noise ratio.

3.5 Silicon Photomultiplier tested

The SiPMs tested in this work are a $3 \times 3\text{mm}^2$ RGB type produced by AdvanSiD company [27]. RGB SiPMs are based on the n on p silicon technology for the detection of visible light (Red, Green, Blue) [28]. The main feature of this device are listed in Table 3.1.

Table 3.1: The main characteristics of the RGB SiPM tested.

Features
Low dark count rate (< 60 kHz/mm^2)
50 μm micro-cells with 60% fill factor
30% PDE at the peak wavelength, 2.5 V over-voltage
Gain temperature stability <1%/°C
Extremely low single photon time jitter (< 50 ps rms at 2.5 V)

The sensor is hosted to a specifically designed socket that provides pin outputs for SiPM anode and cathode terminals. The socket in turn, is mounted on an Evaluation Board whose function is to provide bias and signal amplification. The board allows for an easy interface to acquisition systems for optical and electrical device evaluation and testing and has been specifically designed to match and optimize the performances of AdvanSiD SiPMs. The amplifier is a high-gain inverting transimpedance device (Z = 1000 Ω) followed by two independent output stages. OUT 1 provides a buffered output with a total transimpedance gain G1 = 500 Ω when terminated on a 50 Ω load. OUT 2 provides a further non-inverting amplification stage with a gain of 5 that gives a total transimpedance gain G2 = 2500 Ω when terminated on a 50 Ω load. A picture of the socket with the SiPM, mounted on the Evaluation baord is illustrated in Figure 3.5. The amplifier scheme is reported in Figure 3.6.

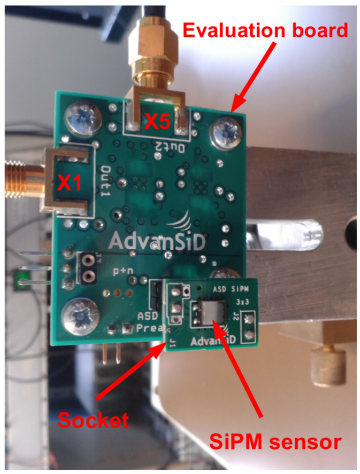

Figure 3.5: The SiPM mounted on the socket connected to the evaluation board amplifier.

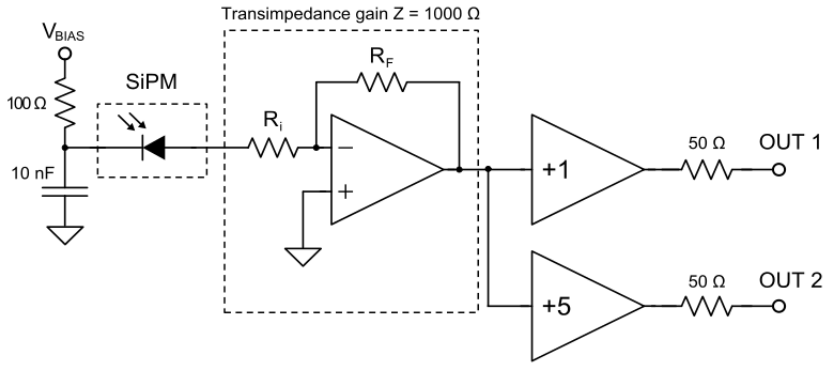

Figure 3.6: The Evaluation Board amplifier sheme.

The gain of the SiPM as a function of the over-voltage, the PDE as a function of the over-voltage and the PDE as a function of the wavelength are reported in Figure 3.7. For the measurements described in chapter 6 the SiPM has been operated at 2.5 V over-voltage in order to obtain a gain ($2{\cdot}10^6$) comparable to the one of the

R1450 Hamamatsu PM tube operated at a voltage of 1500 V.

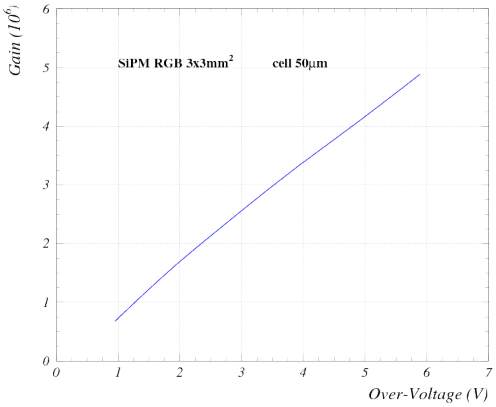

(a) The gain as a fuction of the over-voltage.

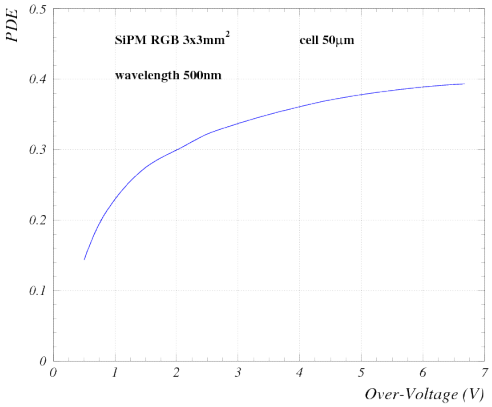

(b) The PDE as a funtion of the over-voltage.

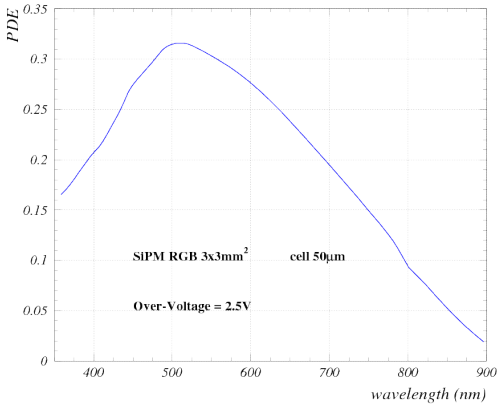

(c) The PDE as a function of wavelength.

Figure 3.7: Characteristics curve of SiPM tested.

Chapter 4

Experimental Setup

During this work, several experiments have been performed at the Legnaro National Laboratories (LNL) in order to study the n/γ pulse shape discrimination properties of new organic scintillating materials coupled with PM tubes and SiPMs. We divide the discussion in two parts. In the first part siloxane scintillators developed at LNL [29] in collaboration with the Padua University, have been coupled with photomultiplier tubes [24] and exposed to a neutron beam.

In the second part, the attention was focused on the light readout through SiPM, whose coupling with scintillators for neutron detection was never studied at least concerning the pulse shape discrimination.

In this chapter the sources, the scintillators, the measurement conditions and the acquisition system exploited are described.

4.1 Radiation Sources

Gamma-ray, α and neutron sources were employed in the experiments to calibrate the detectors, to obtain constant radiation fluxes.

The γ-ray sources used are ^{60}Co, ^{137}Cs and ^{22}Na. The first one is a synthetic radioactive isotope of Cobalt with an half life of 5.2714 years. It is artificially produced by neutron activation of the stable isotope ^{59}Co and then β-decays to the stable isotope ^{60}Ni. As shown in Figure 4.1, the excited nickel nucleus emits two γ rays with energies of 1173 keV and of 1333 keV, hence the overall nuclear reaction is

$$^{60}_{27}\mathrm{Co} \rightarrow ^{60}_{28}\mathrm{Ni} + \mathrm{e}^- + \overline{\nu_e} + \gamma\,\mathrm{rays} \tag{4.1}$$

^{137}Cs has an half life of 30.17 years and is one of the most common fission products of the ^{235}U nuclear fission. About 95 % decays by beta emission to a metastable nuclear isomer of barium ($^{137\mathrm{m}}$Ba), whereas the remainder directly populates the ground state of Barium-137. The metastable isomer of barium emits photons with an energy of 662 keV. The scheme of the decay is shown in Figure 4.2.

^{22}Na, a radioactive isotope of Sodium, has an half life of 2.6027 years. It decays by β^+ decay to the first excited state of Neon-22. When ^{22}Ne de-excites, it emits a

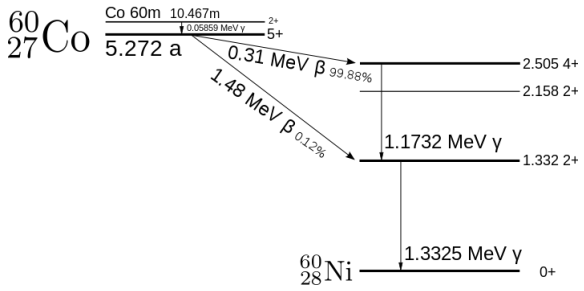

Figure 4.1: ^{60}Co decay scheme.

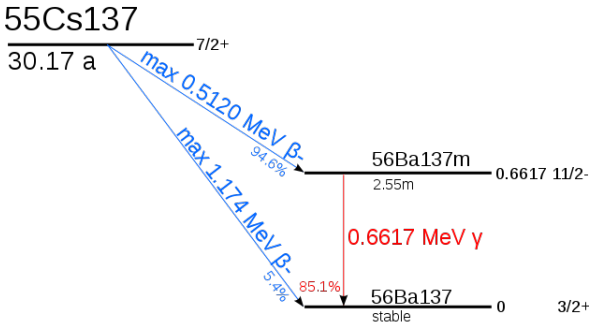

Figure 4.2: ^{137}Cs decay scheme.

γ-ray of energy of 1274 keV. The positron radiated after the decay, captures soon an electron and annihilates. When this phenomenon occurs, two γ-rays with energy of 511 keV each, are produced. Since the total momentum before this occurrence is null, the total momentum afterwards must be zero. For this reason the two γ-rays are emitted back to back. Figure 4.3 shows the decay scheme of ^{22}Na.

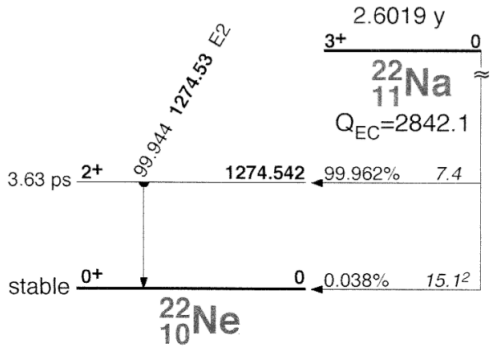

Figure 4.3: ^{22}Na decay scheme.

During the tests of the scintillators a^{241}Am α source was also employed. ^{241}Am is the most prevalent isotope in nuclear waste and has an half-life 432.6 years. Together with α particles of $\sim$ 5.4 MeV kinetic energy, low energy photons (59.6 keV) are emitted. For this reason ^{241}Am is also useful to calibrate detectors at low energy. The main characteristic of the sources used are summarized in Table 4.1.

Table 4.1: Main characteristics of the sources used during the experimental part of this work..

Source	Half-life [yr]	γ energy [keV]	α energy [MeV]
^{241}Am	432.6	59.6	~ 5.4
^{137}Cs	30.17	662	
^{22}Na	2.6027	511 1275	
^{60}Co	5.2714	1173 1333	

An Am-Be neutron source (see 1.1) was also employed to obtain fast neutrons for the laboratory measurements, the emitted neutron energy spectrum is illustrated in Figure 4.4.

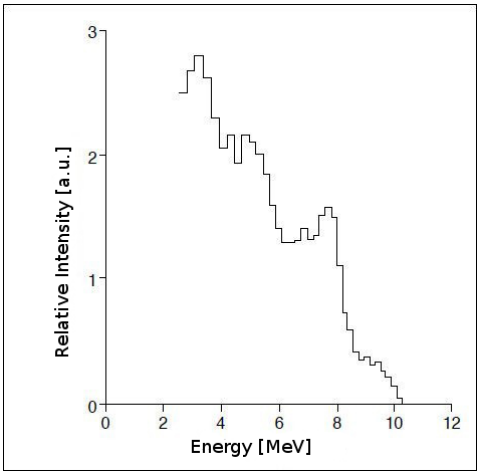

Figure 4.4: The AmBe neutron energy spectrum.

Neutron fluxes have also been produced using the ^{7}Li(p,n)^{7}Be reaction at the CN accelerator at LNL. For the details of the experimental setup see section 4.3.

4.2 Organic scintillators

Both liquid and solid siloxane organic scintillators have been tested.

Those materials are rubbery and flexible due to the low rotational energy of the Si-O bond. They show good radiation hardness properties and a wide range of temperature stability (between -100°C and 200°C). Besides, they are easy to handle and they are unlikely to crack guaranteeing a good mechanical stability. They can be produced in a wide variety of volumes and shapes, so they are usually synthesized to match the PM tube's geometrical dimensions.

The luminiscence takes place due to the energetic structure of the benzene ring (see Figure 4.5) present in the chemical structure of the compounds. Its emission is centred at about 300 nm while common PM tubes are scarcely sensitive in this region of the electromagnetic spectrum. Therefore it is necessary to introduce primary or also secondary fluorophores that act as wavelength shifters. To enhance the light yield, our detectors were doped with different concentrations (between 1% and 4%) of 2,5-Diphenyloxazole (PPO) which has the chemical structure shown in Figure 4.6 and constitutes the primary fluorophore. This material absorbs at about 300 nm and emits at 340 - 370 nm band. Lumogen Violet (LV) was also added in low concentrations (0.02%) as secondary fluorophore. This material is derived from the molecule shown in Figure 4.7. It absorbs between 370 nm and 390 nm and re-emits at 450 nm. Given the good matching between their absorption and emission spectra, these two fluorophores are often combined. Recent detailed studies varying the concentration of the primary and secondary fluorophores are reported in [30].

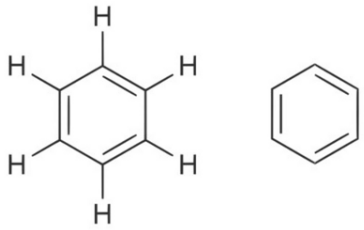

Figure 4.5: The benzene ring.

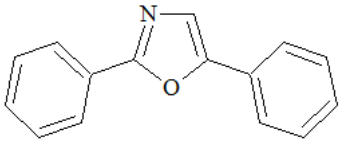

Figure 4.6: PPO chemical structure.

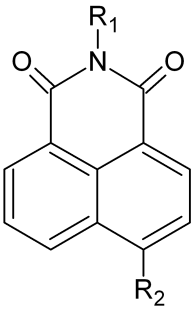

Figure 4.7: The 1,8-Naphthalimidi molecule from which the Lumogen Violet is derived.

The prototypal liquid oligosiloxane scintillators tested in this work are TPTMTS (tetraphenyl-tretramethyl-trisiloxane) and PPTMTS (pentaphenyl-tremethyl-trisiloxane) that present the chemical structure illustrated in Figure 4.8. The liquids were contained in small cylindrical Suprasil® quartz cuvettes (Figure 4.9), 2 cm in diametermatching the window geometry of the Hamamatsu R1450 PM tubes [24]. The cuvette was wrapped with white Teflon in order to optimize scintillation light diffusion inside the scintillating material. This technique exploits the excellent properties of Teflon as diffuser in an extended wavelength range. This allows to improve

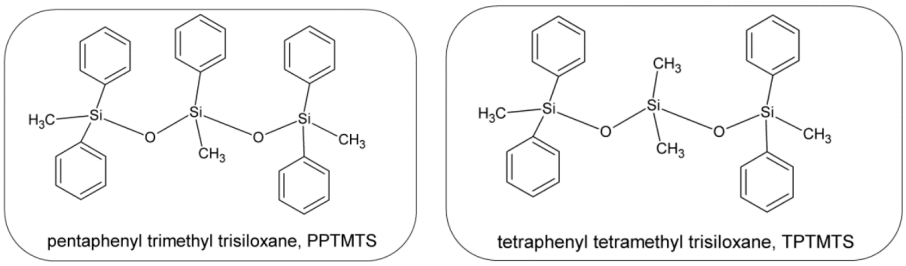

(a) PPTMTS (b) TPTMTS

Figure 4.8: Chemical structure of the oligosiloxane liquid scintillators tested in this thesis.

Figure 4.9: The cuvette containing the liquid scintillators tested.

the uniformity in response of the sample as a function of the scintillation event position.

A solid polysiloxane scintillator (22% Phenyl), 5 inch in diameter was also studied. The chemical structure of this polysiloxane material is illustrated in Figure 4.10. The scintillator is doped with 1% of PPO and with of 0.02% of LV. Figure

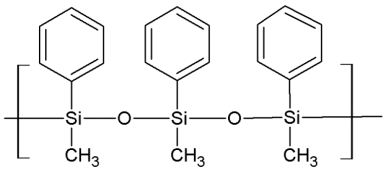

Figure 4.10: The chemical structure of a standard polysiloxane material.

4.11(a) shows it coupled with a 5 inch PM tube from the Hamamatsu company.

In Table 4.2 are summarized the concentrations of the wavelength shifters added to the original compound of the scintillator considered.

The commercial EJ309 liquid scintillator described in section 2.3 has been used as a standard reference.

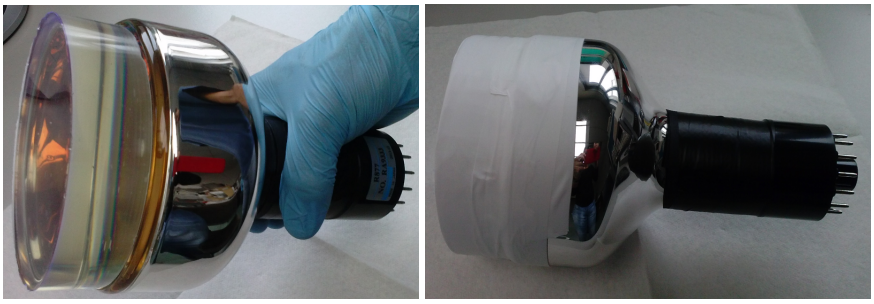

(a) (b)

Figure 4.11: The solid polysiloxane scintillator tested, coupled with the PM tube.

Table 4.2: Complete list of the tested samples.

Name	%PPO	%LV
TPTMTS1	1%	0.02%
TPTMTS2	2%	0.02%
TPTMTS4	4%	0.02%
PPTMTS1	1%	0.02%
STD5"	1%	0.02%

4.3 Experimental setup at the Van der Graaff CN accelerator

In order to produce a neutron flux of known energy, the reaction $^{7}\mathrm{Li}(\mathrm{p},\mathrm{n})^{7}\mathrm{Be}$ was used. To do this, a 4 MeV proton beam provided by the Van der Graaff CN accelerator of the Legnaro National Laboratories impinged agains a thick LiF target. The beam was pulsed at 3 MHz with $\sim$2 ns width bunches so a pulsed neutron flux was obtained. The energy of the emitted neutrons as a function of the emission angle is shown in Figure 4.12. The energy is maximum (2.32 MeV) when the neutron is emitted in the forward direction. During the tests described in the following, the detectors were placed at a distance of about 60 cm from the target in the $\theta < 15°$ angular range so that the average neutron energy is about 2.3 MeV. In order to obtain timing information from the beam bunches, an inductive pickup was placed along the beam line. Those beam bunches induce a bipolar current signal in the pickup which allows to define the time reference for the neutron TOF measurement. A schematic view of the experimental apparatus is given in Figure 4.13.

4.4 Experimental Setup for the Laboratory Measurements

The second series of measurements has been performed in laboratory. In particular, a light-shielded scattering chamber has been exploited for the SiPM tests and the comparison between the SiPM's light readout and the PM tube's light readout

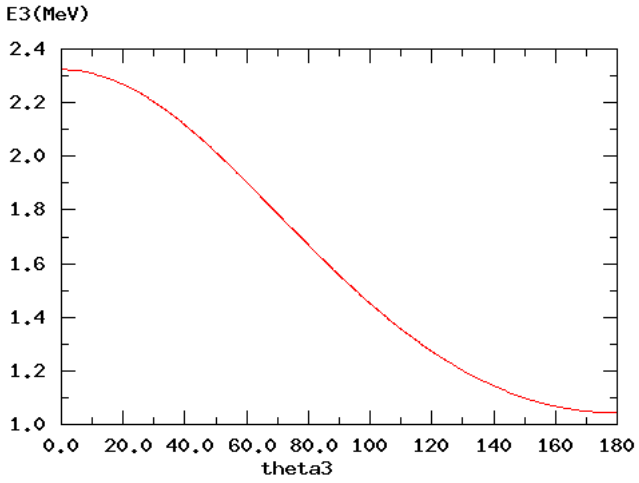

Figure 4.12: Energy distribution as a function of the emission angle for the reaction $^{7}\mathrm{Li}(\mathrm{p},\mathrm{n})^{7}\mathrm{Be}$ when the incident proton energy is of 4 MeV.

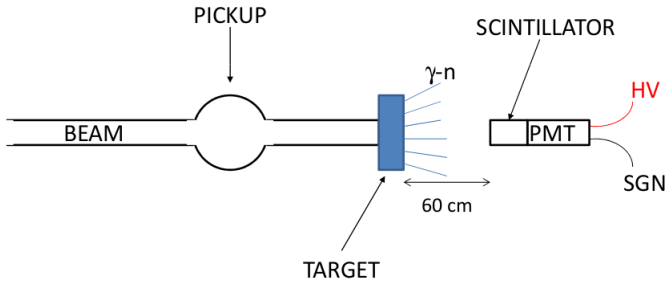

Figure 4.13: Sketch of the experimental setup used at the CN accelerator.

using α,γ-rays and neutron sources. In general, the amount of scintillation light reaching the sensor depends on the position of the scintillation event inside the sample and on the light diffusion and transport properties. In order to minimize the fluctuations of the scintillation signal, the liquid samples were confined in small volumes (about 70 mm^3) in Teflon cylinders with internal diameter smaller than the sensor's diameter (about 3 mm). Special care was taken for sealing such cylinder to avoid the formation of air bubbles. The alignment between SiPM and the Teflon cylinder is also very delicate. In Figure 4.14, a picture of the apparatus shows the experimental condition during a test with the α source where EJ309 and TPTMTS4 samples have been tested. The same samples were also read out using PM tubes with a similar gain. In this case the PM tube window was covered in order to limit its sensitive area to the same sensitive area of the SiPMs.

The same experimental setup was used for the neutron source measurements. As shown in Figure 4.15, the γ-rays radiation background induced by the Am-Be source has been attenuated using Lead and Copper blocks. A pulsed laser (70 ps

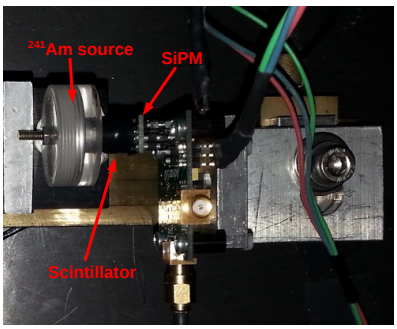

Figure 4.14: The laboratory setup consisting of an α source, the scintillator and the SiPM.

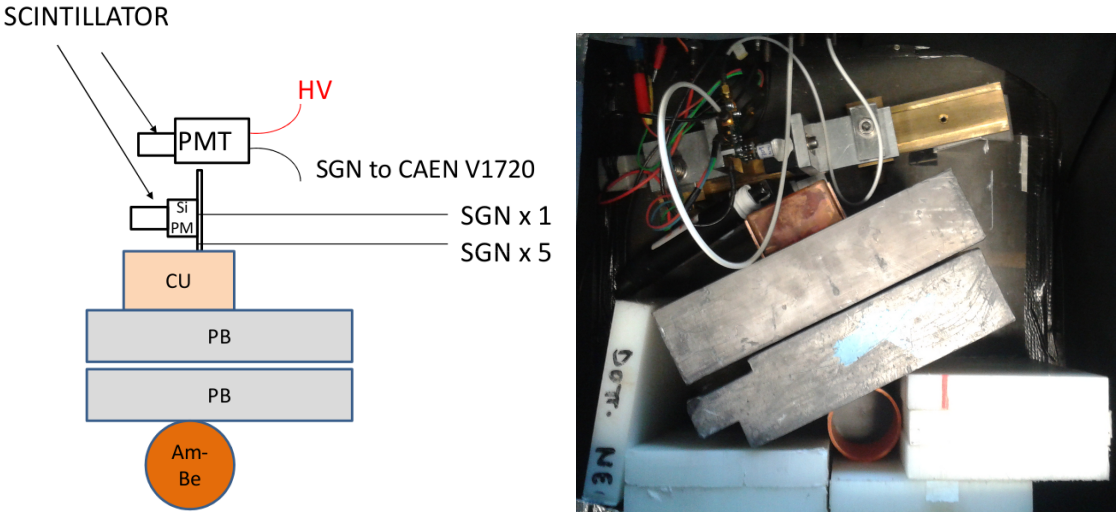

(a) Scheme (b) Picture

Figure 4.15: The experimental setup during the acquisition of the Am-Be neutron source. The lead and copper blocks are used to attenuate the γ-rays radiation background.

rms pulses width) emitting at 395 nm was also exploited for calibration purposes and for studying the electrical impulse response of the PM tubes and SiPM devices.

4.5 Acquisition System

All the measurements reported in this thesis work have been performed using a digital acquisition system whose core is the 250 MS/s, 12 bit CAEN V1720 digitizer (Figure 4.16). A detailed technical description is given in the digitizer's data sheet [31]. The custom software that manages the data acquisition is based on the Linux version of CAEN drivers and libraries. The digitizer have a circular buffer memory on which the data are stored. If the trigger threshold is overstepped the computer buffer memory (RAM) is filled with the pre/post samples whose number is programmable. In our case pre-trigger was set to 20% before the trigger, whereas

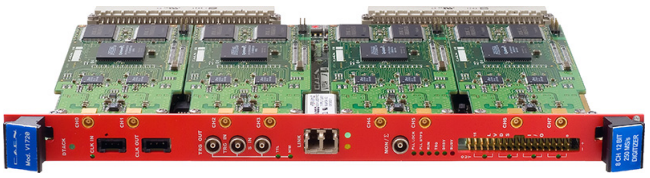

Figure 4.16: The CAEN acquisition board.

the post trigger was set at 80%. The total width of the acquisition window was 752 samples corresponding to 3 μs. In this way the window includes the interesting part the the shapes. When the buffer is full (230 MB) the shapes are written on disk in compact format. The data acquisition system is schematically represented in Figure 4.17.

The most relevant difference between "digital" and "analogue acquisition mode" consists in the possibility of recording any single waveform after minimal analogue processing. On the contrary in "analogue mode " the signal is heavily shaped and processes with often irreversible loss of information before recording. For instance in our case, we could optimize the signal shaping (high pass, low pass, pole zero filters) a posteriori (off-line).

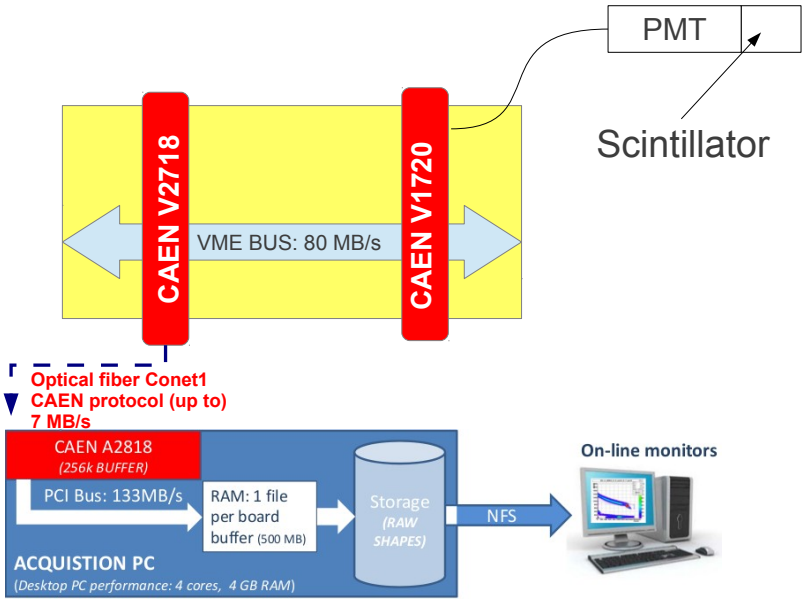

Figure 4.17: Scheme of the acquisition system.

Chapter 5

Pulse Shape Discrimination

The digital data acquired during the experiments illustrated in the previous chapter have been off-line analized to extract several quantities. The first one is the typical shape of the PMT and SiPM signals for the scintillating materials as a function of the incoming radiation type. Then, concentrating on a shpe-by-shape analysis, the neutron-γ discrimination capabilities of the detectors have been tested. The experimental results will be described in the next chapter, now we describe the common algorithms applyed to the shapes during the analysis and the most common pulse shape discrimination methods reported in literature. The newly developed **photon couning** algorithm used to fully expolit the SiPM capabilites is also illustrated.

5.1 Preliminary pulse shape processing

Several quantities have to be extracted from the sampled shapes during the data analysis: the energy release of the impinging radiation, its time of arrival in the detector and various pulse shape discrimination parameters. As a first step, the signal baseline is computed as the average amplitude of the first ten samples. This value is immediately subtracted from each waveform so that its baseline becomes zero. Other important quantities are the maximum amplitude of the signal (**rawmax**) and the shape integral (**energy**). Timing information from the shape are extracted through an algorithm acting as a digital emulator of a Constant Fraction Discriminator filter. Given a certain threshold (usually computed as a percentage of the signal maximum), and a starting sample (usually the number of sample at which the maximum signal amplitude occurs), the threshold-crossing time is evaluated analytically applying a cubic interpolation filter. RC-CR algorithms have also been employed to obtain low-pass or high-pass digitally emulated filters (see A).

5.2 Zero Crossing method

The Zero Crossing technique (ZCO) is widely used and is considered one of the best ways to discriminate neutron from γ-ray pulses using liquid scintillators like BC501 [14, 16, 32].

In the analogue version of the filter, the original pulse is integrated and subsequently differentiated so that the signal becomes bipolar. The baseline crossing of this bipolar signal happens at different times according to the slope of the tail of the original waveform. Therefore the measure of the zero crossing time gives the discrimination parameter (ZCO). Moreover, the zero crossing point for γ-rays is fixed and energy-independent, while the zero crossing point for neutrons changes as a function of their energy: the lower is the energy, the closer is the zero crossing time between the two particle sets.

In the digital case (see [16]) the integration and differentiation of the pulse can be obtained using RC-CR emulating algorithms (see appendix A) and results are similar to the analog ones. A valid alternative to this procedure, available ony in the digital domain, consists in extracting the ZCO-equivalent information from the difference between a suitable start time and the time where the signal crosses a pre-defined fraction of the maximum peak amplitude. This process is illustrated in Figure 5.1 where the relation between the discrimination parameter and the physical properties of the waveforms can be clearly observed. Timing information is

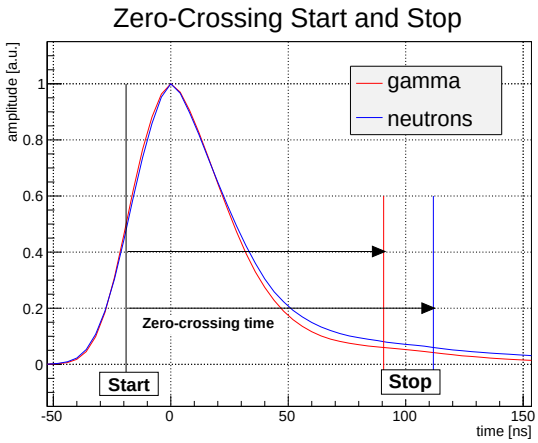

Figure 5.1: Definition of ZCO start and stop. The threshold for the stop is fixed at 6% of the peak amplitude.

extracted using the digital constant fraction discriminator algorithm: the start time is usually computed at one half of the maximum peak amplitude in the rising edge of the signal while the stop is chosen in the decreasing front so that the discrimination between pulses coming from different particles is maximized. Typical values are at about 10% of the maximum peak amplitude. An example of ZCO distribution for NE213 liquid scintillator at different energy thresholds is reported in Figure 5.2.

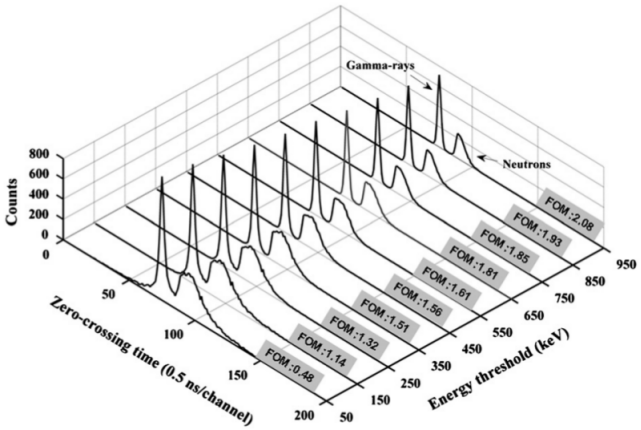

Figure 5.2: ZCO distributions at different energy thresholds for NE213 organic scintillators. Adapted from [16].

5.3 Pulse Gradient Analysis

The Pulse Gradient Analysis method (PGA) is based on the comparison of the maximum peak amplitude and the amplitude of a sample occurring a defined time interval after this maximum, known as the **discrimination amplitude**. The time interval used for the selection of the discrimination amplitude depends on the scintillator properties and on the type of photomultiplier tube used. A scatter plot of the sample amplitude against the maximum peak amplitude allows to identify the two population. A neutron induced pulse has indeed a higher discrimination amplitude for the same maximum peak amplitude compared to a γ-ray induced one (see Figure 5.3). Usually the PGA method is applied to an RC integrated copy of the

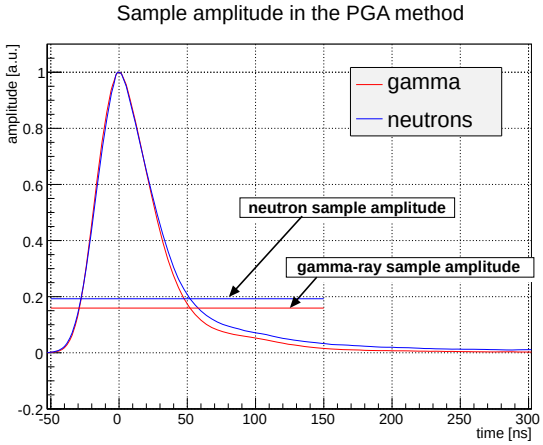

Figure 5.3: Example of the sample amplitude extracted from a neutron pulse and a γ-ray pulse. The sample amplitude is evaluate 52 ns after the pea.

original pulse to minimize high frequency noise effects. This technique is widely

used in literature, for example see D'Mellow in [33] and Gamage in [15]. Their results using an Am-Be neutron source and liquid scintillators (EJ-301 in the former case, BC-501 in the latter) are reported in Figure 5.4.

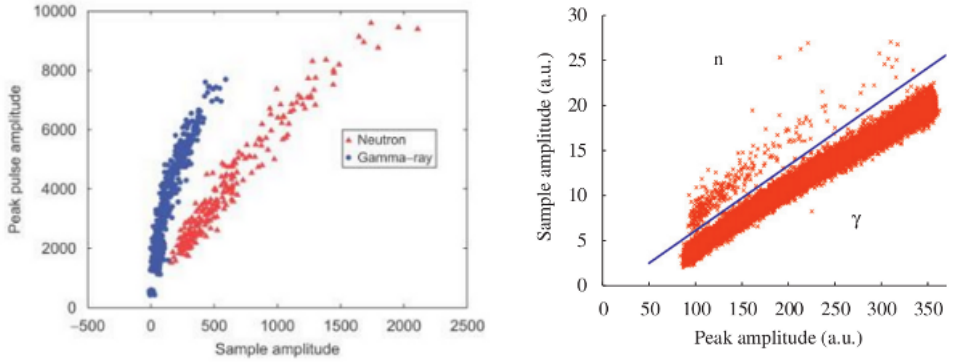

(a) D'Mellow et al. [33] (b) Gamage et al. [15]

Figure 5.4: Sample amplitude against peak amplitude

5.4 Charge Comparison Method

The Charge comparison method (CC) is based on the comparison of the pulse integrals in two different time intervals (long integral and short integral). The former corresponds to the integral of the area of the entire pulse whereas the latter includes only its tail. This procedure is well established in the analogue domain while in the digital version it is implemented summing the amplitude of the discrete samples. Usually the starting point of the long integral is set to coincide with the starting point of the rising pulse. The starting point of the short integral is determined by testing in which values one appreciates better the difference between the neutron short integral and the γ-ray short integral. Typical values are some tens of nanoseconds after the peak amplitude. The end point in both cases is set at the end of the pulse, at about one microsecond after the peak amplitude. The scatter plot of the short integral against the long integral allows to appreciate two different population since the short integral of the neutron pulses is larger compared to the one of a γ-ray having the same long integral. An example of the application of this technique is given by Gamage et al. in [15]. The resulting scatter plots are shown in Figure 5.5.

We considered the fast integral and the slow integral instead of the short integral and the long integral. The slow integral coincides with the short integral whereas the fast integral is the integral of the area of the fast part of the pulse. The starting point is set at the point where the pulse starts rising, the end point is set at the starting point of the slow integral. In Figure 5.6 the two areas are highlighted.

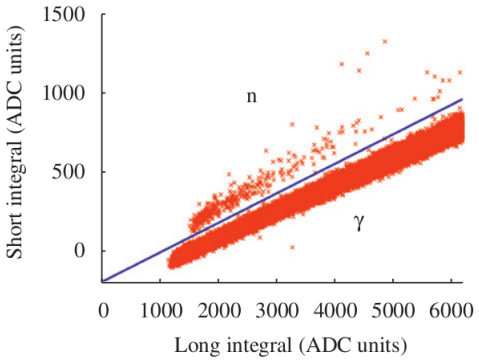

Figure 5.5: Scatter plot of short integral versus long integral for an Am/Be neutron source for the charge comparison method [15].

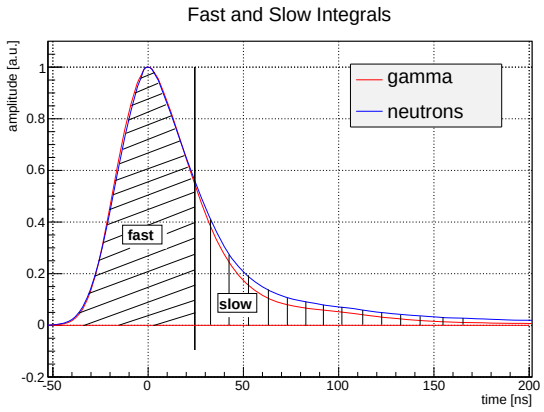

Figure 5.6: The two areas of the fast integral and the slow integral considered for the charge comparison algorithm. The starting point of the slow integral is set at 25 ns after the peak.

5.5 Neutron - γ Model Analysis

This technique consists in the comparison of an unidentified pulse with a neutron pulse and a γ-ray pulse previously identified [15, 17]. The sample pulses are usually obtained by averaging a set of several thousand known γ-ray and neutron pulses. The definition of the two sets is given by the measurement of the time of flight which is different between the two particles. The characterization of the comparison is given by calculating the difference between the chi-square for the γ-ray model (χ^2_γ) and the neutron model (χ^2_n) using the following equations:

$$\chi^2_\gamma = \sum_{i=1}^{n} \frac{\left(\frac{Am_\gamma}{Ap_u} p_u(i) - m_\gamma(i)\right)^2}{m_\gamma(i)} \tag{5.1}$$

$$\chi^2_n = \sum_{i=1}^{n} \frac{\left(\frac{Am_n}{Ap_u} p_u(i) - m_n(i)\right)^2}{m_n(i)} \tag{5.2}$$

$$\Delta\chi^2 = \chi^2_\gamma - \chi^2_n \tag{5.3}$$

where p_u, m_γ and m_n are unknown pulse, model γ-ray pulse and model neutron pulse respectively, Ap_u, Am_γ and Am_n are area of the unknown pulse, model γ-pulse and neutron pulse respectively for i number of samples. Thus, if the chi-square difference $(\chi^2_\gamma - \chi^2_n)$ is negative the unknown pulse is consistent with the γ-ray model, whilst if positive the unknown pulse is consistent with the neutron model. The chi-square difference can be plotted against the pulse area so that two population are delineated. Gamage at al. have implemented this algorithm in [15] and their results are presented in Figure 5.7.

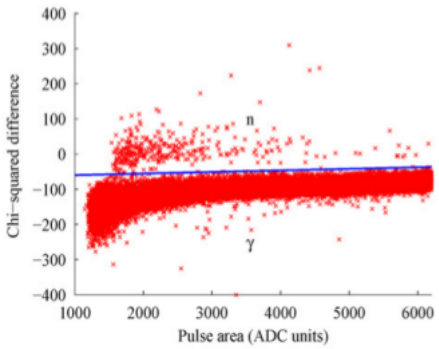

Figure 5.7: Scatter plot of chi-square difference versus pulse area obtained in [15]. An Am-Be source and a BC-501 liquid scintillators were used.

5.6 Simplified Digital Charge Comparison

The simplified digital charge comparison methods (SDCC) [34] relies on the decay rate difference of neutron interaction and γ-ray interaction in organics. In this method the rise time proportion of the pulse is discarded and the peak amplitude is set as the first sample of the signal. A discrimination parameter (D) is introduced, defined to be for each pulse:

$$D = log\left(\sum_{n=a}^{n=b} x_n^2\right) \tag{5.4}$$

where x_n is the sample amplitude of the nth sample and a and b are the samples associated with the start and the end number of the short integral, respectively. Usually, a and b corresponds to the samples at three-sixteenths sample and one half of the pulse, respectively. The discrimination parameter can be represented against the peak amplitude as done by Gamage at al. in [15] (Figure 5.8).

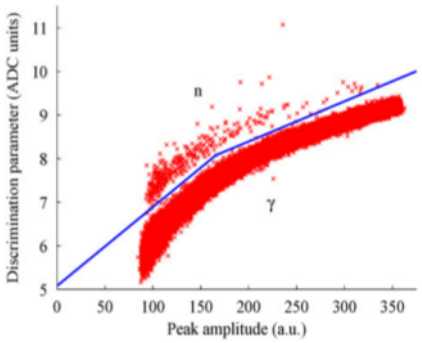

Figure 5.8: The parameter D against the pulse area as resulting from [15].

5.7 Photon counting with SiPMs

This method exploits the SiPM single photon counting capabilities to discriminate between a γ-ray pulse and a neutron pulse. We proceed firstly filtering the signal in order to deconvolve the pulses from the SiPM-amplifier response and to recover the original light pulse shape. To this aim, the following filter is used:

$$S_{filter}[k] = S[k] - e^{-\frac{1}{\tau}} S[k-1] \tag{5.5}$$

where $S_{filter}[k]$ is the k^{th} sample of the filter signal and $S[k]$ is the k^{th} sample of the original signal; τ is the dominant time constant of the SiPM-amplifier configuration and is measured by filtering the average single photoelectron signal falling tail with an exponential function. At this point a counting gate is selected according to the optimum estimate of the slow scintillation time constants. Inside this gate, using the filtered signal, the number of photons is counted. The algorithm to count the photons has been first implemented during this work and consists in the comparison of the k^{th} sample with the previous and the following one. The amplitude difference is calculated. If at least one of the two differences crosses a given threshold, the photon i counted. This method minimizes the effects of pile-up on threshold crossing.

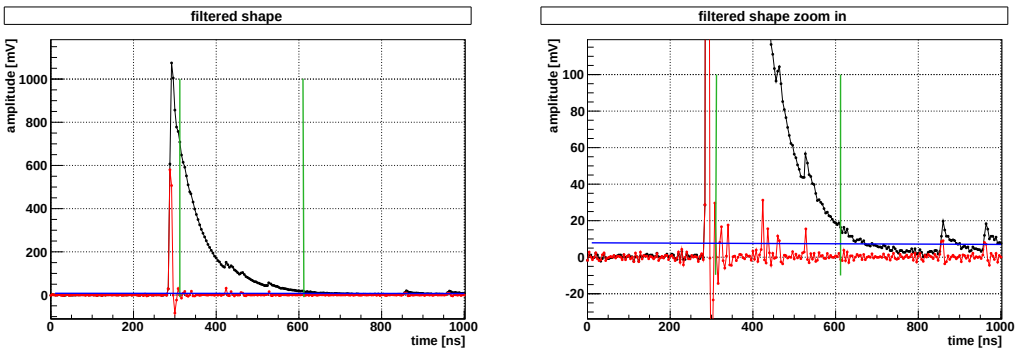

(a) (b)

Figure 5.9: a) Photon counting algorithm: in black, the original shape, in red the filtered shape, in green the gate for the counting and in blue the threshold. b)Zoom of the photon counting gate.

Chapter 6

Data Analysis and Experimental Results

The data analysis and the experimental results obtained both for measurements at the CN accelerator and in the laboratory are now presented. First of all the scintillation decay time constants have been measured exploiting the Bollinger-Thomas method. Afterwards, the detector calibration procedure carried out during CN accelerator measurements is discussed. Then the pulse shape discrimination data analysis is illustrated for PM tube light readout (CN measurements) and SiPM light readout (laboratory measurements). Finally the comparison between PM tube and SiPM light readout is discussed.

The last section of this chapter is dedicated to the summary of the obtained results .

6.1 Decay Time Measurements

Decay time constant measurements were made by the Bollinger-Thomas single photon method [11]. The used setup is illustrated in Figure 6.1.

We measured the difference in time between the excitation of the scintillator and the formation of the first photoelectron in a PM tube that views the scintillator. A ^{137}Cs γ source was used to excite the scintillator sample, producing light pulses in it. The samples were wrapped with Teflon only on the sides, leaving two surfaces opened to the PM tubes. A PM tube ("start") was located close to one of the open surfaces and was directly exposed to the light pulse. The other PM tube ("stop") viewed the other surface from a distance of approximately 20 cm, through neutral filters and collimators.

A large fraction of the light from the scintillator is thus collected by the "start" PM tube, where a zero-time signal is formed with negligible jitter with respect to the true light pulse time. On the contrary, we tuned the filters and collimators so that just single photons from the same pulse can reach the "stop" PM tube.

The timing spectrum of single photons detected by the "stop" PM tube reflects the statistics of the photons emitted during the scintillation light pulse and allow

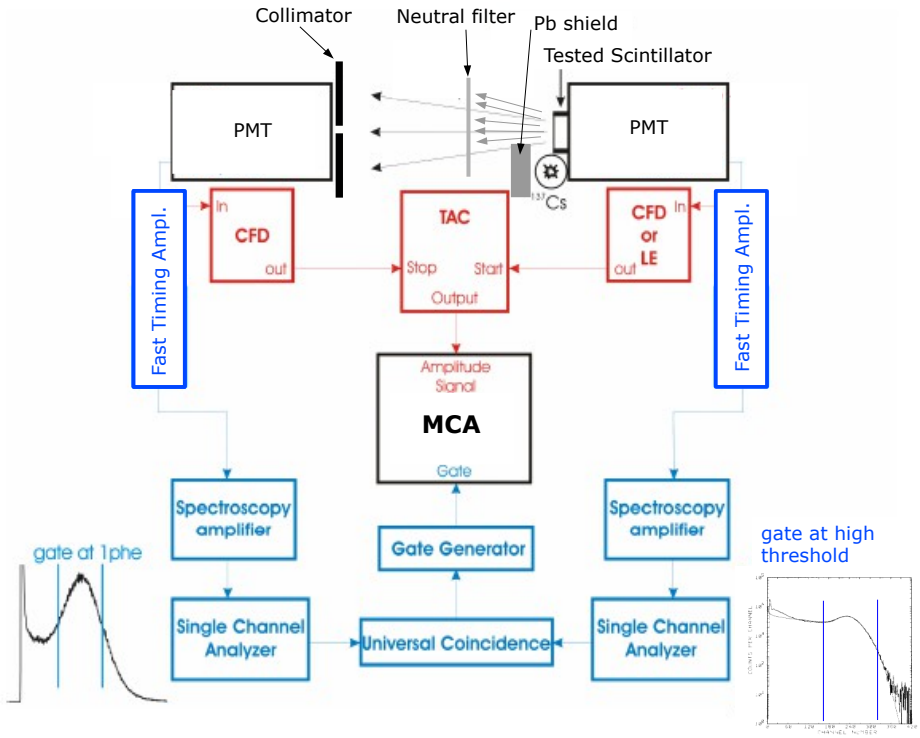

Figure 6.1: The setup used by Bollinger-Thomas

the study of the decay time of the scintillator under test.

The energy windows were set at the single photoelectron peak for the "stop" PM tube and at the Compton edge for the reference PM tube. In order to avoid spurious signals due to Cherenkov events in the window of the "stop" PM tube the source was shielded with lead so that γ-rays could illuminate just the scintillator sample. Such a configuration ensures the detection of single photons from the scintillator, induced by a ^{137}Cs γ source. The decay curves obtained are shown in Figures 6.2, 6.3 and 6.4 both in linear and logarithmic scale. Each curve was interpolated with two, three or four exponentials with constant background. The non linear fit was performed with the Levenberg–Marquardt method. The best χ^2 fit was obtained with four time constants for EJ309 and with three time constants for TPTMTS2 and TPTMTS4.

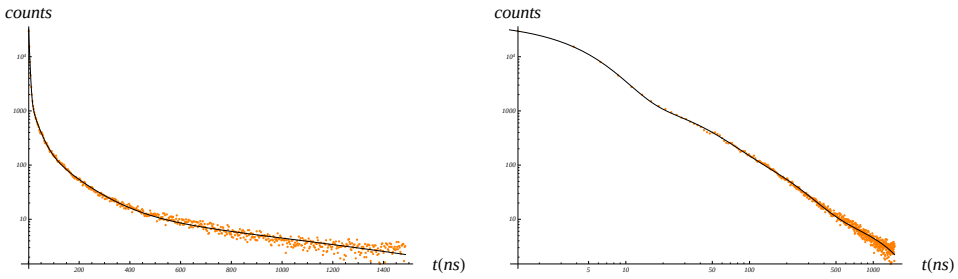

(a) Linear scale (b) Logarithmic scale

Figure 6.2: Decay time curve for EJ309 with the exponential fit superimposed.

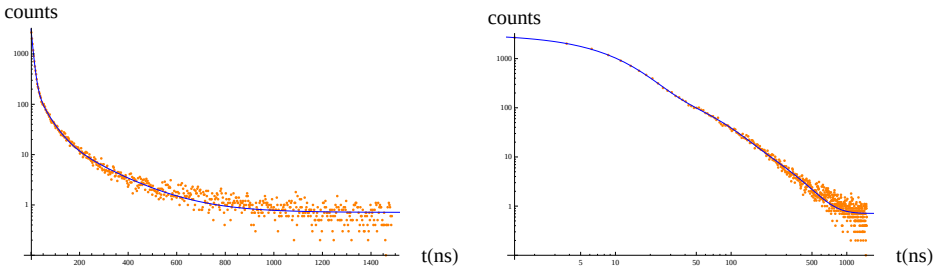

(a) Linear scale (b) Logarithmic scale

Figure 6.3: Decay time curve for TPTMTS2 with the exponential fit superimposed.

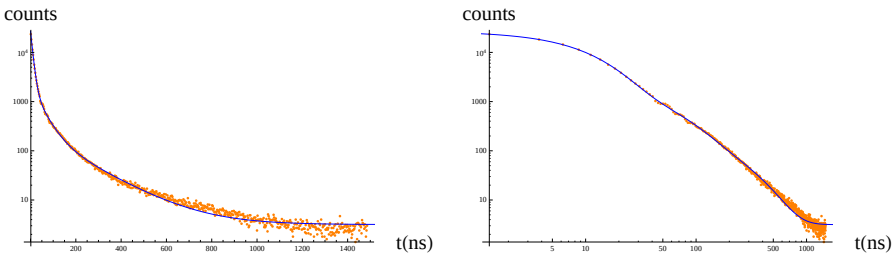

(a) Linear scale (b) Logarithmic scale

Figure 6.4: Decay time curve for TPTMTS4 with the exponential fit superimposed.

The results for EJ309, TPTMTS2 and TPTMTS4 are presented in Tables 6.1(a), 6.1(b) and 6.1(c) respectively. The decay time constants obtained are presented in decreasing order on relative intensity. The main contribution is greater then 90%. It is worth to notice that the time constants obtained for TPTMTS2 and TPTMTS4 are approximately a factor of two larger than the corresponding decay time constants obtained for EJ309.

Table 6.1: Best solutions for detectors tested. The third column indicates the relative intensity of each exponential contribution.

(a) Results for EJ309 given by fit with four exponentials.

Time Constant	Results	Relative Intensity
τ_1	(3.26 ± 0.01) ns	(95%)
τ_2	(19.0 ± 0.5) ns	(4 %)
τ_3	(71 ± 5) ns	(1 %)
τ_4	(313 ± 55) ns	(0.1%)

(b) Results for TPTMTS2 given by fit with three exponentials.

Time Constant	Results	Relative Intensity
τ_1	(7.97 ± 0.04) ns	(91%)
τ_2	(42 ± 1.1) ns	(8.0%)
τ_3	(165 ± 7) ns	(1.0%)

(c) Results for TPTMTS4 given by fit with three exponentials.

Time Constant	Results	Relative Intensity
τ_1	(9.08 ± 0.04) ns	(90.7%)
τ_2	(43.0 ± 0.9) ns	(7.7 %)
τ_3	(166 ± 5) ns	(1.6 %)

6.2 Detector Energy Calibration

For all samples tested at the CN accelerator last January, has been realized an energy calibration test using two of the sources presented in 4.1, ^{60}Co and ^{137}Cs. The aim of the calibration is to have the neutron energies in unit of keV electron equivalent (see chapter 2, section 2.2.2), in order to give an energy threshold of discrimination after the pulse shape analysis.[1]

The γ-radiation emitted by the sources interacts with low-Z materials of which our scintillators are made, through Compton effect. Only part of the incident energy is therefore transferred to electrons of the material and can thus be detected. The resulting energy spectrum will be characterized by an almost constant plateau over which the so-called Compton edge, that constitute the only structure that can give us energy information, stands out. The maximum energy transferred to an electron by the incident γ-ray, occurs when the photon is diffused at 180° and is given by

$$E^e_{max} = \frac{2E^2_\gamma}{m_e c^2 + 2E_\gamma} \tag{6.1}$$

where E_γ is the incident photon energy, m_e is the electron mass and c is the light

[1] A neutron energy of about 2.35 MeV corresponds to approx. 700 keV$_{ee}$ [10].

speed in vacuum. Experimentally has been shown [35] that the Compton edge corresponds to the 95% of the E^e_{max} and so the energies were been calculated accordingly. Table 6.2 summarizes the incident photon energies, the maximum energies calculated through equation (6.1) and the Compton energy for the sources available to calibrate. The calibration procedure adopted, was to make a Gaussian fit of the

Table 6.2: Incident photon energy, E^e_{max} and energy of the Compton edge for the sources available to calibrate.

Source	E_γ[keV]	E^e_{max}[keV]	E_{CE}[keV]
^{22}Na	511	341	324
	1275	1062	1009
^{137}Cs	662	477	454
^{60}Co	1173	963	933
	1333	1118	

Compton edge, taking the mean as the channel to associate at the Compton energy. It is noteworthy that the two energies relative to ^{60}Co are very close so the two Compton edges overlap because our detectors do not have enough resolution to distinguish them. Often the average between the two maximum energies, namely 989 keV is associate to the single peak visible in the spectrum. But this result in a bias, as in this case the energy is systematically greater than in the cases of other sources. As a first approximation remedy we have exploited the Caesium energy spectrum to reproduce a situation in which two Compton edges are very close because they have similar energies. Figure 6.5 shows the result obtained by summing

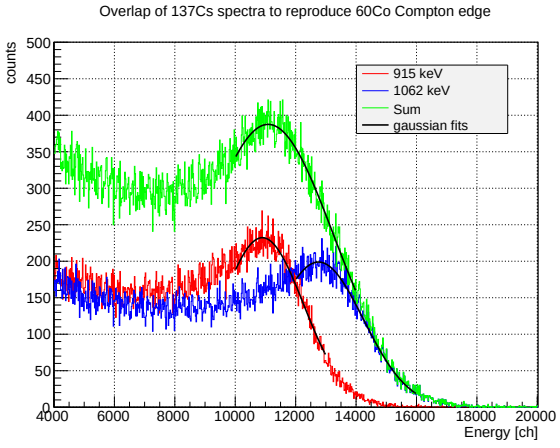

Figure 6.5: Overlapping between two close Compton edges. The sum (green spectrum) has its peak at an energy lower than the average energy. The black curves are gaussian fits over the peaks.

the two scaled spectra: the sum peaks at an energy lower than the average. There-

fore we associated 933 keV instead of 989 keV to the Cobalt Compton energy and this value permits better linear calibration.

The calibration was performed by putting on ordinate scale the Compton energies calculated and in the x axis the channel corresponding to the mean of the Gaussian curves obtained. A linear fit is usually carried in order to extract the calibration factor (the slope). The offset is usually greater than zero due to non linearity of the scintillation processes [36].

In our cases the offset is negative in all cases but for the solid polysiloxane detector where a different PM tube was used. To understand the physical reason of this result it has been decided to repeat the calibration of the system at a lower operating voltage of the PM tubes and with more sources. We found that the negative offset is explained by some amount of saturation of the PM tube signal. Indeed we operated the PM tube at 1500 V (which falls within the working range by Hamamatsu) while when working at 1300 V a better linearity and a positive offset is recovered (see Figure 6.6). The new calibration was performed a posteriori in order to understand but due to different coupling between scintillators and PM tubes it could not be applied to CN data.

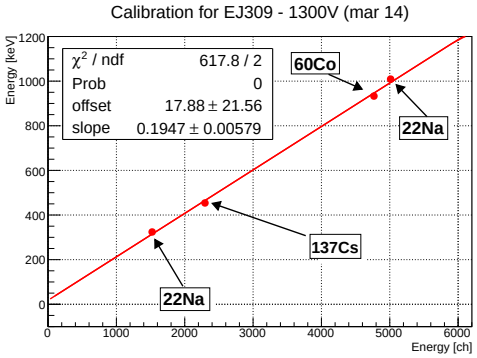

Figure 6.6: Calibration fit for the EJ309 scintillator at an operating voltage of the PM tube of 1300 V. The offset is positive and equal to (17.88 ± 21.56) keV.

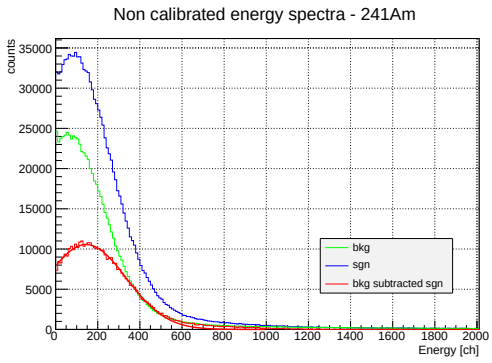

Figure 6.7: Americium energy spectrum. In blue the signal spectrum, in green the background spectrum and in red the subtraction over which the the Gaussian fit was done.

Thus for calibrating CN data we proceeded as follows. First, we added a fifth data point at low energy. To this purpose data for EJ309 and PM tube at HV = 1500 V was taken by exposing the sample with the ^{241}Am source. This emits a 59.6 keV γ-ray which converts in the scintillator mainly by photoelectric effect. The low signal from the 59.6 keV γ-ray was statistically extracted by the data sample, by subtracting the background (obtained acquiring without the source) as shown in Figure 6.7.

An empirical calibration was obtained from the five data points by fitting a power function. In Figure 6.8 is shown the calibration fit through the function

$$f(x) = ax^N + q \tag{6.2}$$

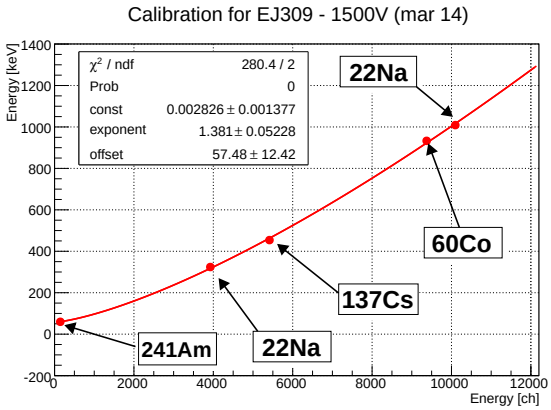

Figure 6.8: Calibration fit through (6.2) for EJ309 scintillator and an operating voltage for the PM tube of 1500 V.

where $f(x)$ stands for the energy in keV, x is the energy in channels extracted from the Compton edges and a, N and q are the fit parameters.

Since there was not the possibility of repeat the measurements at the CN accelerator with more sources and at a lower operating voltage of the PM tubes, it has been decided to take the offset obtained through the fit represented in Figure 6.8 and put it together with the only two available points acquired at the CN accelerator. Thus it is possible to use equation (6.2) to interpolate the data and to have a rough calibration fit. Figure 6.9 shows the fits over the three points for all the scintillator tested, compared with the straight line crossing the two original points. It is evident that beyond the range included between the original points, the linear approximation is not valid with the exception of the solid polysiloxane scintillator for which the two curves are very similar and both valid. However, for the uniformity with the other cases we have decided to use (6.2) even for the solid polysiloxane scintillator. The fit parameters are summarized in Table 6.3.

Table 6.3: Calibration parameters obtained for every detector tested.

Detector	a (eV)	N	q (keV)
EJ309	0.39±0.02	1.523±0.006	57.48 ±1.01
TPTMTS1	5.0±0.3	1.267±0.006	57.48 ±1.04
TPTMTS2	4.5±0.2	1.266±0.005	57.48±1.00
TPTMTS4	11.4±0.4	1.178±0.004	57.48±1.00
PPTMTS1	2.2±0.1	1.350 ± 0.005	57.48± 1.01
STD 5″	113±4	0.984 ±0.004	57.48± 1.00

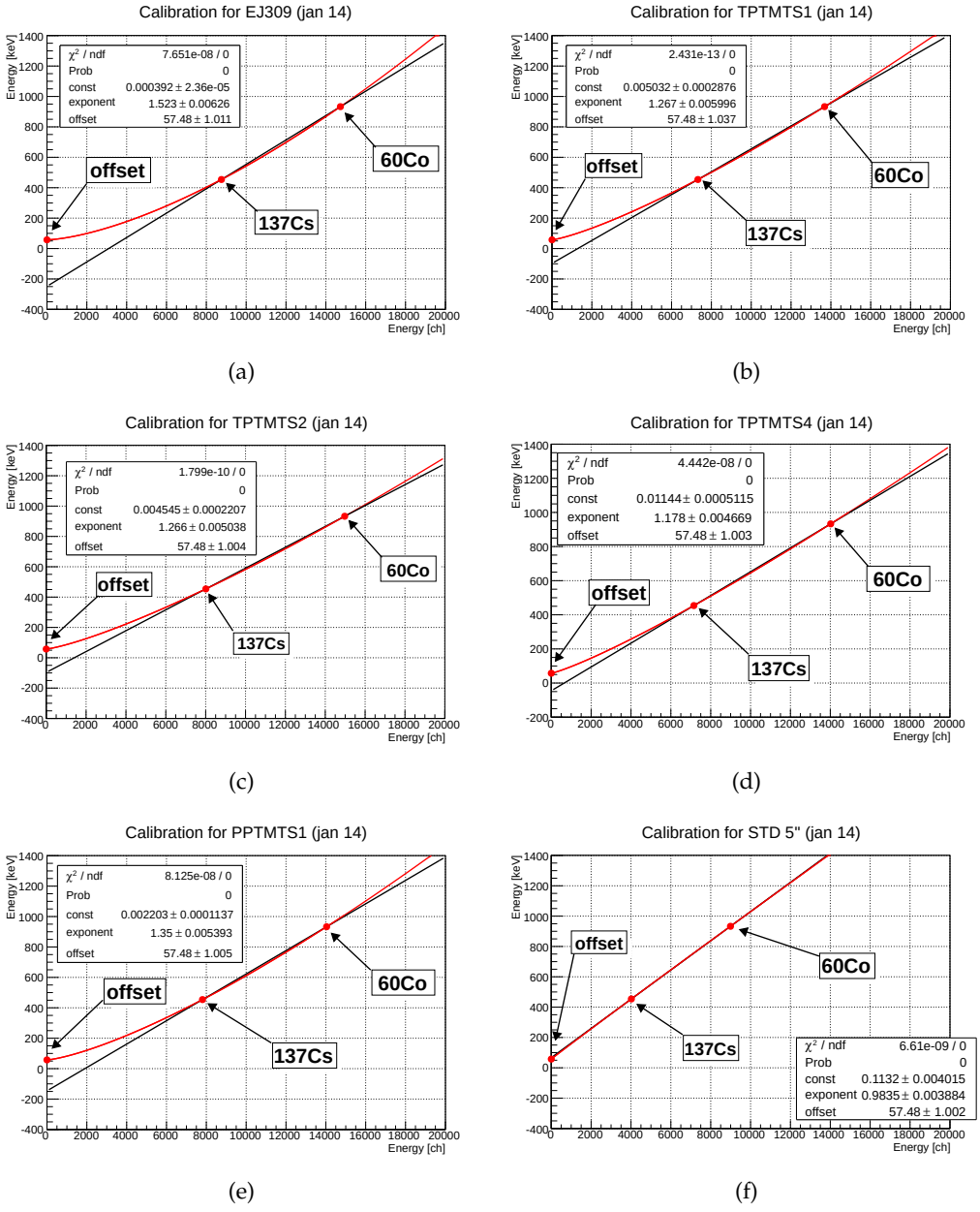

Figure 6.9: Calibration fit for the detector tested during the measurements at the CN accelerator last January.

6.3 Preliminary Analysis and Average Shapes

The data analysis has been carried out in C++ using the ROOT environment [37]. The preliminary analysis of the data acquired consists in the generation of the average shape for neutrons and γ-rays. To obtain this result some preliminary operations must be applied on the rough shapes.

First of all the baseline on each signal has to be subtracted in order to shift the shapes at the same amplitude scale. The baseline is calculated as the average amplitude of the first 10 samples of each shape. Since we expect stable baselines, it is therefore necessary to control that the baseline distribution is narrow (few mV). When this does not occur, we imposed a cut in the baseline distribution. In general, if the light is read by PM tubes, the baseline is very narrow and it is not necessary to cut the distribution (Figure 6.10(a)). Using SiPM instead, the baseline has a wider distribution because it is common to have the tail of the previous pulses at the beginning of the acquisition window. For a preliminary analysis we decided to select only events with negligible pileup at beginning of the readout window. The selection is illustrated in Figure 6.10(b) (red lines) An example of a selected waveform with the baseline subtracted is shown in Figure 6.11.

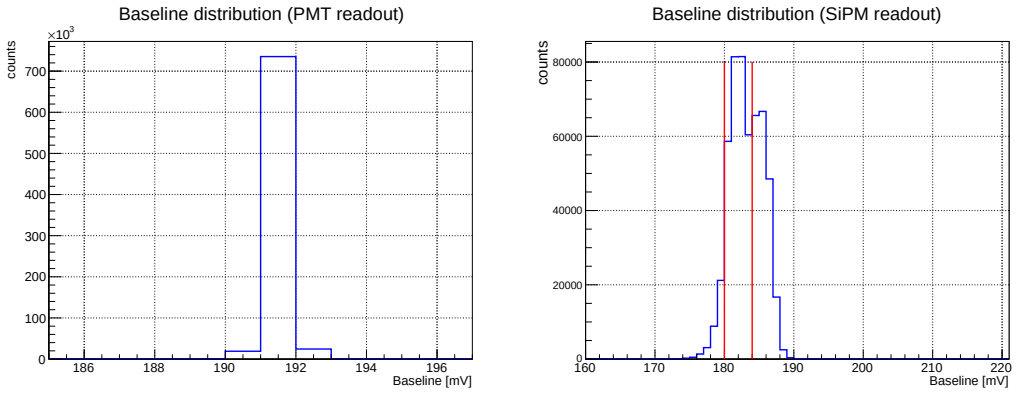

(a) PM tube readout, CN measurements.

(b) SiPM readout, AmBe acquisition.

Figure 6.10: The baseline distribution.

After baseline subtraction, the distribution of the shapes' maxima (called rawmax) is drawn. The rawmax distribution gives a first information about the energy spectrum. If some signals saturate (namely the maximum reach the end of the scale) and a background at low energy is present, it could be necessary to cut the maxima distribution. For PM tube readout a typical rawmax spectrum is given in Figure 6.12(a). Figure 6.12(b) instead shows the rawmax spectrum for SiPM measurements.

Eventually, we controlled the rawmax position along the time axis discarding signals that are shifted in the temporal scale. Alternatively the distribution of the time of constant fraction discrimination (tcfd) can be studied. We defined tcfd as the time where the amplitude reaches the 50% of its maximum in the leading front

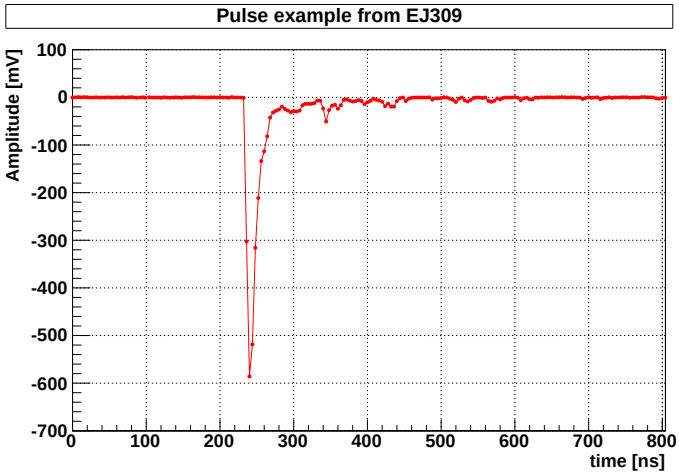

Figure 6.11: A shape example with the baseline subtracted.

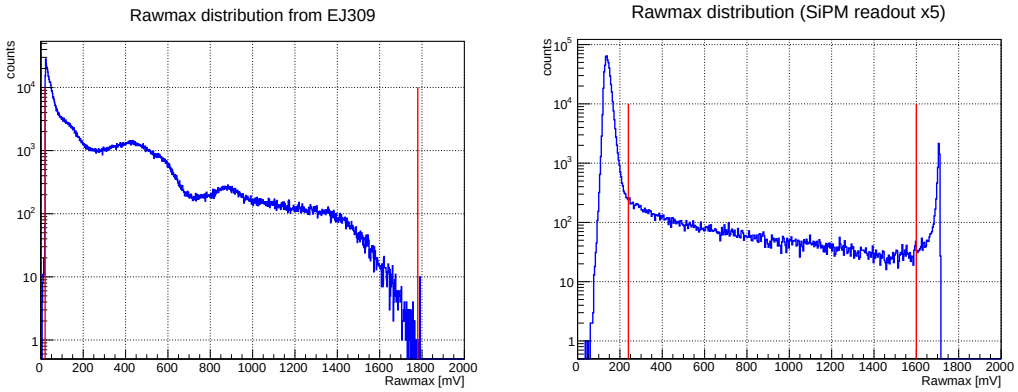

(a) PMT readout, CN measurements.

(b) SiPM readout, AmBe acquisition.

Figure 6.12: The rawmax distribution with the cuts (red lines) applied.

of the signal and it is used as the reference time when calculating the time of flight of the particle.

For enhancing the PSD parameter the shapes were filtered by a low pass filter with time constant RC (see Appendix A).

Since the preliminary analysis between the PM tube light readout and the SiPM light readout is different, we proceed by presenting separately the results for the two readout modes.

PM tube light readout

For CN measurements, in order to distinguish γ-ray from neutron pulses, the time of flight of the two particles has been measured exploiting the time information supplied from the pickup (see section 4.3 in chapter 4). The time of flight is the dif-

ference between the tcfd of the detector signal and the tcfd of the pickup signal. For enhancing the signal to noise ratio, the pickup tcfd was calculated on the average of three subsequent pulses. In Figure 6.13 two examples of TOF distribution, for a liquid and the solid polysiloxane detectors, are shown where the gates selected for γ-ray and neutron pulses are also indicated.

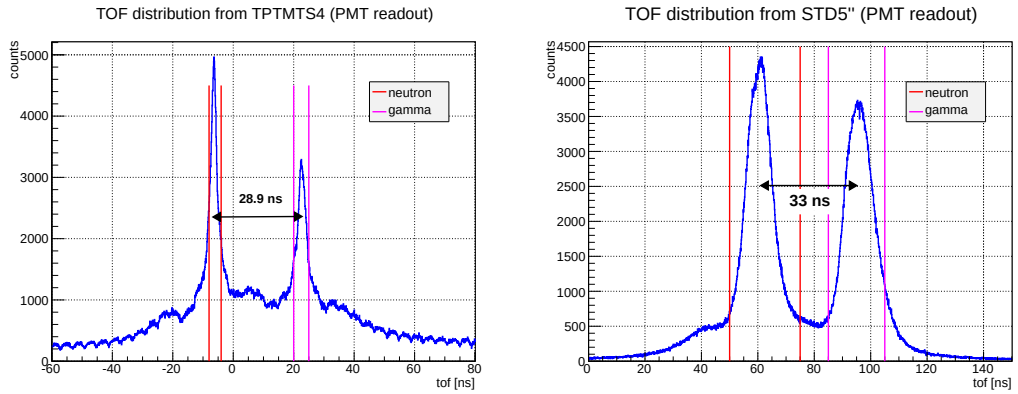

(a) Liquid oligosiloxane.

(b) Solid polysiloxane.

Figure 6.13: The TOF distribution from the CN measurements. The gate for γ-ray and neutron shapes are indicated.

The temporal distance between the two main peaks represents the difference between the times of flight from the target to the detector for the two particles. It has been controlled that it was compatible with the geometry of the apparatus and the maximum energy of neutron. Due to problems with the accelerator, the beam bunches presented irregular and instable patterns resulting in TOF distributions with high level of background.

The average shapes are then obtained by inverting and normalizing every shape to the rawmax and aligning them in the temporal axis. In Figures 6.14 and 6.15 the average shapes for the detectors tested during CN measurements are presented. The average is done on the same number of shapes (several thousands).

It is noteworthy that a hundred nanosecond after the peak amplitude two bumps appear. In order to check whether the effect was due to the PM tube system (signal reflection due to impedance mismatch), we illuminated them in laboratory with a pulsed laser. We found indeed similar bumps, just shifted, due to different cable length. The effect was mitigated by low-pass filtering the signal.

In case of the 5 inch PM tube, the bumps are less relevant because the PM tube is slower and integrates more signal.

SiPM light readout

Since in this case a TOF measurement was not possible (measurements in laboratory without a timing reference), the average shapes have been calculated analysing separately the acquisition with the γ-ray, the neutron and the α sources. The proce-

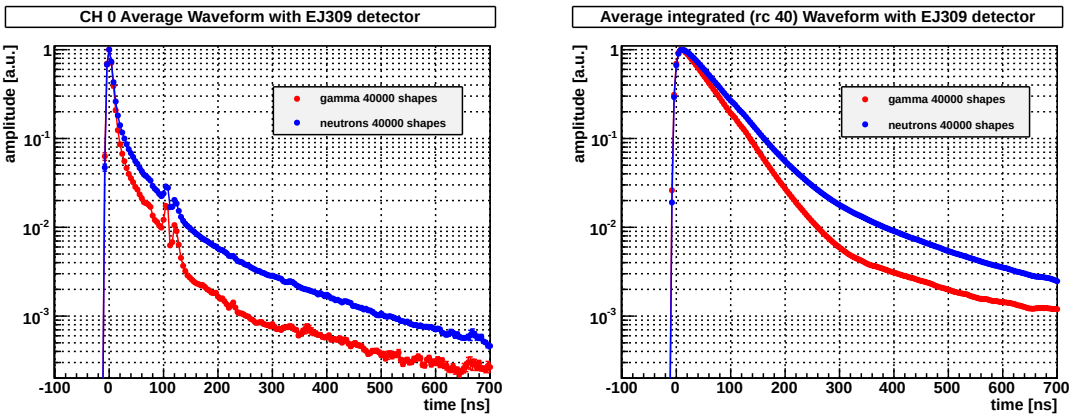

(a) EJ309 detector.

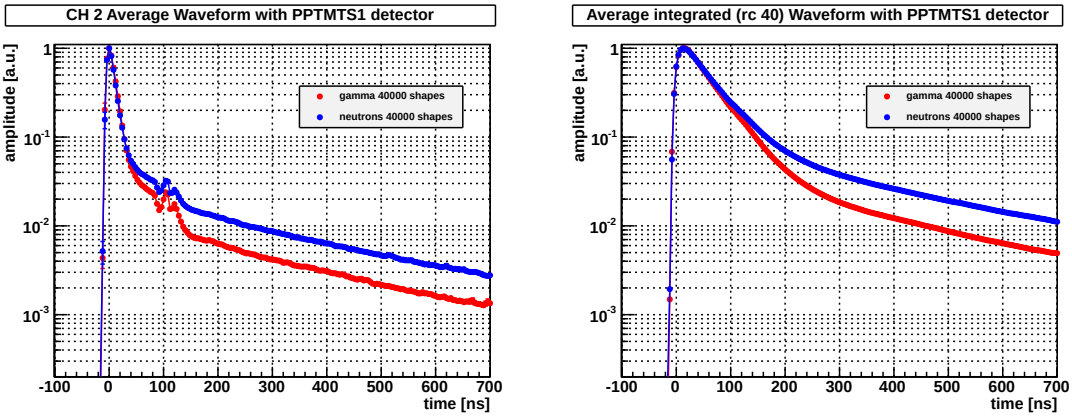

(b) PPTMTS1 detector.

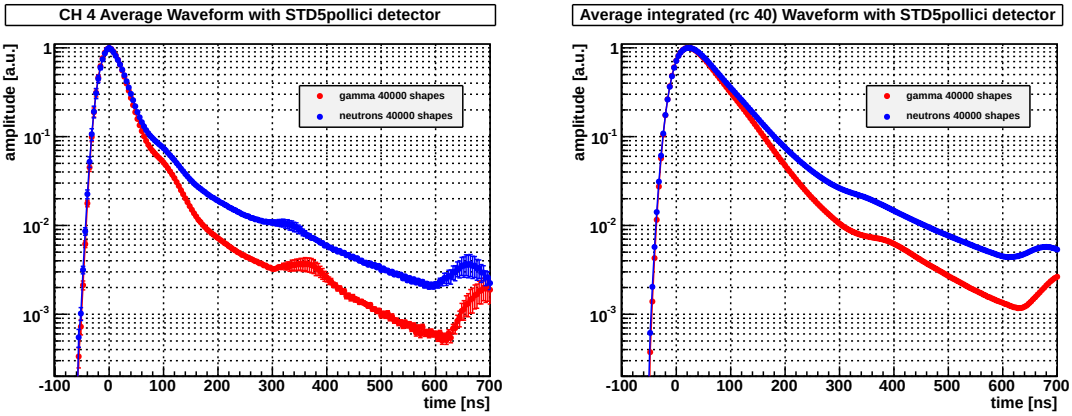

(c) STD5″

Figure 6.14: Average shape for the detectors tested during the CN measurements. On the right the original shapes, on the left the shapes after having applied the integration filter.

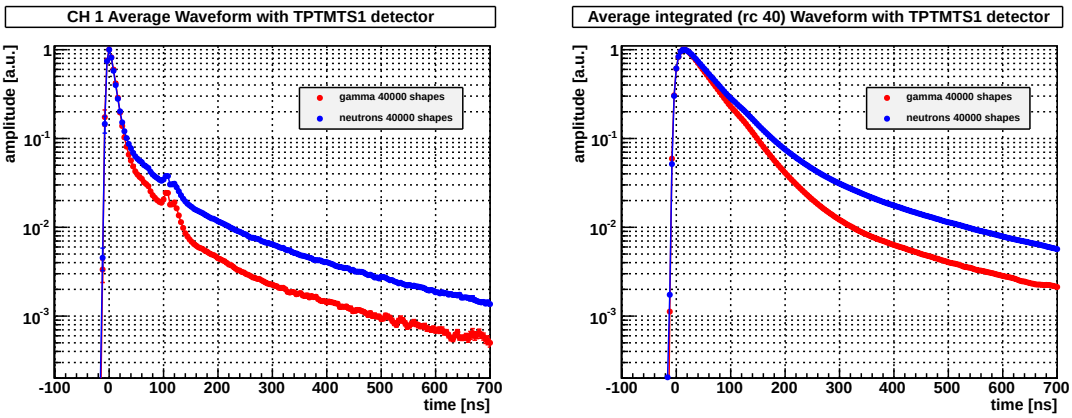

(a) TPTMTS1 detector.

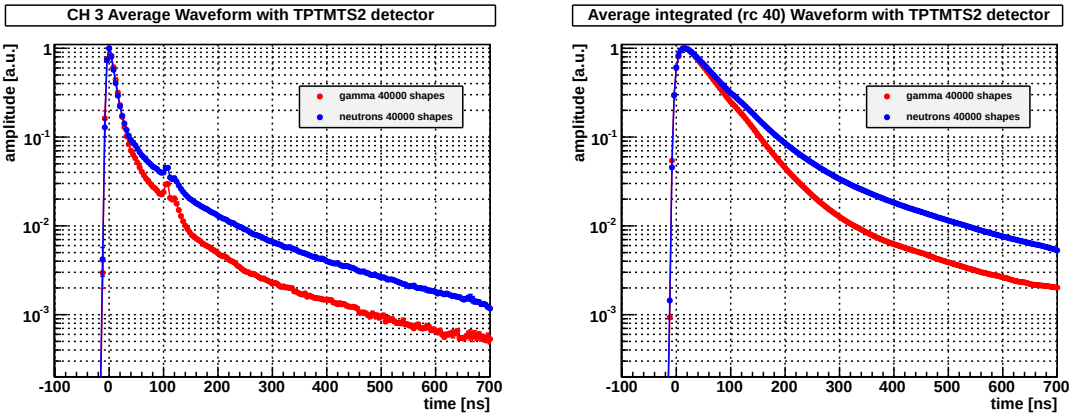

(b) TPTMTS2 detector.

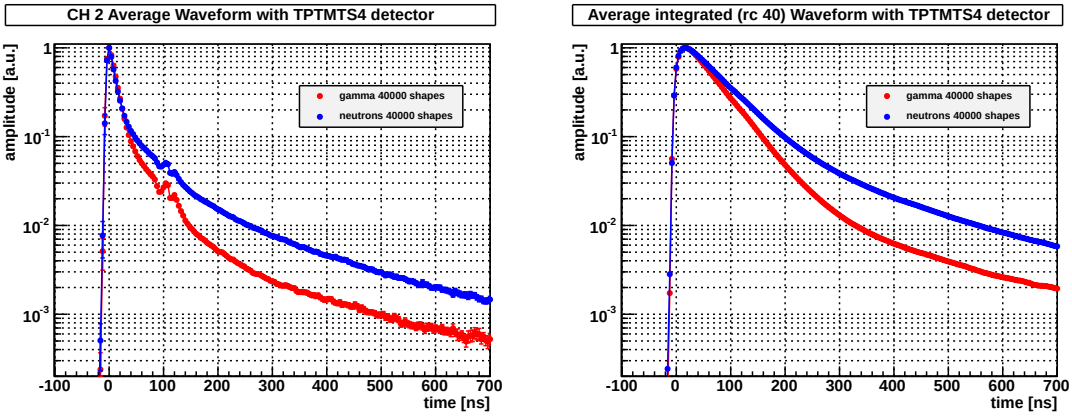

(c) TPTMTS4 detector.

Figure 6.15: Average shape for the detectors tested during the CN measurements. On the right the original shapes, on the left the shapes after having applied the integration filter.

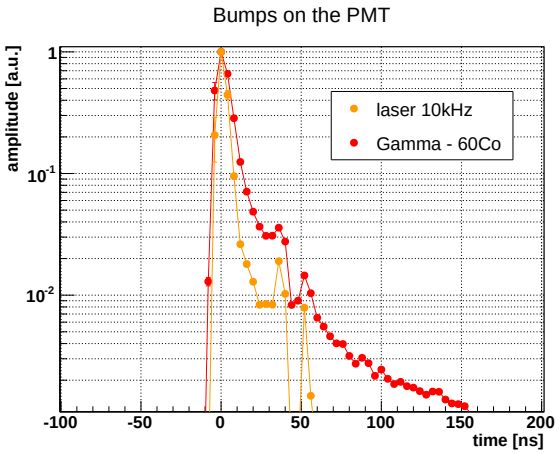

Figure 6.16: The PM tube bumps. The scintillation signal (red) superimposed on the PM tube signal (orange).

dure was the same of the case of PM tubes at CN accelerator namely every shapes were inverted, normalized and temporal aligned. Moreover the average shapes were filtered according to equation (5.5) to reduce the effect of the electronics on the pulse shapes. The resulting average shapes for the EJ309 and TPTMTS4 detectors can be seen in Figure 6.17 and 6.18 respectively.

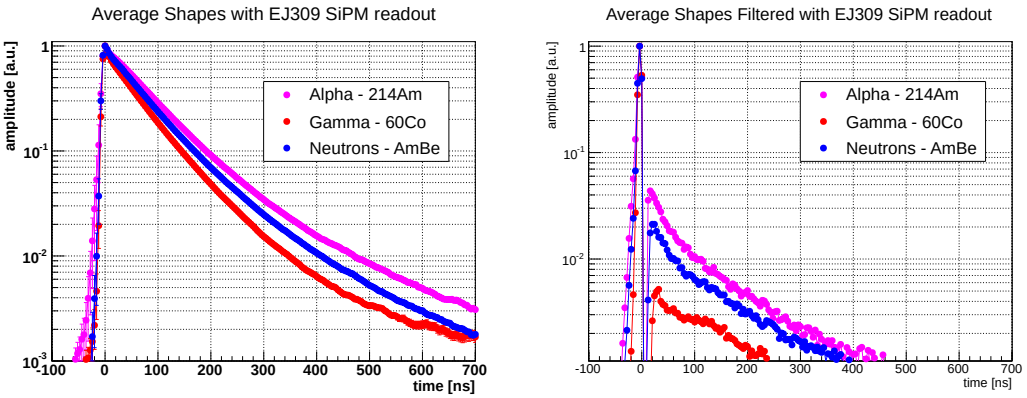

(a) Average shapes

(b) Average shapes filtered

Figure 6.17: Average shapes for EJ309 coupled with SiPM.

Interesting is also the raw energy spectrum obtained calculating the integral of the pulse (low-pass filtered with time constant RC = 5 ns) between 12 ns before and 120 ns after the peak amplitude. Due to the SiPM sensitivity to single photons it is possible to distinguish the firsts photoelectron peaks at low energy. (Figure 6.19(a)). Determining their distance estimated the number of photoelectrons that generates the signal of a particle (for example an α from ^{241}Am), simply by dividing the mean energy of the particle for this distance (the amount of energy for each photoelec-

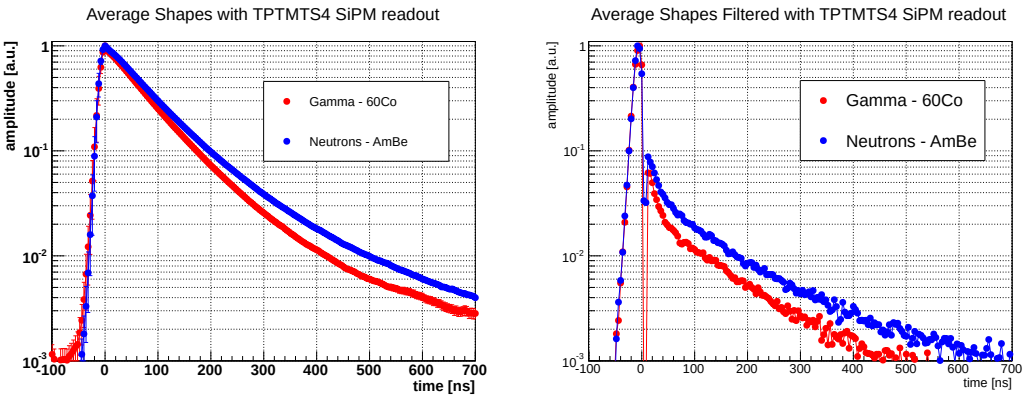

(a) Average shapes (b) Average shapes filtered

Figure 6.18: Average shapes for TPTMTS4 coupled with SiPM.

tron). In our case the first photoelectron peak is at about 700 channels (corresponding to signal of amplitude of 12 mV) separated by the second one by 650 channels. The average energy of the α particle form ^{241}Am stands at about 47000 channels so the α signals are formed by about 70 photoelectrons (see Figure 6.19(b)). Knowing the PDE of the SiPM, it is possible to estimate to the average number of of photons that generated the pulses.

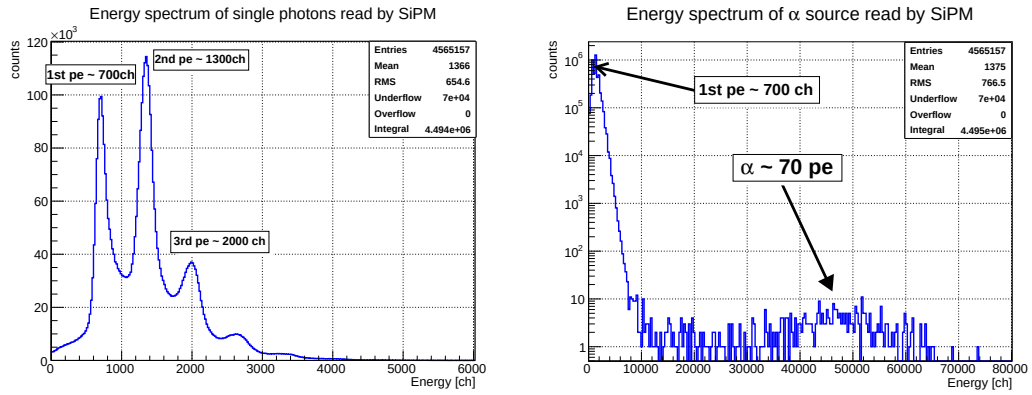

(a) Raw energy for single photoelectrons peak. (b) Raw energy for α particles.

Figure 6.19: Energy spectrum acquired with SiPM exposed to an α source.

6.4 Pulse Shape Analysis

We have studied the charge comparison, the zero crossing and the pulse gradient algorithms for the CN measurents and the zero crossing and the photons counting for the laboratory measurements. We proceed by discussing each one of them justifying the choices made.

6.4.1 CN measurements

Charge comparison Method

For the charge comparison method the starting point of the fast integral was set to 12 ns before the maximum and the end point of the slow integral was set 1000 ns after the peak amplitude. For the starting point of the slow integral that coincides with the end point of the fast integral, we used a value of 50 ns, basing the choice on the average shapes. We defined the discrimination parameter as follow:

$$PSD_{CC} = \frac{10 \cdot slow}{fast + slow} \tag{6.3}$$

In order to optimize the integration time constant (RC) to apply the low pass filter to the shapes, we evaluated the difference between the PSD parameter measured on the γ-ray average shape and the PSD parameter measured on the neutron average shape varying the RC constant. The dependence for all detectors is illustrated in Figure 6.20. The better compromise is given by RC = 40 ns. Therefore, before the calculation of the PSD parameter on the single shapes the pulses were integrated using this time constant. The PSD parameter distribution against energy is given in Figure 6.21 where the two populations are visible.

The two populations are clearly distinguishable in every cases but for solid polysiloxane which deserves further studies for understanding the inferior performances

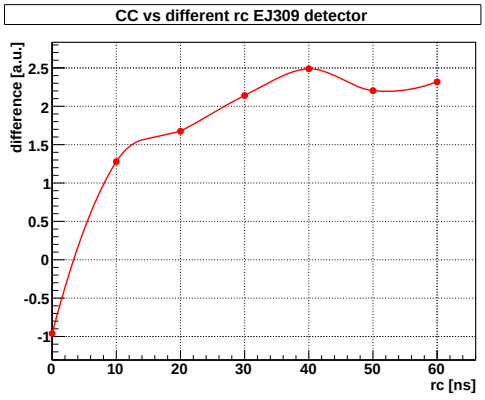

(a) EJ309

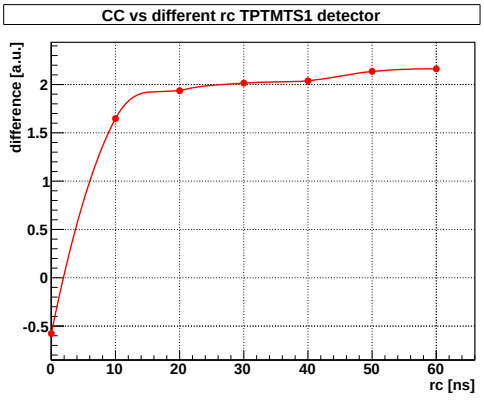

(b) TPTMTS1

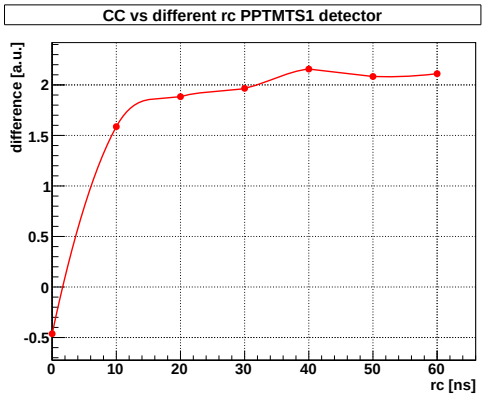

(c) PPTMTS1

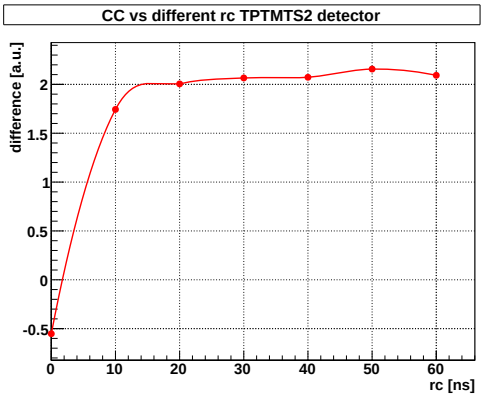

(d) TPTMTS2

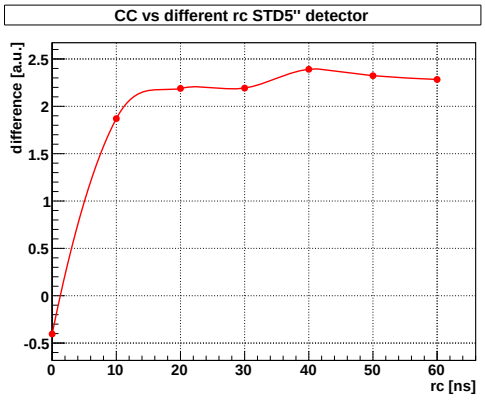

(e) STD5″

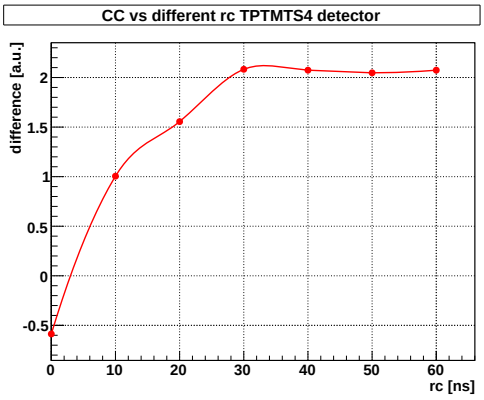

(f) TPTMTS4

Figure 6.20: The difference between the PSD parameter measured on the average γ-ray and neutron shapes as a function of the integration time constant (RC).

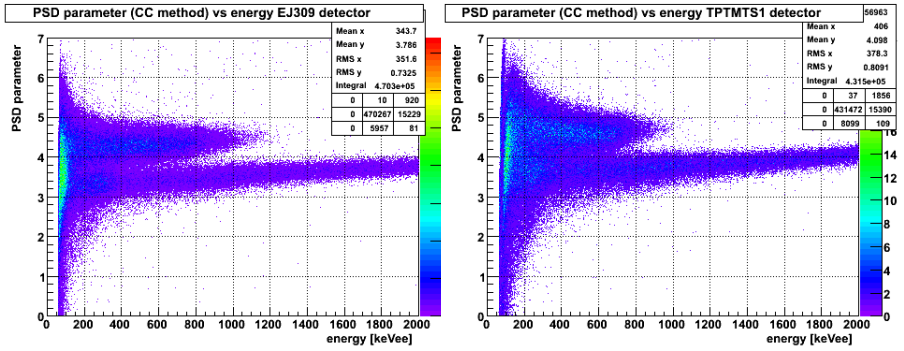

(a) EJ309 (b) TPTMTS1

(c) PPTMTS1 (d) TPTMTS2

(e) STD5″ (f) TPTMTS4

Figure 6.21: The PSD parameter distribution as a function of energy for the charge comparison method.

Zero crossing method

In this case, a study as a function of the percentage of the time right has been carried out before measuring the PSD parameter (ZCO) on the single shapes. In Figure 6.22 the dependence is reported both on the original average shapes and on the integrated average shapes (RC = 40 ns). In the latter case the ZCO is systematically better. In order to maximize the parameter we chose the 6% of the peak amplitude as the time right threshold. The better ZCO parameter measured on the average shape at lower threshold is an effect of the average. Under 6% in fact, the fluctuations of the background of the single shapes become important so the measurement of the ZCO would be unreliable.

The ZCO distributions as a function of the energy is shown in Figure 6.23. Even in this case the solid polysiloxane scintillator does not show an appreciable separation.

Pulse Gradient Analysis

In this case, we investigated the threshold where the difference of the sample amplitudes between γ-ray and neutron pulses is maximized. The dependence are reported in Figure 6.24. It is not possible to fix the same threshold for all the detectors (because the dependence are different) so every case was treated separately. The PSD parameter was

$$PSD_{pga} = \frac{\text{sample amplitude}}{\text{sample amplitude} + \text{peak amplitude}} \tag{6.4}$$

The distribution as a function of energy is shown in Figure 6.25 where the two populations are visible in every case but the solid polysiloxane.

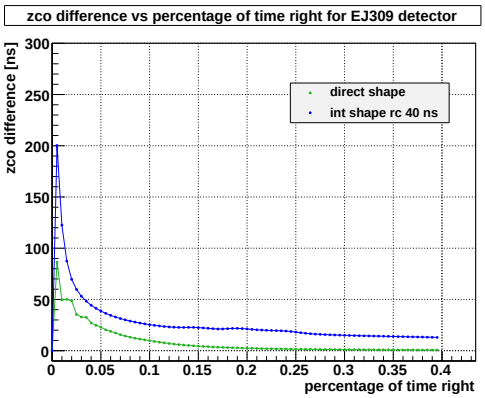

(a) EJ309

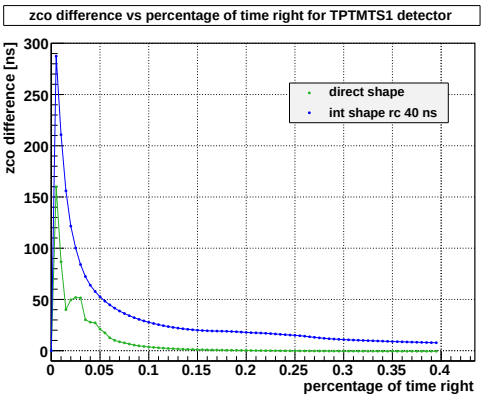

(b) TPTMTS1

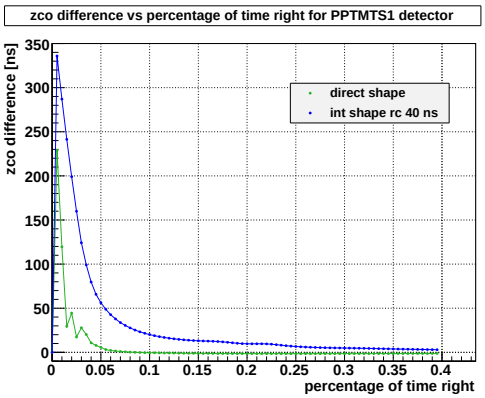

(c) PPTMTS1

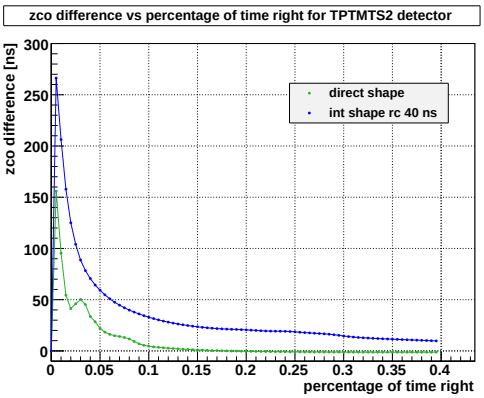

(d) TPTMTS2

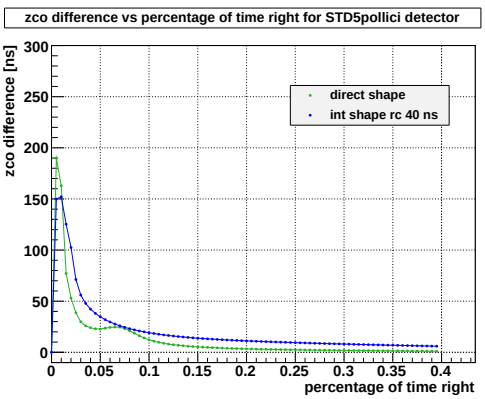

(e) STD5″

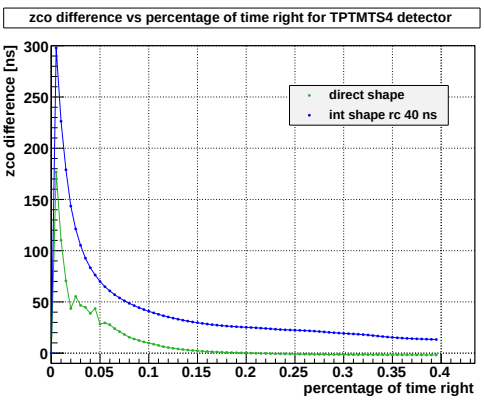

(f) TPTMTS4

Figure 6.22: The zero crossing parameter as a function of the percentage of time right.

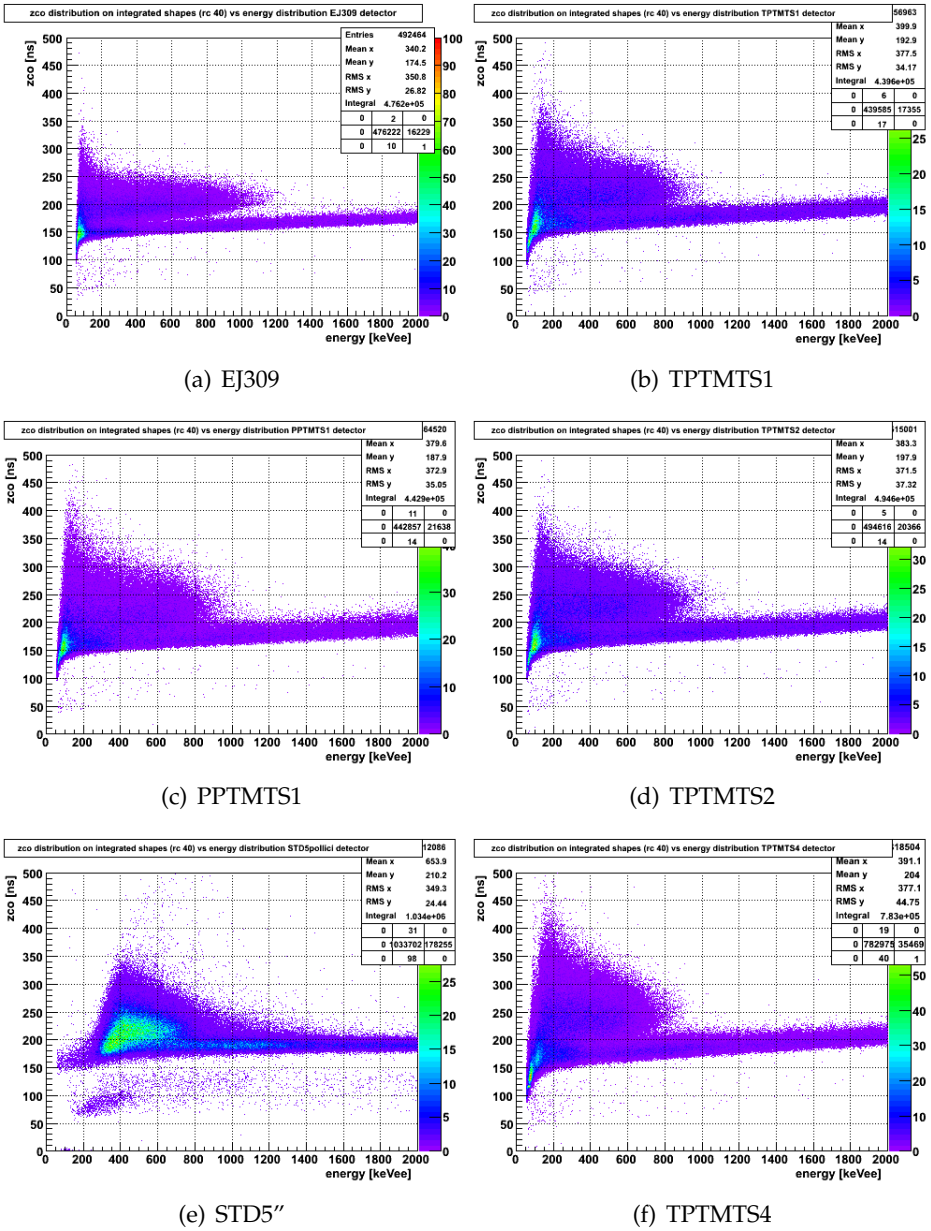

(a) EJ309 (b) TPTMTS1

(c) PPTMTS1 (d) TPTMTS2

(e) STD5″ (f) TPTMTS4

Figure 6.23: The ZCO parameter distribution as a function of energy for the zero crossing method.

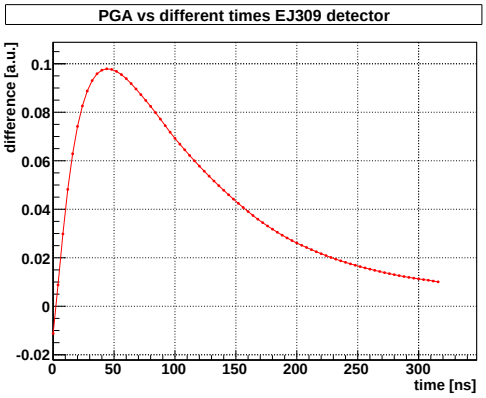

(a) EJ309

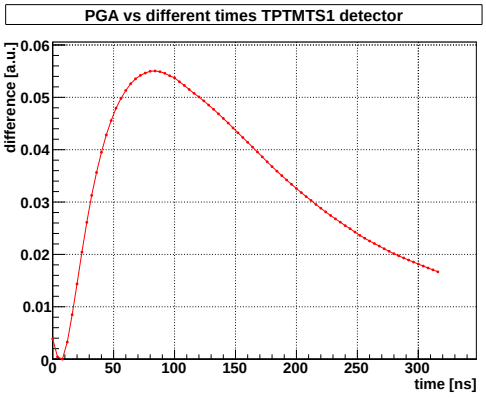

(b) TPTMTS1

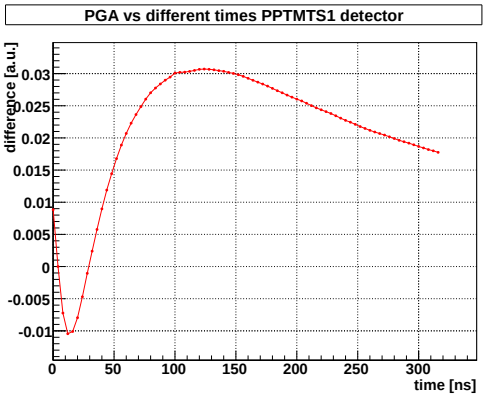

(c) PPTMTS1

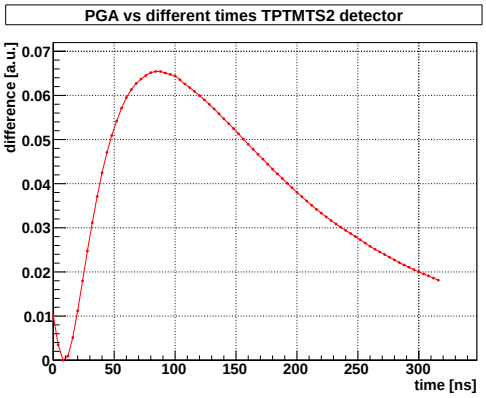

(d) TPTMTS2

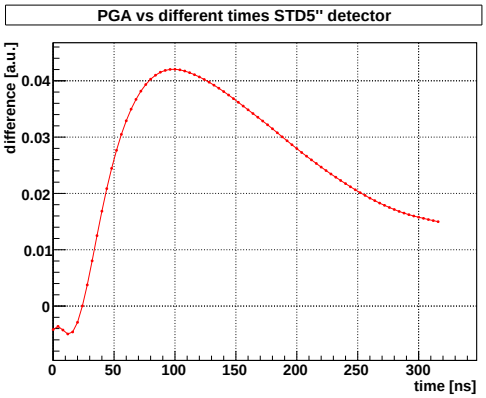

(e) STD5″

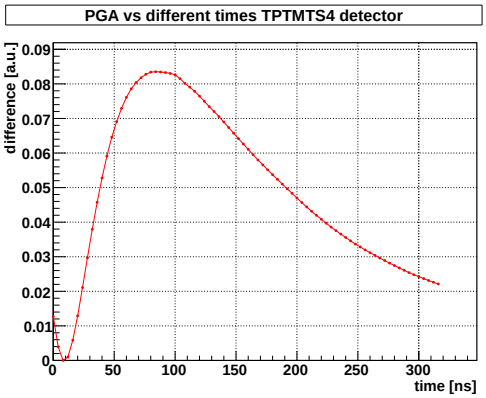

(f) TPTMTS4

Figure 6.24: The difference between the sample amplitudes for γ-ray and neutron pulses as a function of the time after the peak amplitude.

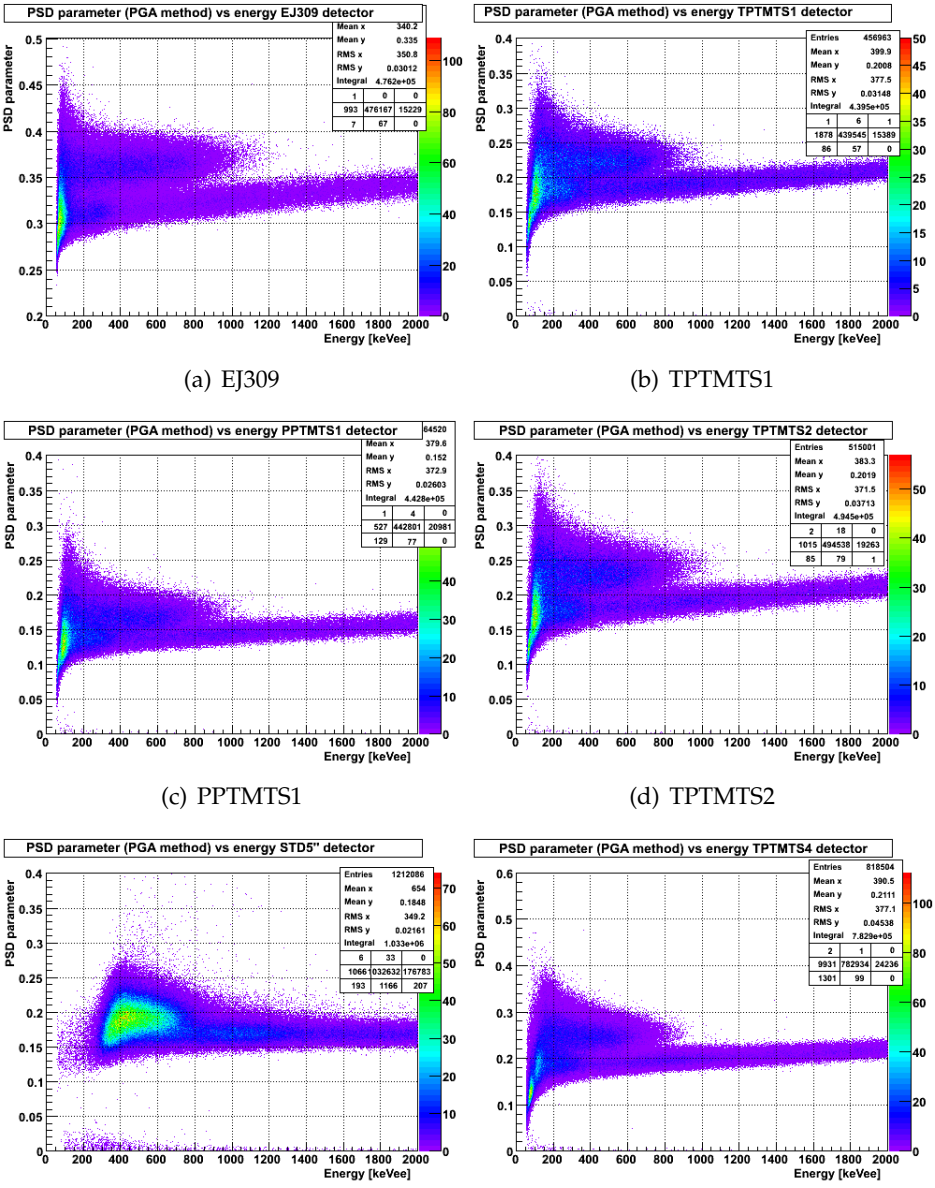

(a) EJ309 (b) TPTMTS1

(c) PPTMTS1 (d) TPTMTS2

(e) STD5″ (f) TPTMTS4

Figure 6.25: The PSD parameter distribution as a function of energy for the pulses gradient analysis method.

6.4.2 SiPM Light read out

Zero crossing method

The zero crossing method was used to test pulse shape discrimination also in case of light readout through SiPM. Being not available a TOF measurement, the ZCO parameter was calculated separately on γ-ray source, on neutron source and on α source acquisitions. This procedure result in three different distributions that we present overlapped to supply a comparison. It is evident that the α distribution is shifted with respect to the γ-rays distribution. Concerning neutrons two populations are clearly visible, indicating that gamma background was not totally shielded. The ZCO distribution for the detector tested is presented in Figure 6.26.

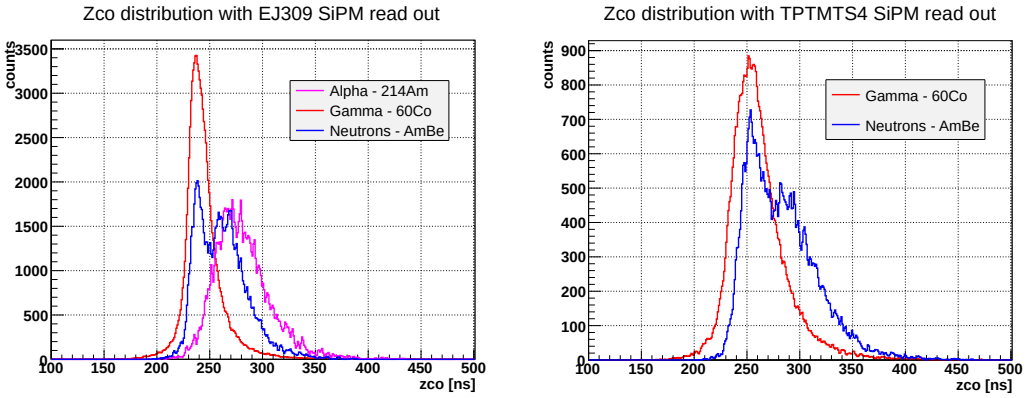

(a) EJ309 (b) TPTMTS4

Figure 6.26: The ZCO distribution for the detectors tested with SiPM.

Photons Counting

The photons counting method was tested on SiPM acquisitions. The number of photons counted on the tails following the procedure described in chapter 5 (section 5.7), is normalized to the peak. The gate for the count was fixed between 24 ns and 324 ns after the peak amplitude. The distributions are shown in Figure 6.27. Two populations are quite well distinguishable for EJ309 detector where the γ-rays background is visible in the neutron distribution

In the case of the TPTMTS4 sample just one population is evident. We believe that this effect is related to a somehow lower light yield shown by the specific TPTMTS4 sample in this set of measurements.

As a general comment, we believe that the use of larger scintillator samples, readout by SiPMs with large area will greatly improve PSD performances with respect to these preliminary tests. The more if SiPMs will be operated at higher over-voltage and consequently higher PDE.

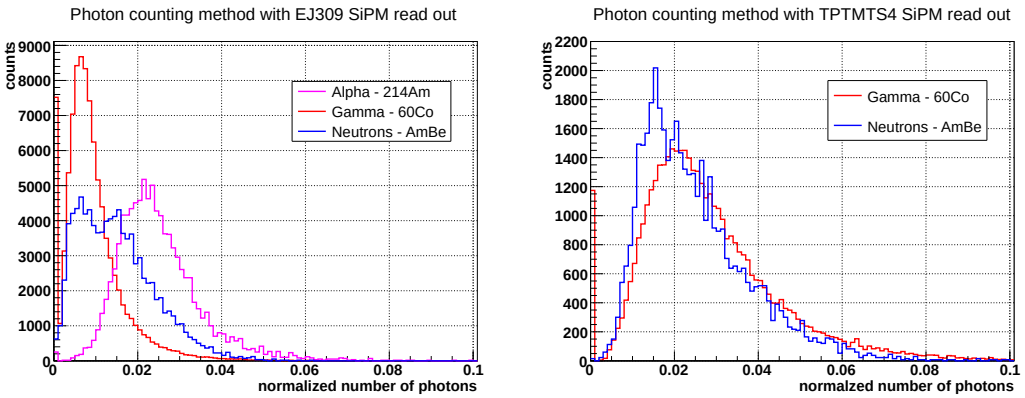

(a) EJ309 (b) TPTMTS4

Figure 6.27: The normalized photons distribution for the detectors tested with SiPM.

6.5 Comparison between SiPM and PM tubes

In order to compare the SiPM readout with the PM tube readout we have realized the average shapes and ZCO distribution based on acquisition with PM tube lead to the same conditions as the SiPM acquisition, namely same gain and same volume of scintillators. The Average shapes are shown in Figure 6.28. Clear is the comparison

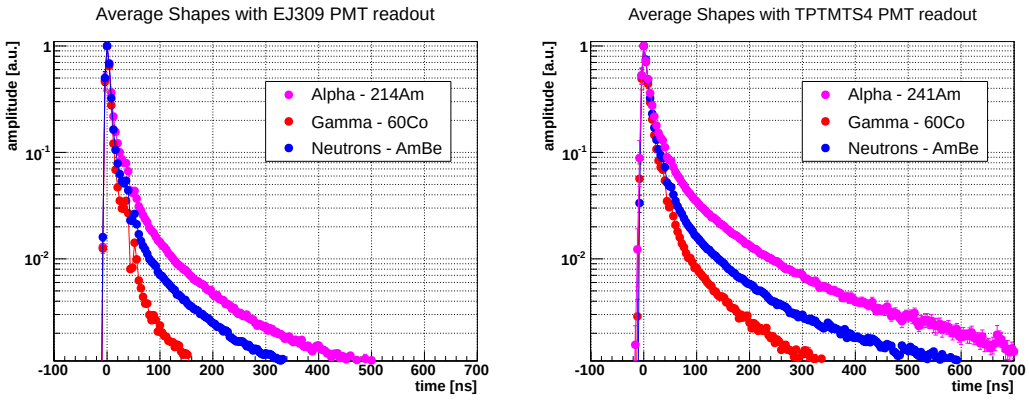

(a) EJ309 (b) TPTMTS

Figure 6.28: Average shapes for PM tube in the same conditions of SiPM acquisitions.

of the decay time constants of these shapes with the results obtained using the Bollinger method (see section 6.1): the TPTMTS4 signals crosses 1‰of the peak amplitude at a time approximately a factor of two later than for EJ309. The effect is noticeable even in the CN measurements (Figures 6.14 and 6.15). This confirms that the liquid oligosiloxane samples has decay time constants longer than the EJ309.

The ZCO distribution (Figure 6.29 vs Figure 6.26) for SiPM tells us that the pulse shape discrimination between SiPM and PM tube is still better with PM tube.

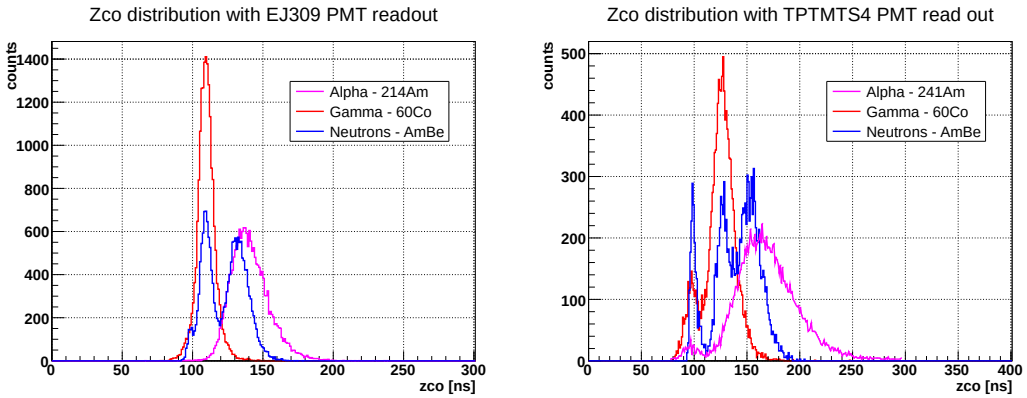

(a) EJ309 (b) TPTMTS

Figure 6.29: ZCO distribution for PM tube in the same conditions of SiPM acquisitions.

Regarding the ZCO distribution for the TPTMTS4 a third peak on the left of the γ-ray peak is noticeable for all the sources. This is due to small amplitude events with sharp waveform that deserve further investigation. Concerning the regular populations we observe that also in this case TPTMTS4 performances are worse than EJ309.

As previously noted, the use of larger scintillator samples, and SiPMs with large area will greatly improve PSD performances. Improvements are also expected by the use of NUV SiPMs with enhanced PDE in the blue and UV region.

6.6 Results

To qualify the results of the pulse shape analysis, comparing between the algorithms implemented and the detectors employed, is usually introduced the Figure of Merit (FOM) . The FOM is defined as the ratio between the peak separation and the sum of the FWHM (full width at half maximum) calculated on the γ-ray and neutron distributions, namely:

$$FOM = \frac{peak\,separation}{FWHM_n + FWHM_\gamma} \tag{6.5}$$

FOM typical values ranges from 0.2 and 2 [16]. Obviously, greater is the FOM better is the discrimination.

In order to study the discrimination properties as a function of the energy threshold, the FOM were calculated by projecting the PSD parameter distributions as a function of energy at different energy threshold. As an example we show the result of this operation on EJ309 for the ZCO method and the pulse gradient analysis algorithm (Figure 6.30), where the energy window used to project the distribution was 50 keV_{ee} wide.

The FOM calculated on each detector and for each method implemented are summarized in Tables 6.4 and 6.5.

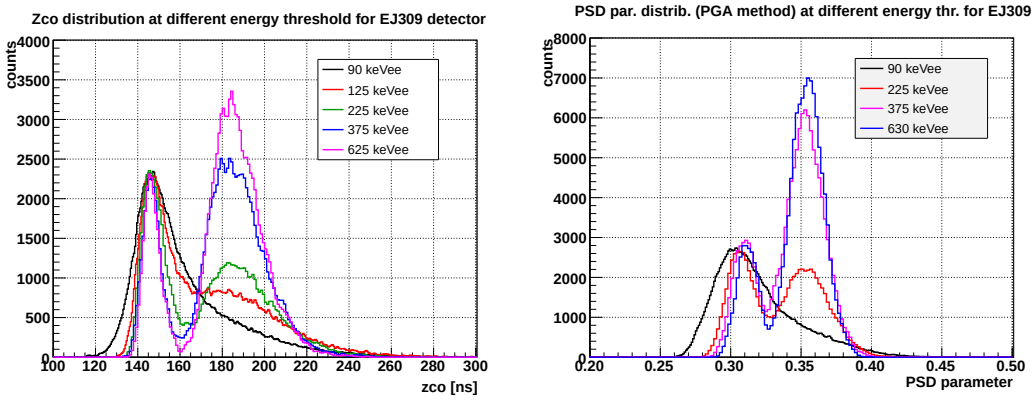

(a) (b)

Figure 6.30: The PSD parameter distribution at different energy thresholds. For each of these distribution the FOM was calculated.

Table 6.4: FOM calculated on the EJ309 scintillator

Algorithm	Energy [keV_{ee}]	FOM
CC	145	0.400± 0.008
	225	0.645 ± 0.006
	375	0.909 ± 0.010
	625	1.114 ± 0.012
	830	1.330 ± 0.016
ZCO	125	0.389 ±0.010
	225	0.771 ±0.009
	375	0.896 ±0.005
	625	1.281 ±0.007
PGA	125	0.475 ± 0.008
	225	0.751± 0.005
	375	0.846± 0.003
	630	0.902± 0.003

Eventually, we show the dependence of the FOM from the energy threshold at fixed detector (Figure 6.31) and at fixed method (Figure 6.32). In the former case the methods' comparison is given and results that for the EJ309 the methods are comparable below 400 keV_{ee}. At higher energy thresholds the charge comparison and ZCO method result in better FOM than pulse gradient analysis. For the liquid oligosiloxane samples the charge comparison is systematically better than other methods. In the latter case instead the detector are compared. For the ZCO method and for the pulse gradient analysis the EJ309 is systematically better than the other scintillators but in the charge comparison method the TPTMTS2 and the PPTMTS1

Table 6.5: FOM calculated on the liquid oligosiloxane samples.

Scintillator	Algorithm	Energy [keV$_{ee}$]	FOM
TPTMTS1	CC	270	0.527 ± 0.006
		430	0.656 ± 0.013
		630	0.936 ± 0.010
		725	1.115 ± 0.012
	ZCO	275	0.337± 0.009
		430	0.664 ± 0.004
		625	0.762 ± 0.006
	PGA	275	0.464±0.010
		430	0.566± 0.009
		625	0.643 ±0.010
		725	0.703 ±0.013
TPTMTS2	CC	275	0.741 ± 0.006
		430	0.940 ± 0.010
		670	1.185 ± 0.011
	ZCO	275	0.487 ±0.012
		430	0.738 ±0.012
		675	0.795 ± 0.013
	PGA	275	0.539 ± 0.007
		430	0.663 ±0.008
		670	0.781 ±0.010
TPTMTS4	CC	275	0.704 ± 0.006
		425	0.839 ± 0.011
		630	1.135 ± 0.010
	ZCO	280	0.533 ±0.012
		425	0.757±0.005
		630	0.814±0.011
	PGA	280	0.565 ±0.006
		425	0.692± 0.005
		630	0.834± 0.009
PPTMTS1	CC	150	0.368 ±0.020
		275	0.709± 0.005
		375	0.806± 0.008
		525	0.963 ±0.009
		680	1.153 ±0.011
		730	1.180 ±0.013

have very similar FOM of that of the EJ309 especially between 300 and 700 keV_{ee}. Moreover the charge comparison method was the only way to realize Figures of Merit for the PPTMTS1. The results are very similar to EJ309.

The better oligosiloxane liquid detectors are TPTMTS2 and TPTMTS4 that approach FOM = 0.8 for ZCO and pulse gradient methods and FOM = 1 or better for the charge comparison method. The TPTMTS1 is systematically worse with better FOM = 0.75 with the ZCO method, better FOM = 0.7 for pulse gradient analysis and better FOM = 1.1 for the charge comparison. In any case the lower energy discrimination threshold is between 100 and 200 keV_{ee} for EJ309 and less than 300 keV_{ee} for the liquid oligosiloxane samples. The understand the reasons why the only methods to discriminate particles with the PPTMTS1 sample is the charge comparison algorithm and why the solid polysiloxane does not allow any discrimination are still to be studied.

The pulse shape analysis carried out reading out the light emitted by small scintillator volumes through SiPM, results in a slightly lower discrimination power than for PM tubes under similar conditions. On the other hand, the new original discrimination method of counting photons standing along the tails is promising with the EJ309 scinitillator. Additional work is deserved understand more in details and to improve these results in particular with the siloxane samples.

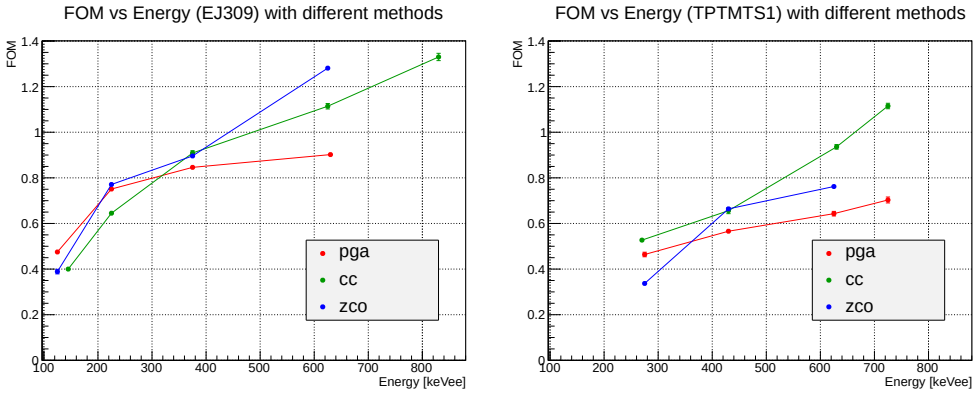

(a) EJ309

(b) TPTMTS1

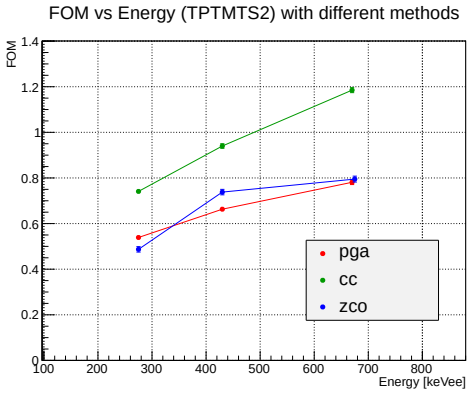

(c) TPTMTS2

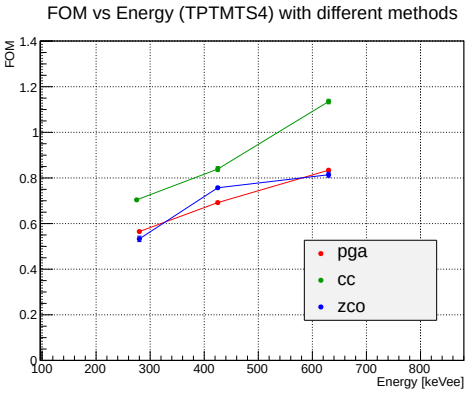

(d) TPTMTS4

Figure 6.31: Figure of Merit as a function of energy threshold. Methods comparison.

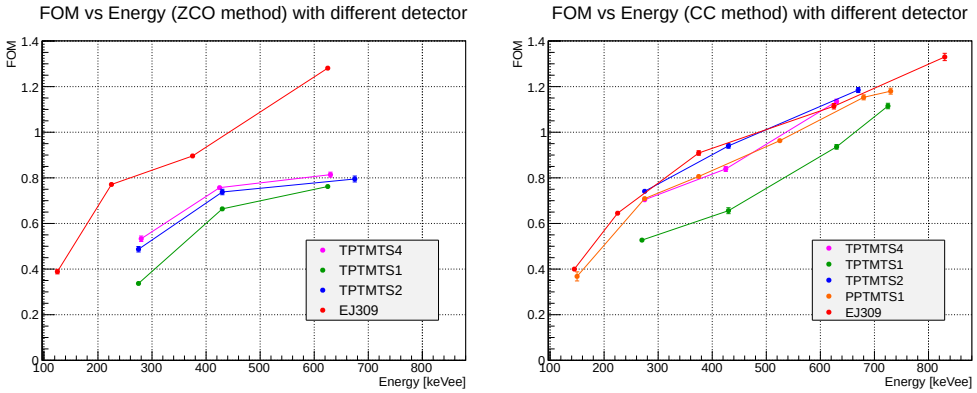

(a) ZCO method

(b) CC method

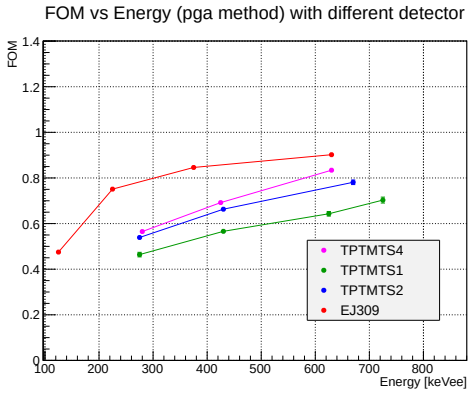

(c) PGA method

Figure 6.32: Figure of Merit as a function of energy threshold. Detector comparison.

Conclusions

This thesis' work was focused on the study of new means for neutron detection. In particular we investigated the use of new types of scintillators coupled with PM tubes and with new solid state detectors.

Various issues related to scintillating materials, photon detection and signal processing were addressed. This was an occasion for learning standard techniques and developing new ideas related to neutron detection.

The work has been divided in two parts. In the first part the attention was mainly focused on the pulse shape discrimination properties of new siloxane scintillators developed at LNL. The purpose was the study of scintillating materials able to detect neutrons and charged particles as well as γ radiation. Neutron fluxes, indeed, are often combined with a γ-rays background, thus a good neutron detector should be able to distinguish between them. Commercial solutions available are often toxic, flammable and polluting even if their properties of pulse shape discrimination are very good. Recently more and more solutions have been developed in order to provide cheap, not dangerous and efficient alternatives.

To this aim five siloxane scintillator samples were studied together with the commercial scintillator EJ309, for comparison purposes. They were exposed to a neutron flux produced by the $^7\mathrm{Li}(\mathrm{p},\mathrm{n})^7\mathrm{Be}$ reaction at the LNL Van der Graaff CN accelerator. Neutrons were separated from γ-rays through Time of Flight measurements. Three pulse shape discrimination algorithms were also implemented: the charge comparison, the zero crossing and the pulse gradient analysis methods. For each of them the Figure of Merit were calculated at different energy thresholds in order to qualify the results. All the detectors but the solid polysiloxane show good pulse shape discrimination properties. Moreover, all methods work quite well with the EJ309 for which the energy threshold for the neutron/γ discrimination is about 120 keV_{ee}. The analysis of oligosiloxane scintillators shows that the charge comparison method gives the best Figure of Merit for three of the four liquid samples tested. Noteworthy these results are very similar to the EJ309. Concerning the other methods, EJ309 performs better. Further studies are needed to understand these differences in more details, for instance concerning the different amount of quenching and a somehow lower light yield for protons and α particles.

The second aim of this work was the study of the performances of these materials coupled with the state of the art in solid state photodetectors, namely silicon photomultiplier. The use of these devises instead of the most common photomultiplier tubes is of great interest because of their superior amplitude and time res-

olution for single photons. We performed a preliminary study of the pulse shape discrimination with small area SiPM devises, reading out the light emitted by small scintillator volumes. The resulting discrimination power is slightly lower than for PM tubes under similar conditions. To our knowledge a study like this was never carried on up to now and should be considered quite preliminary. We believe that using larger area SiPM (matrices) and working at higher PDE will easily improve the results. For instance either simply working at higher over-voltage or exploiting the new "NUV" SiPM with high sensitivity in the UV region will provide immediate improvements. Moreover the SiPM readout allows the application of a new original discrimination method. This exploits the single photon counting capabilities offered by the SiPM. The discrimination performances achieved using this method appear good and quite promising with the EJ309 scinitllator. Additional work is deserved for the development of the method, in particular to understand the results with the siloxane samples.

The results obtained, although preliminary, are very innovative because a deep study of the topics presented in this thesis was never carried out before regarding both the pulse shape analysis of new siloxane materials and the light readout through SiPM. The success of this new line of research may find several fields of application ranging from the construction of new detectors for nuclear physics studies, to the development of cheap and eco-friendly radiation monitors and detectors. The latter could be the basic constituent of new generation detectors for nuclear medicine diagnostic tools.

Appendix A

Signal Shaping

This part has been taken from [3] and is reproduced here for completeness and to help the reader.

It is common to define the term RC shaping to indicate the use of passive resistor-capacitor networks to carry out a desired alteration in pulse shape. It is conventional to make a distinction between **differentiator** or *CR* networks, and **integrator** or *RC* networks. Since both operations act as filtering in the frequency domain the purpose of pulse shaping is to improve signal-to-noise ratio by limiting the response of the instrumentation to those frequency ranges in which the signal has useful components, while reducing the transmission of frequency components from the various sources of noise. In both types of network, the time constant $\tau = RC$ plays a critical role.

A.1 CR Differentiator or High-Pass Filter

A diagram of basic CR differentiator network is shown in Figure A.1. The input voltage E_{in} and output voltage E_{out} are related by

$$E_{in} = \frac{Q}{C} + E_{out} \tag{A.1}$$

where Q represents the charge stored across the capacitor. Now, differentiating with respect to time:

$$\frac{dE_{in}}{dt} = \frac{1}{C}\frac{dQ}{dt} + \frac{dE_{out}}{dt} \tag{A.2}$$

where $dQ/dt = i$ is the current through the circuit, and considering that $E_{out} = iR$, we obtain:

$$E_{out} + \tau\frac{dE_{out}}{dt} = \tau\frac{dE_{in}}{dt} \tag{A.3}$$

If RC is sufficiently small, the second term on the left can be neglected:

$$E_{out} \simeq \tau \frac{dE_{in}}{dt}. \tag{A.4}$$

The network, in the limit of small time constant, acts to produce an output E_{out} proportional to the time derivative of the input waveform E_{in}, hence the name differentiator.

In the opposite extreme of large time constant, we can neglect the first term on the left of (A.3) and we have:

$$\tau \frac{dE_{out}}{dt} \simeq \tau \frac{dE_{in}}{dt} \tag{A.5}$$

and performing the integration within the same time interval we obtain:

$$E_{out} \simeq E_{in} \tag{A.6}$$

so the filter output is the unaltered incoming waveform.

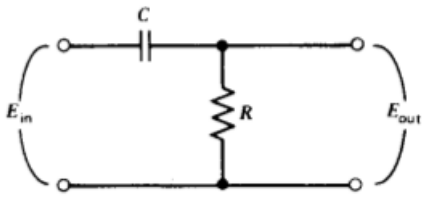

Figure A.1: A high-pass CR filter or differentiator network.

An example of application of CR high-pass filter on a typical shape from the tested scintillator is given in Figure A.2.

A.2 RC Integrator or Low-Pass Filter

When configured as shown in Figure A.3 a passive RC network can also serve as an integrator. The equation is now

$$E_{in} = iR + E_{out} \tag{A.7}$$

The current i represents the rate of charging or discharging of the capacitor

$$i = \frac{dQ}{dt} = C\frac{dV_c}{dt} \tag{A.8}$$

or

$$i = C\frac{dE_{out}}{dt} \tag{A.9}$$

Now combining (A.7) and (A.9) we obtain

$$E_{in} = \tau \frac{E_{out}}{dt} + E_{out} \tag{A.10}$$

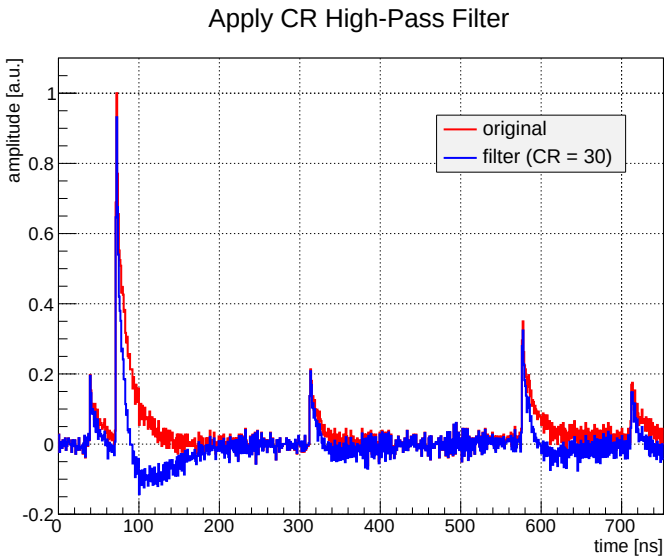

Figure A.2: Example of the high pass filter for a typical shape.

or

$$\frac{dE_{out}}{dt} + \frac{1}{\tau}E_{out} = \frac{1}{\tau}E_{in} \tag{A.11}$$

If RC is sufficiently large, only the first term on the left is significant, and then

$$\frac{dE_{out}}{dt} \simeq \frac{1}{\tau}E_{in} \tag{A.12}$$

or

$$E_{out} = \frac{1}{\tau}\int E_{in}\,dt \tag{A.13}$$

Hence, the name integrator. The network will integrate provided the time constant τ is large compared with the time duration of the input pulse. In the opposite ex-

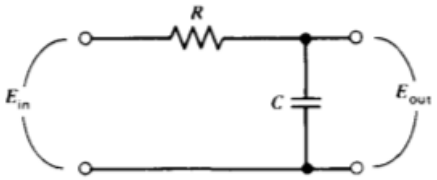

Figure A.3: A low-pass RC filter or integrator network.

treme of small time constant only the second term on the left of (A.11) is significant, and therefore

$$\frac{1}{\tau}E_{out} \simeq \frac{1}{\tau}E_{in} \tag{A.14}$$

or

$$E_{out} \simeq E_{in} \tag{A.15}$$

An example of application of RC low-pass filter for a typical shape from the tested scintillator is given in Figure A.4.

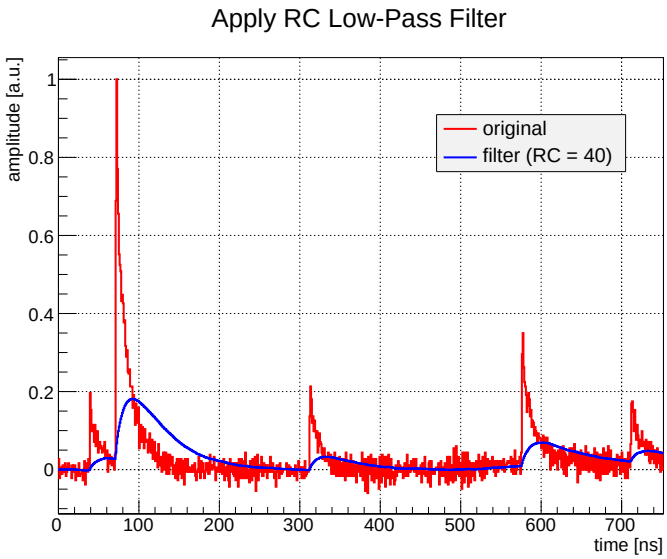

Figure A.4: Example of RC low pass filter on a typical shape.

Bibliography

[1] *Physics letter b*, 2008. http://www.elsevier.com/locate/physletb.

[2] Kenneth S. Krane: *Introductory Nuclear Physics*. John Wiley & Sons, 4th edition edition, 1988.

[3] Glenn F. Knoll: *Radiation Detection and Measurement*. John Wiley & Sons, 2010.

[4] H.R. Bowman, S.T. Thompson, J.C.D. Milton, and J. Swiatecki: *Velocity and angular distributions of prompt neutrons from spontaneous fission of* ^{252}*cf*. Physical Review, 126(6):2120–2136, 1962.

[5] J Iwanowska, L Swiderski, M Moszynski, T Szczesniak, P Sibczynski, N Z Galunov, and N L Karavaeva: *Neutron/gamma discrimination properties of composite scintillation detectors*. Journal of Instrumentation, 6(07):P07007, 2011. http://stacks.iop.org/1748-0221/6/i=07/a=P07007.

[6] S.K. Lee, Y.H. Cho, Kang B.H., *et al.*: *Scintillation properties of composit stilbene crystal for neutron detection*. Progress in nuclear science and technology, 1:292–295, 2011.

[7] Syed Naeem Ahmed: *Physics & Engineering of Radiation Detection*. Elsevier, 2007.

[8] J.B. Birks: *The Theory and Practice of Scintillaton Counting*. Pergamon Press, 1964.

[9] Bernard Valuer: *Molecular Fluorescence: Principles and Applications*. Wiley-VCH, 2001.

[10] H.K. Shin and B.J. Koh: *Comparison of light output from ne213 for electrons and protons*. Journal of the Korean Nuclear Society, 11(2):111–117, 1979.

[11] Bollinger L. and Thomas G.: *Measurement of the time dependence of scintillation intensity by a delayed-coincidence method*. Review of scientific Instruments, 32(9):1044–1050, 1961.

[12] BC501 Data Sheet. http://www.crystals.saint-gobain.com/uploadedFiles/SG-Crystals/Documents/SGC%20BC501_501A_519%20Data%20Sheet.pdf.

[13] EJ301 Data Sheet. http://www.eljentechnology.com/index.php/products/liquid-scintillators/71-ej-301.

[14] P.A. Söderström, J. Nyberg, and R. Wolters: *Digital pulse-shape discrimination of fast neutrons and γ-rays*. Nuclear Instruments and Methods in Physics Research A, 594, 2008.

[15] K.A.A. Gamage, M.J. Joyce, and N.P. Hawkes: *A comparison of four different digital algorithms for pulse-shape discrimination in fast scintillators*. Nuclear Instrument and Methods in Physics Research A, 642, 2011.

[16] M. Nakhostin and P.M. Walker: *Application of digital zero-crossing technique for neutron–gamma discrimination in liquid organic scintillation detectors*. Nuclear Instruments and Methods in Physics Research A, 621, 2010.

[17] S Marrone, D Cano-Ott, N Colonna, C Domingo, F Gramegna, E.M Gonzalez, F Gunsing, M Heil, F Käppeler, P.F Mastinu, P.M Milazzo, T Papaevangelou, P Pavlopoulos, R Plag, R Reifarth, G Tagliente, J.L Tain, and K Wisshak: *Pulse shape analysis of liquid scintillators for neutron studies*. Nuclear Instruments and Methods in Physics Research Section A: Accelerators, Spectrometers, Detectors and Associated Equipment, 490(1–2):299 – 307, 2002, ISSN 0168-9002. http://www.sciencedirect.com/science/article/pii/S016890020201063X.

[18] Natalia Zaitseva, Benjamin L. Rupert, Iwona PaweŁczak, Andrew Glenn, H. Paul Martinez, Leslie Carman, Michelle Faust, Nerine Cherepy, and Stephen Payne: *Plastic scintillators with efficient neutron/gamma pulse shape discrimination*. Nuclear Instruments and Methods in Physics Research Section A: Accelerators, Spectrometers, Detectors and Associated Equipment, 668(0):88 – 93, 2012, ISSN 0168-9002. http://www.sciencedirect.com/science/article/pii/S0168900211021395.

[19] EJ299 33 Data Sheet. http://www.eljentechnology.com/index.php/products/plastic-scintillators/114-ej-299-33.

[20] D. Cester, G. Nebbia, L. Stevanato, F. Pino, and G. Viesti: *Experimental tests of the new plastic scintillator with pulse shape discrimination capabilities ej-299-33*. Nuclear Instruments and Methods in Physics Research A, 735, 2013.

[21] S.A. Pozzi, M.M. Bourne, and S.D. Clarke: *Pulse shape discrimination in the plastic scintillator ej-299-33*. Nuclear Instruments and Methods in Physics Research A, 723:19–23, 2013.

[22] EJ309 Data Sheet. http://www.eljentechnology.com/index.php/products/liquid-scintillators/73-ej-309.

[23] S.D. Ambers, L. Huang, M. Flaska, and S.A. Pozzi: *Reference-pulses nutron/gamma-ray pulse shape discrimination in liquid scintillators for deposited neutron energies from 200 kev*. In *IEEE*.

[24] Hamamatsu Website. http://www.hamamatsu.com.

[25] Peter Križan and Samo Korpar: *Photodetectors in particle physics experiments*. Annual Review of Nuclear and Particle Science, 63(1):329–349, 2013. http://www.annualreviews.org/doi/abs/10.1146/annurev-nucl-102212-170604.

[26] Claudio Piemonte: *A new silicon photomultiplier structure for blue light detection*. Nuclear Instruments and Methods in Physics Research Section A: Accelerators, Spectrometers, Detectors and Associated Equipment, 568(1):224 – 232, 2006, ISSN 0168-9002. http://www.sciencedirect.com/science/article/pii/S016890020601271X, New Developments in Radiation Detectors Proceedings of the 10th European Symposium on Semiconductor Detectors 10th European Symposium on Semiconductor Detectors.

[27] AdvanSiD Website. http://advansid.com.

[28] N Serra, A Ferri, A Gola, T Pro, A Tarolli, N Zorzi, and C Piemonte: *Characterization of new fbk sipm technology for visible light detection*. Journal of Instrumentation, 8(03):P03019, 2013. http://stacks.iop.org/1748-0221/8/i=03/a=P03019.

[29] S. Carturan, A. Quaranta, T. Marchi, F. Gramegna, M. Degerlier, M. Cinausero, V. L. Kravchuk, and M. Poggi: *Novel polysiloxane-based scintillators for neutron detection*. Radiation Protection Dosimetry, 143(2-4):471–476, 2011. http://rpd.oxfordjournals.org/content/143/2-4/471.abstract.

[30] Matteo Dalla Palma: *Produzione e caratterizzazione di materiali siliconici con emissione nel rosso per la rivelazione di radiazioni*. Master's thesis, Università degli studi di Trento, 2012.

[31] CAEN Website. http://www.caen.it/csite/CaenProd.jsp?idmod=570&parent=11.

[32] R. Aryaeinejad, E.L. Reber, and D.F. Spencer: *Development of a handheld device for simultaneous monitoring of fast neutrons and gamma rays*. IEEE Transactions on Nuclear Science, 49(5), 2002.

[33] B. D' Mellow, M.D. Aspinalla, R.O. Mackina, M.J. Joycea, and Peytonb A.J.: *Digital discrimination of neutrons and γ-rays in liquid scintillators using pulse gradient analysis*. Nuclear Instrument and Methods in Physics Research A, 578, 2007.

[34] D.I. Shippen, M.J. Joyce, and M.D. Aspinall: *A wavelet packet transform inspired method of neutron-gamma discrimination*. IEEE Transaction on Nuclear Science, 57(5), 2010.

[35] H.H. Knox and T.G. Miller: *A technique for determining bias settings for organic scintillators*. Nuclear Instruments and Methods in Physics Research A, 101, 1972.

[36] K.F. Flynn, L.E. Glendenin, P. Steinberg, and P.M. Wrigth: *Pulse height-energy relations for electrons and alpha particles in a liquid scintillator.* Nuclear Instruments and Methods, 27:13–17, 1964.

[37] ROOT Website. http://root.cern.ch/drupal/.